2 (m¹ˣ)

NASA CR-139006

TEXAS INSTRUMENTS
INCORPORATED

132

FINAL TECHNICAL LETTER REPORT
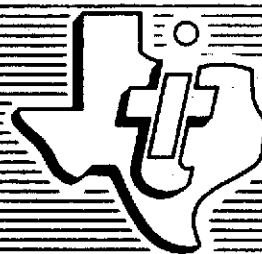FOR
MARINER JUPITER/SATURN 1977
INFRARED INTERFEROMETER
SPECTROMETER (MJS'77) DESIGN STUDY

Prepared for:

National Aeronautics and
  Space Administration
Goddard Space Flight Center
Greenbelt, Maryland

Contract No. NAS 5-23270

Equipment Group
Document No. 859505
April 1974

TEXAS INSTRUMENTS
INCORPORATED

PREFACE

Texas Instruments Incorporated was contracted by NASA/
Goddard Space Flight Center to conduct a design study of the
Infrared Interferometer Spectrometer and Radiometer (IRIS)
instrument chosen for experimentation on the Mariner Jupiter/
Saturn 1977 mission. This effort was the third of three studies
preceding the hardware development program. The first of these
demonstrated the feasibility of adapting the basic subsystem to
the MJS'77 mission requirements. The second of this series
established electronic, mechanical, thermal and environmental
interfaces between the instrument and spacecraft jointly com-
patible with their respective requirements. The primary objec-
tive of the design study was to investigate a number of potential
problem areas identified in previous studies and to develop the
instrument system designs along lines providing for the optimum
performance attainable with the allowable budgets.

This final study report is submitted in compliance with
the requirements of NASA contract NAS 5-23270. Modification No. 2,
to the subject contract, reduced the scope of this report to a
technical letter summary primarily oriented towards readers
already familiar with the basic instrument design. Accordingly, the
usual general instrument descriptions have been omitted. The
information contained herein is primarily based on the results
of the final review held at the Texas Instruments facility in
Dallas, Texas on 18 and 19 March 1974 and subsequent developments.

TABLE OF CONTENTS

LIST OF TABLES

LIST OF FIGURES

LIST OF FIGURES (CONT'D)

7<

I.   INTRODUCTION

A.   Background

During the MJS'77 IRIS Compatibility Study the conceptual design of the instrument was developed in greater detail in order to accurately define the spacecraft interfaces. At the conclusion of this study effort, in September 1973, the only major interface problem which remained unresolved was that of the intensity of the electromagnetic field generated by the Michelson motor portion of the IRIS subsystem.

Prior to the start of the MJS-IRIS Design Study, several major technical problems, or potential problem areas, had been defined which were not directly related to instrument interfaces. These included problems associated with the choice of the primary interferometer detector; the performance of the data channels and phase lock loop; the redesign of the Michelson motor; the instrument mounting scheme; and the beamsplitter mounting and coating.

Two detector types appeared to be capable of meeting the performance levels required of the interferometer detector, the pyroelectric and the thermopile. Fairly recent developments in the pyroelectric detectors had been made through the use of improved active flake materials. Theoretical predictions supported by reasonable extrapolations of available test data, gave every indication that a device could be produced which would be suitable for the instrument application. However, none of the units actually built exhibited the superior NEP characteristics required of the IRIS interferometer detector.

The problems associated with the thermopile detector were of a slightly different nature. The NEP's of available detectors were in themselves adequate. The main difficulty was in their extremely low signal and noise levels. The input noise levels typical of conventional preamplifiers far exceeds that of the thermopile detectors. Thus, in order to maintain a detector noise limited system, a preamplifier would have to be designed which would be jointly compatible with the detector noise levels and instrument physical budgets.

The increased instrument sensitivity also imposes stringent requirements on the performance of the data channel and phase lock loop. The noise and error contributions of these circuits must remain compatible with those of the detector even as the instrument is subjected to spacecraft vibrations. While it was recognized at the outset that modifications to the basic MM'71 design would have to be made to improve and optimize, the magnitude and scope of the changes was unknown. Furthermore, the longer interferogram time and lower signal frequencies associated with the MJS design, were seen as compounding obstacles.

The Michelson motor would have to be redesigned to reduce the external magnetic field by approximately an order of magnitude in order to comply with the spacecraft EMI requirements. This redesign would have to be constrained to be at least compatible with, if not complementary to, the basic phase lock loop design.

The mounting scheme adopted on previous instruments used rubber insulators primarily for thermal flux and stress isolation, and to some extent, vibration isolation as well. This technique could not be expected to maintain the required boresight stability over the extended temperature ranges of the MJS'77 mission. A new scheme would have to be devised which satisfied the boresight, thermal design, vibration, and budget requirements.

The results of tests performed in the development of the MM'71 beamsplitter indicate that the mounting technique will have to be substantially improved for the MJS'77 application. Thermal stresses exerted on the Cesium Iodide beamsplitter by the optical housing and beamsplitter assembly must be reduced to allow the beamsplitter to survive temperature transitions down to the 200°K operating temperature.

B. Design Study

The design study goals initially established were predominantly addressed to the technical problem areas previously discussed. Preliminary design tasks were also planned in the mechanical and thermal design areas in order to support the detailed development of the instrument optical design. And finally, effort was planned to investigate onboard calibration schemes and non-linearities imputed to the instrument ADC.

Three major study areas materialized during the study due to unplanned developments. These were the FDS interfaces, the telescope, and radiation.

The interfaces between the IRIS and FDS continued to be in a state of flux during the early stages of the study as the relationships between the FDS and other subsystems began to take form. The impact of these changes was most significant to the radiometer channel definition and design.

The second major area of study which developed dealt with the design and fabrication of the telescope. The original telescope concept consisted of using extremely light weight replicated mirror surfaces mounted to honeycomb aluminum substrates. Early studies of the replication process revealed serious problems in the producibility of the large primary mirror and in maintaining mechanical integrity over the operating temperature range. As confidence in the replication process and manufacturer flagged, numerous alternate approaches were pursued in depth.

The final study effort not previously planned was in support of passive electron radiation tests conducted by JPL in March of this year. Additional effort has been applied, and is continuing, in support of the next phase of radiation evaluation testing.

C.   Study Results Summary

The MJS'77 IRIS Design Study has served as a cost-effective prelude to the hardware development program. Viable solutions have been identified for the major technical problem areas. The design study has also resulted in the detailed definition of instrument systems and designs and has produced valuable design and analysis tools which will provide for a totally integrated and optimum instrument design.

With respect to the major problem areas, a redesign of the Michelson motor has been derived which will make it compatible with the spacecraft EMI requirements, the instrument budgets, and the phase lock loop design. Detector tests and studies have identified practical means of improving the NEP of pyroelectric detectors to a value consistent with the instrument objectives and have demonstrated the thermopile detector to be a viable alternate to the pyroelectric. An instrument mounting design has been detailed which jointly accommodates the boresight and instrument design requirements as well as the physical budgets. And finally, new beamsplitter mounting and coating techniques have been devised to provide for its optical stability over the temperature extremes.

Detailed computerized models of the data channel, Michelson motor, and mechanical designs have been constructed which will guide and verify the detail instrument design. Figure 1 depicts the major inputs and outputs of these models and illustrates the manner in which they are interlocked to provide an analytical base for the integration of the various design disciplines. Tying these models together permits various areas of the design to be analyzed in terms of their effect upon the instrument end product as a function of NER. These basic design tools are expected to be used throughout the instrument detailed design and verification and possibly in hardware problem troubleshooting and analysis in the latter phases of the hardware program.

While some questions remain in the radiometer area, the optical design has been described in detail. An optical tolerance analysis has been conducted which will allow for the iteration of the optomechanical and thermal designs. The telescope problems and alternatives have been explored in depth leading to the current design and fabrication recommendations. Finally, radiation tests have identified a number of potential problem areas which could have pronounced effects upon instrument designs. Efforts in this area are continuing in support of more extensive

FIGURE 1.   MJS-IRIS DESIGN STUDY

COMPUTER MODELS

PLL/DATA CHANNEL
ERROR SOURCES →

DATA CHANNEL MODEL → NER

1. DESIGN REQUIREMENTS
   a. DATA CHANNEL
   b. PLL
   c. MICHELSON MOTOR
   d. MOUNTING

2. OPTIMIZATION

3. TROUBLESHOOTING AND
   ANALYSIS

MICHELSON MIRROR DISPLACEMENT ↑

MAGNETIC DESIGN →

DAMPING CHARACTERISTICS →

MICHELSON MOTOR MODEL → POWER REQUIREMENTS

HOUSING DISPLACEMENT ↑

PLATFORM VIBRATION →

LAUNCH AND FLYBY LOADS →

INSTRUMENT MECHANICAL MODEL → STRESS LOADS

→ STRESS DEFLECTIONS

4

testing to be conducted to more fully assess the impact of the
radiation hazards.

Along with the many accomplishments of the study
effort, were some disappointments. The most significant of these
were in the optical design and data modeling areas. Slow progress
in optical design definition took its toll in the development
of the housing design and analyses. Problems encountered in the
final stages of the data channel modeling prevented it from be-
ing used to specify performance requirements for a number of
electronic circuit elements.

A summary of study results is contained within the
following sections of this report. Table 1 lists the general
instrument specifications. Section II describes the optical design
layout and the results of the optical tolerance analyses. Section
III covers the mechanical design areas including the beamsplitter
and telescope. The results of the electronics design and detector
studies are contained in Section IV, along with a description of
the current FDS interface definitions. Appendix A describes the
various elements of the data channel model in some detail. This
report is concluded with Appendix B which summarizes the results
of the passive radiation tests conducted in early March of this
year.

TABLE 1. MJS SYSTEMS SPECIFICATIONS

Spectral range	
Interferometer	200 to 4000 cm^{-1} (2.5 to 50.0 μm)
Radiometer	5000 to 33,000 cm^{-1} (0.3 to 2.0 μm)
Spectral resolution	
Maximum	4.42 cm^{-1}
Sym interferogram	11.12 cm^{-1}
Resolved spectral intervals (maximum)	860
Instrument aperture	
IRIS	7.26 cm^2 (3.05 cm)
Telescope	2,027 cm^2 (50.8 cm)
Instrument FOV	
IRIS	4.17 degrees (72.8 mrad, 4.16 X 10^{-3} sr)
Telescope	0.25 degrees (4.37 mrad, 1.49 X 10^{-5} sr)
Operating temperature	<200° K maximum
NER–IRIS	<7 X 10^{-10} Wcm^{-2} sr^{-1} cm
NEP–detector in radiometry channel	<1 X 10^{-9} WHz$^{-\frac{1}{2}}$
NEP–IRIS detector	<1 X 10^{-10} WHz$^{-\frac{1}{2}}$
System weight	16.1 kg
Primary power	15.3 W (peak)
Standby power	3.2 W (average)
Interferometer frame time	48 seconds
Interferogram time	45 seconds
Reference wavelength	0.58525 μm
Reference frequency	120 Hz
Mirror velocity	3.51 X 10^{-3} cm s^{-1}
Mirror travel	0.158 cm
Optical path difference	0.316 cm
Data frequency	1.4 to 28 Hz
Data word rate	80 Hz
A/D word length	13 bits
Output word length	14 bits
Bit rate	1.120 BPS
Samples per interferogram	3,600 (4096)*
Zero crossings per data Word	
To summation	1
To output	3
Dynamic range including chirping	16,000

*Zeros will be added before processing the interferogram to obtain 4,096 words.

II. OPTICAL DESIGN

The overall system optics layout is shown in Figure 2, terminating at the interferometer fixed mirror. The distances and curvatures shown are fixed for the telescope, while some variations might arise behind the telescope image plane as the design is analyzed further. The dichroic reflector used to collimate the beam into the interferometer is currently being considered a spherical section, but will be analyzed further before this is confirmed. The dichroic has a double function in the optical system, since it images the primary mirror onto the interferometer fixed mirror. Because of the physical depth of the telescope primary, the actual focal plane is not that well defined, so that the distance between the dichroic and fixed mirror may not be precisely 9.873 inches. The collector shown for the radiometer is on-axis, which differs from the off-axis configuration originally conceived. Closer study has indicated that the on-axis configuration can be arranged to match the radiometer FOV to that of the interferometer, a situation impossible to achieve with the off-axis radiometer collector. The matched FOV plus the mechanical simplicity of an on-axis collector has warranted the change. An extensive study is currently underway to verify that the FOV of the two systems can indeed be matched in this way.

Figure 3 shows the interferometer housing layout, as conceived at the time of the design review on March 18-19. This figure shows the reference channel coaxially located as was the case in previous IRIS systems. Recent reviews of the expected electron flux environment around Jupiter have indicated that fluorescence from the CsI beamsplitter might cause interference in the reference channel, causing the PLL to lose lock during the planetary encounter. To avoid this a design change is currently under consideration to place the reference interferometer behind the Michelson motor, and completely shielded from the beamsplitter. This change will involve mounting a reference channel Michelson mirror on the back of the motor shaft and constructing a miniature interferometer behind the motor to generate the reference signal. This allows closer coupling of the interferometer redesign. The only drawback to this system change is that the IR interferometer can no longer be aligned by simply aligning the reference channel.

The optical design was extended beyond the basic layout in several areas, but these are not completely resolved at this time. Figures 4-6 show the relationship between misalignment and spherical distortion of elements of the interferometer and the signal intensity at the detector. It can be seen that distortions in the optics become more critical at higher frequencies, and are especially critical in the beamsplitter because of the double pass through the optics.
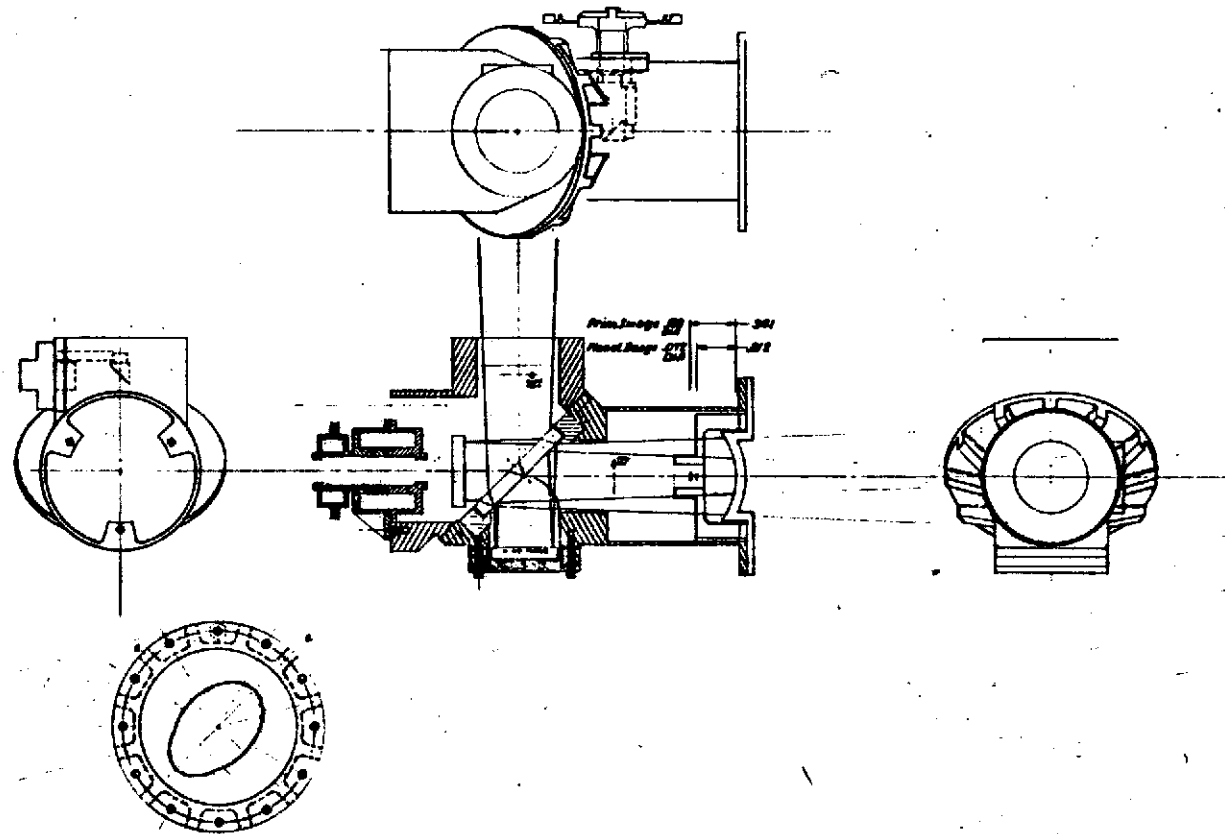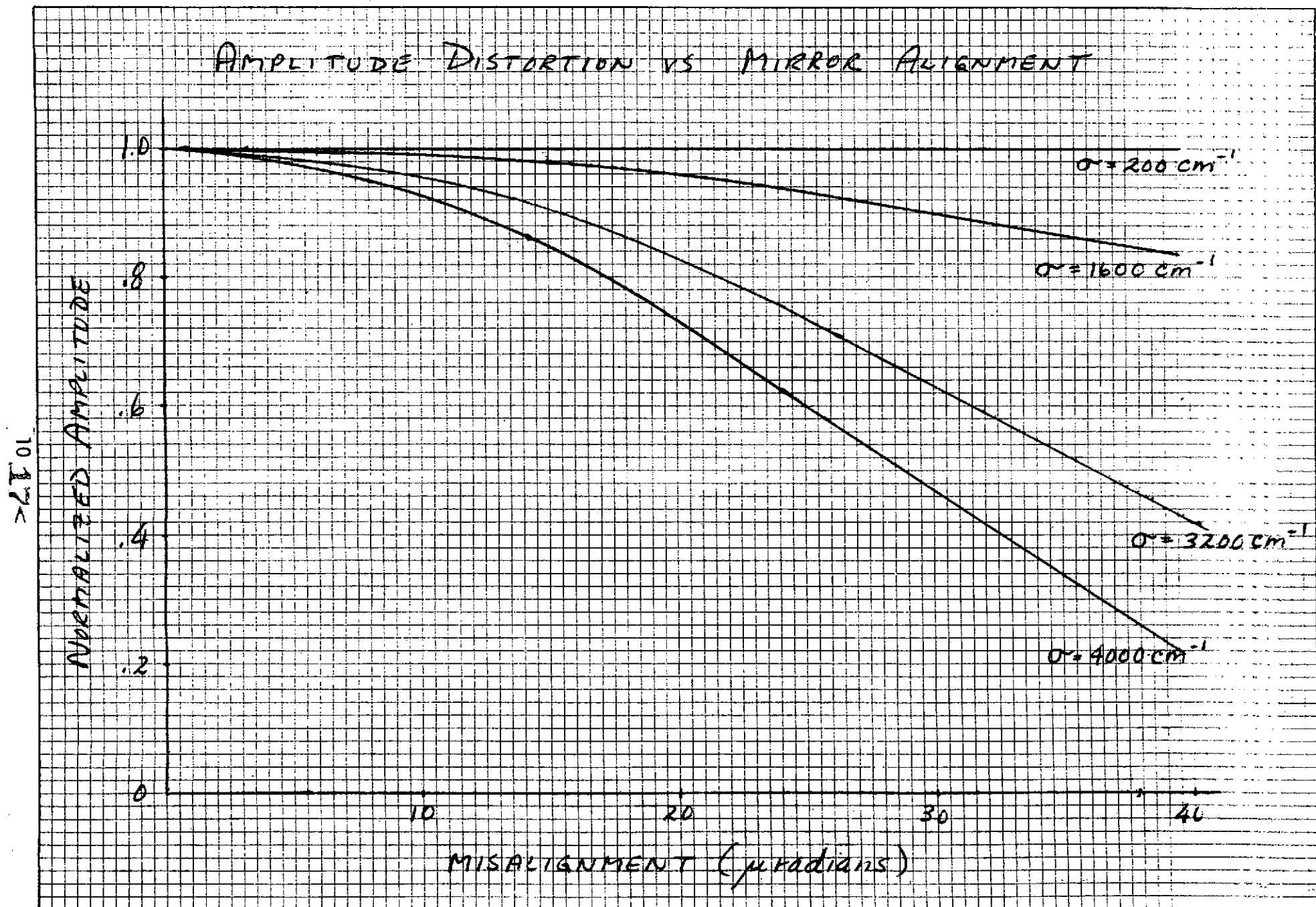
FIGURE 2. MJS IRIS OPTICAL LAYOUT

FIGURE 3.

FIGURE 4.
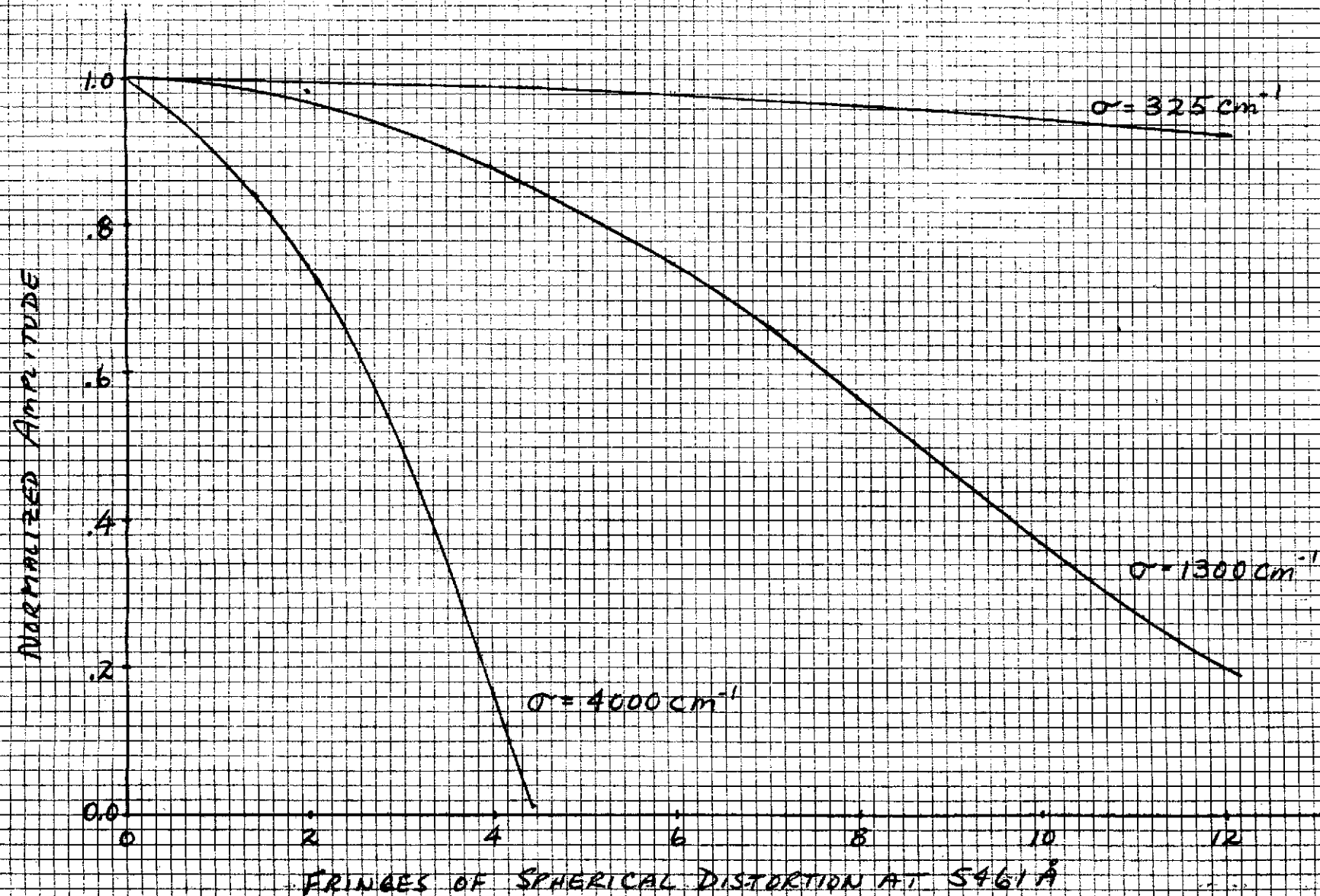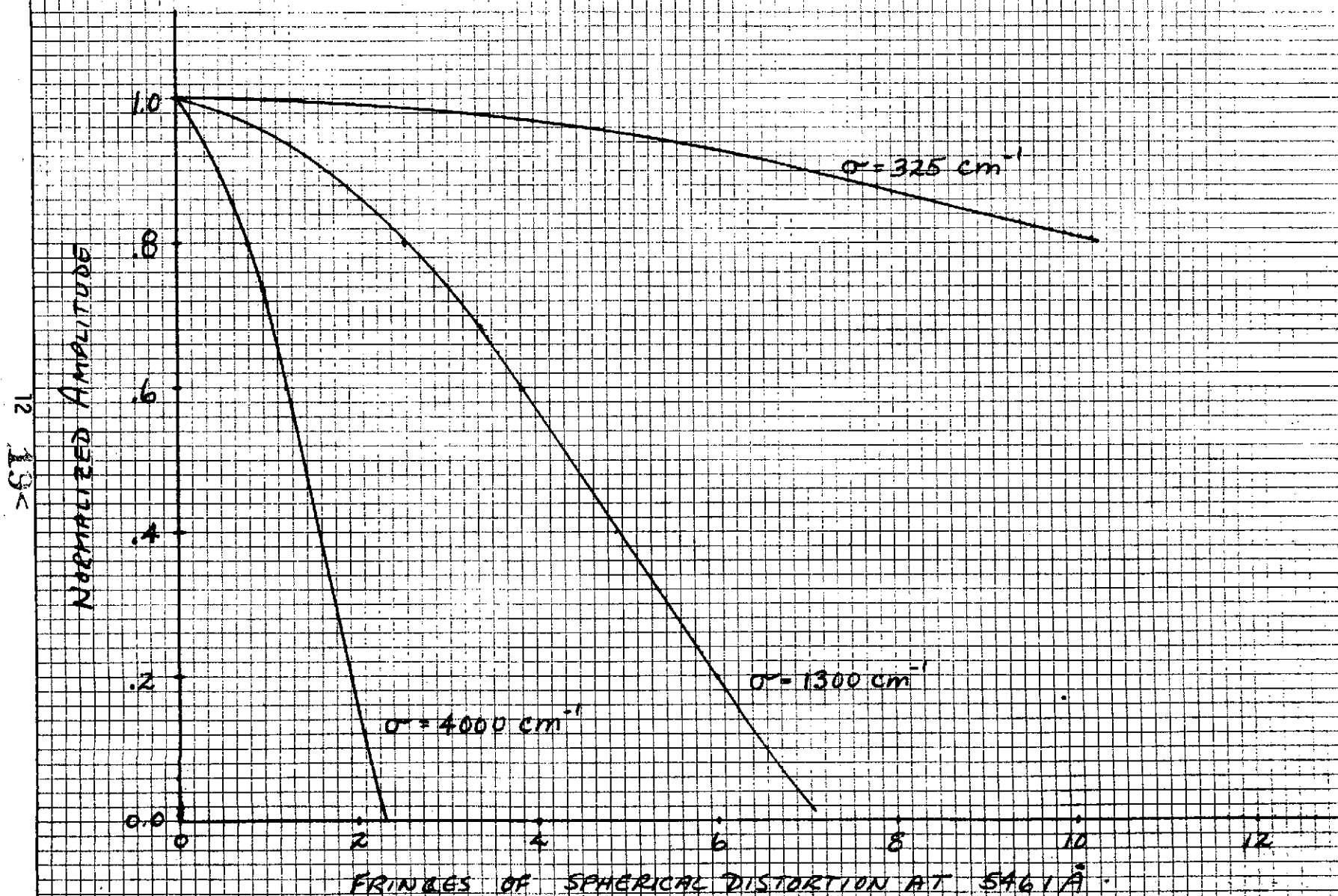
FIGURE 5.

FIGURE 6.

A partial tolerance analysis was carried out with regard to movement of various optical elements. The coordinate system used in this analysis is shown in Figure 7. The optical system has been considered in two parts; the telescope which determines boresight and FOV, and the interferometer/radiometer systems that analyze the energy collected by the telescope. Distortions caused by the telescope have been related to movements of the telescope secondary along the y or z axis producing a boresight deviation accord-to the relationship:

Boresight Deviation (mr) = (5.56×10^{-2}) Displacement (mils)

This transfers ± 9 mils of linear displacement into ± 0.5 mr. A rotation about the y or x axis produces boresight deviations as follows:

Boresight Deviation (mr) = (.278) mirror rotation (mr)

This transfers ± 1.8 mr of mirror rotation into ± 0.5 mr deviation of the boresight.

Translation of the secondary mirror along the x-axis does not affect the boresight, but it does blur the FOV at the tele-scope image plane. Figure 8 shows the blur vs secondary displace-ment, where blur is expressed as a fraction of the FOV.

System tolerance to movements behind the telescope are related primarily to energy losses induced by misalignment. It is planned to use a somewhat oversized detector on the radiometer, so that slight misalignments will not have much effect on this channel. The interferometer, however, will be subject to the usual tolerances for such an instrument, plus a critical align-ment between the dichroic and interferometer. The energy through-put of the system as a function of linear and rotational motion of the dichroic is shown in Figures 9 and 10.

The system optical design is currently undergoing final checks, and an extensive study of the allowable manufacturing and alignment tolerances will be carried out early in the hardware program. A list of the optical design tasks that will be carried out, and their approximate chronological order is shown below:

1. Confirm on-axis radiometer configuration.

2. Extensive tolerance study effort.

3. Define baffling for system.

4. Define calibration hardware.

5. Design reference interferometer.

6. Wavefront analysis to IRIS detector.

7. Design test fixtures.

This list is not all inclusive, and will be extended and modified as necessary during the early stages of the hardware program.
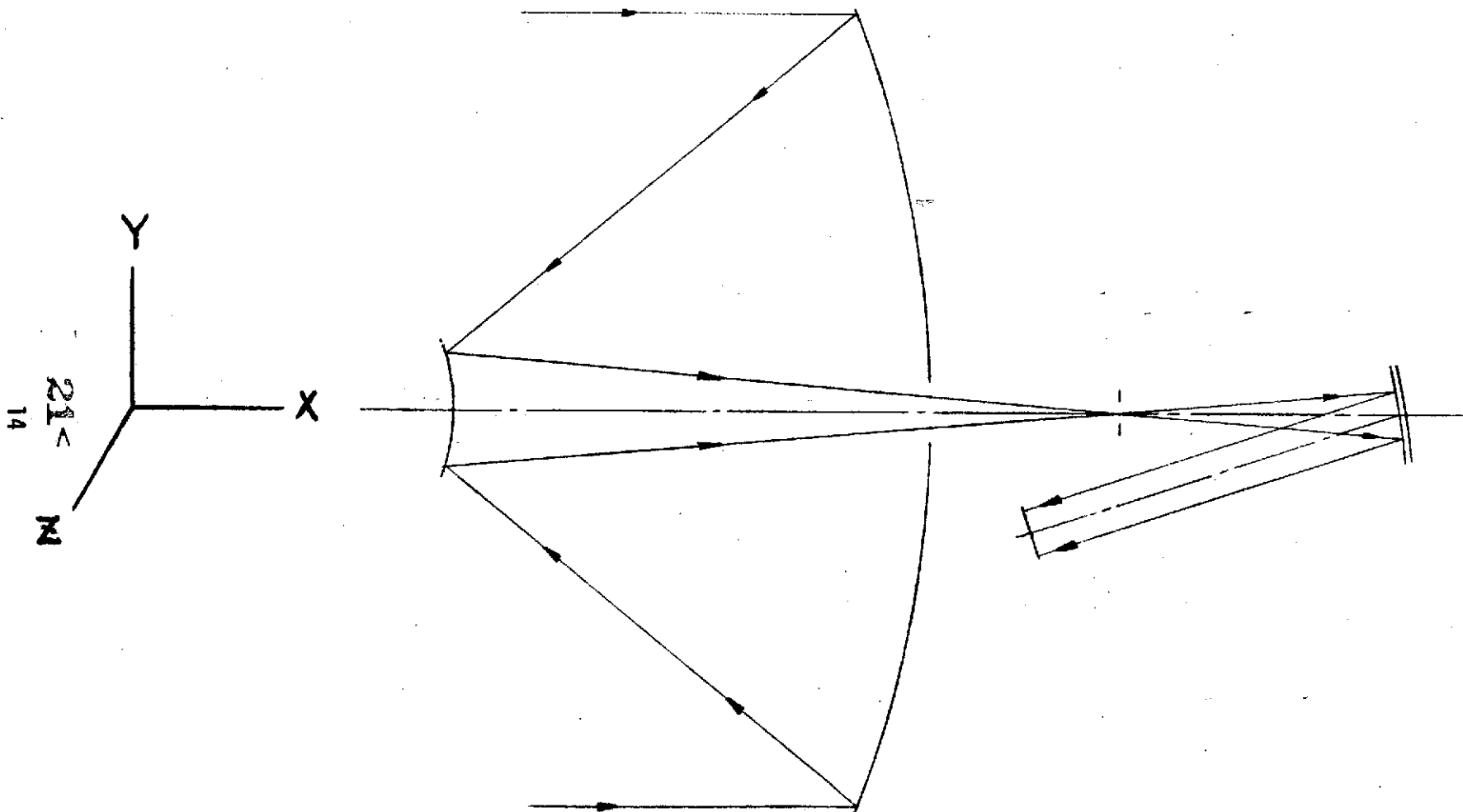
FIGURE 7.
OPTICAL TOLERANCE ANALYSIS COORDINATE SYSTEM

BLUR VS SECONDARY DISPLACEMENT

BLUR

DISPLACEMENT OF SECONDARY (X-AXIS)

22< FIGURE 8.

15

THROUGHPUT VS DICHROIC DISPLACEMENT

POWER
THROUGH-
PUT

1.00

.90

.80
0.00   .01   .02   .03   .04   .05 in

DISPLACEMENT OF DICHROIC (X-AXIS)
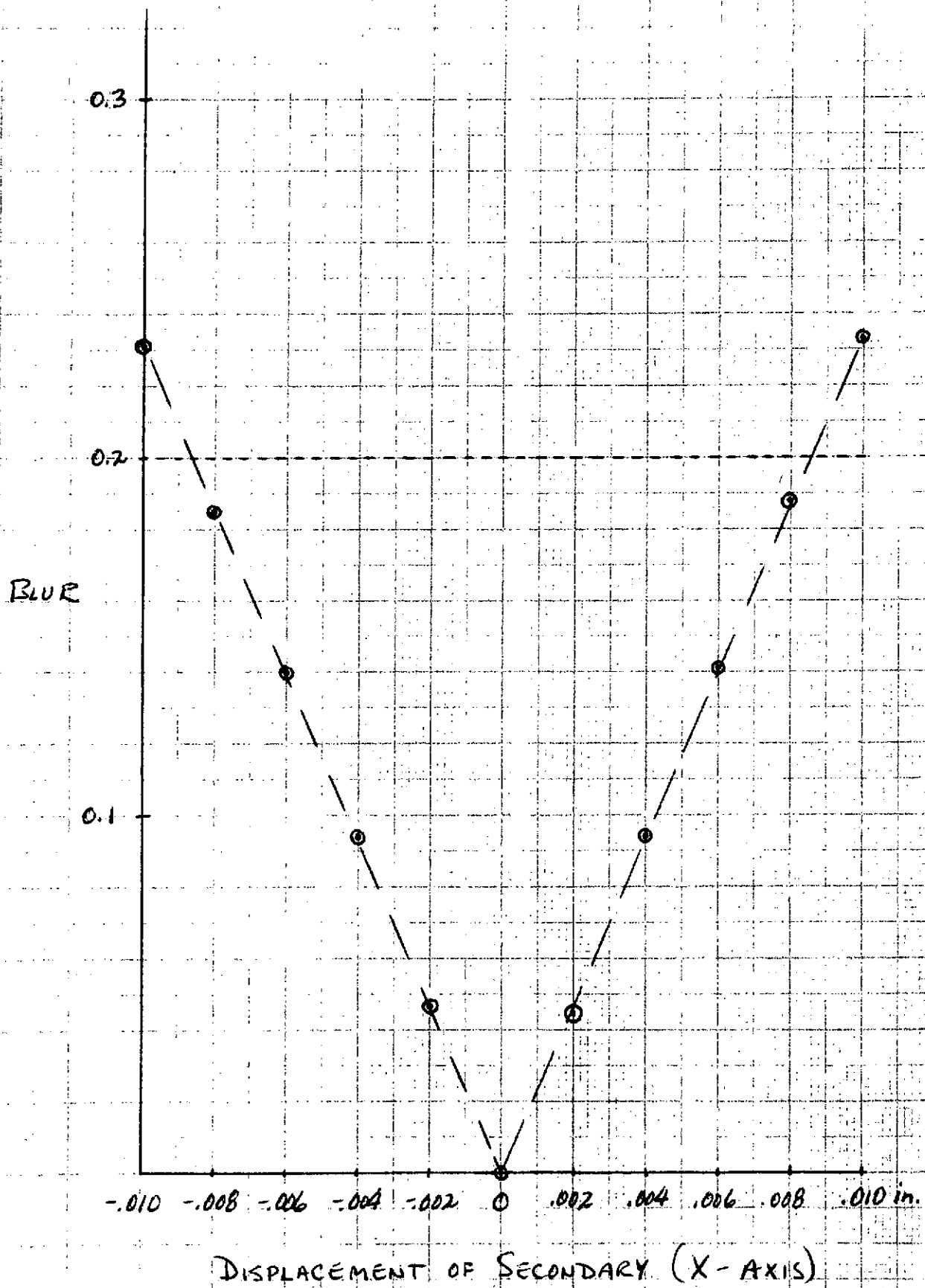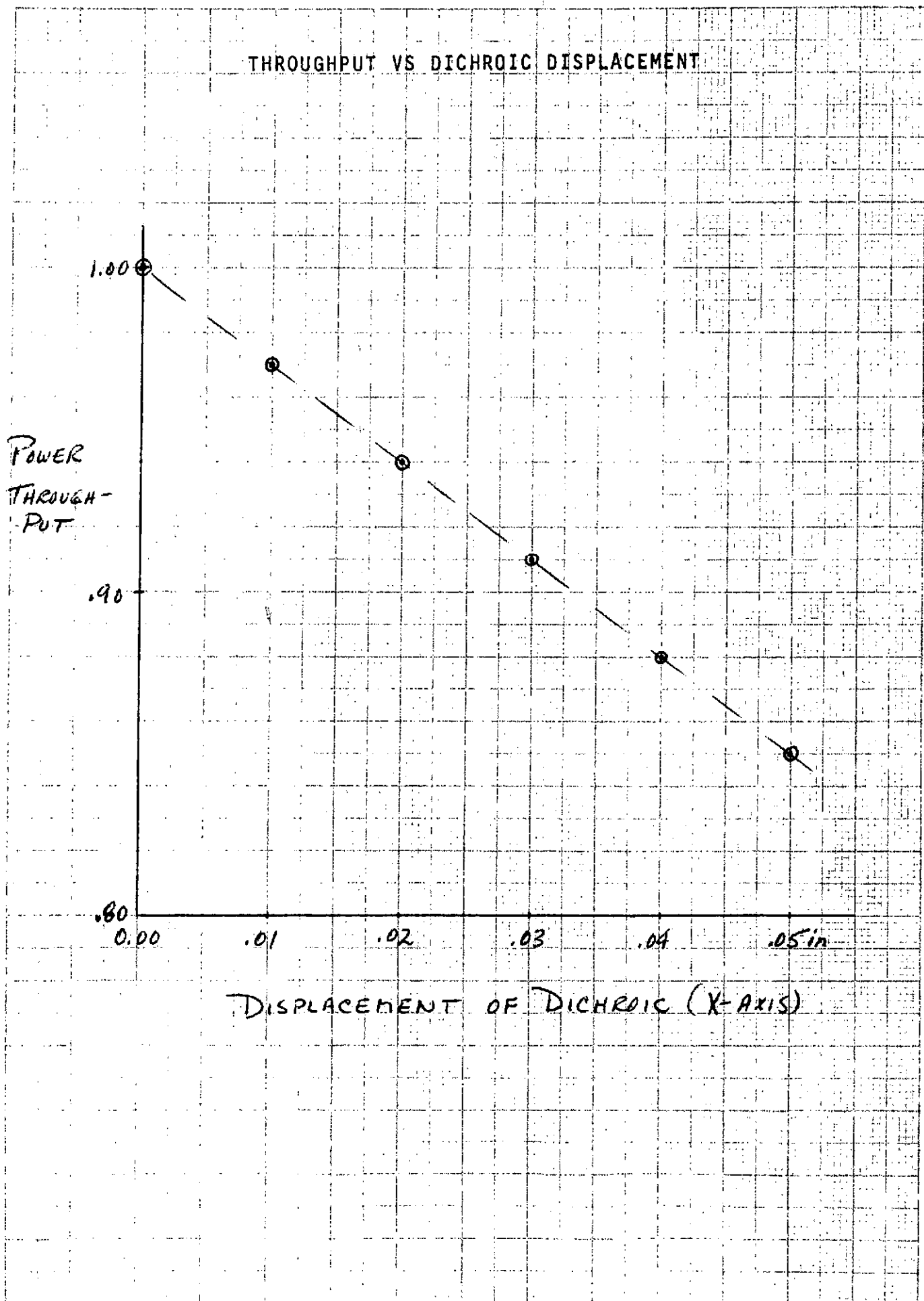
23 FIGURE 9.   16

THROUGHPUT VS DICHROIC ROTATION

POWER

THROUGHPUT

ROTATION OF DICHROIC (Z-AXIS)

24< FIGURE 10.
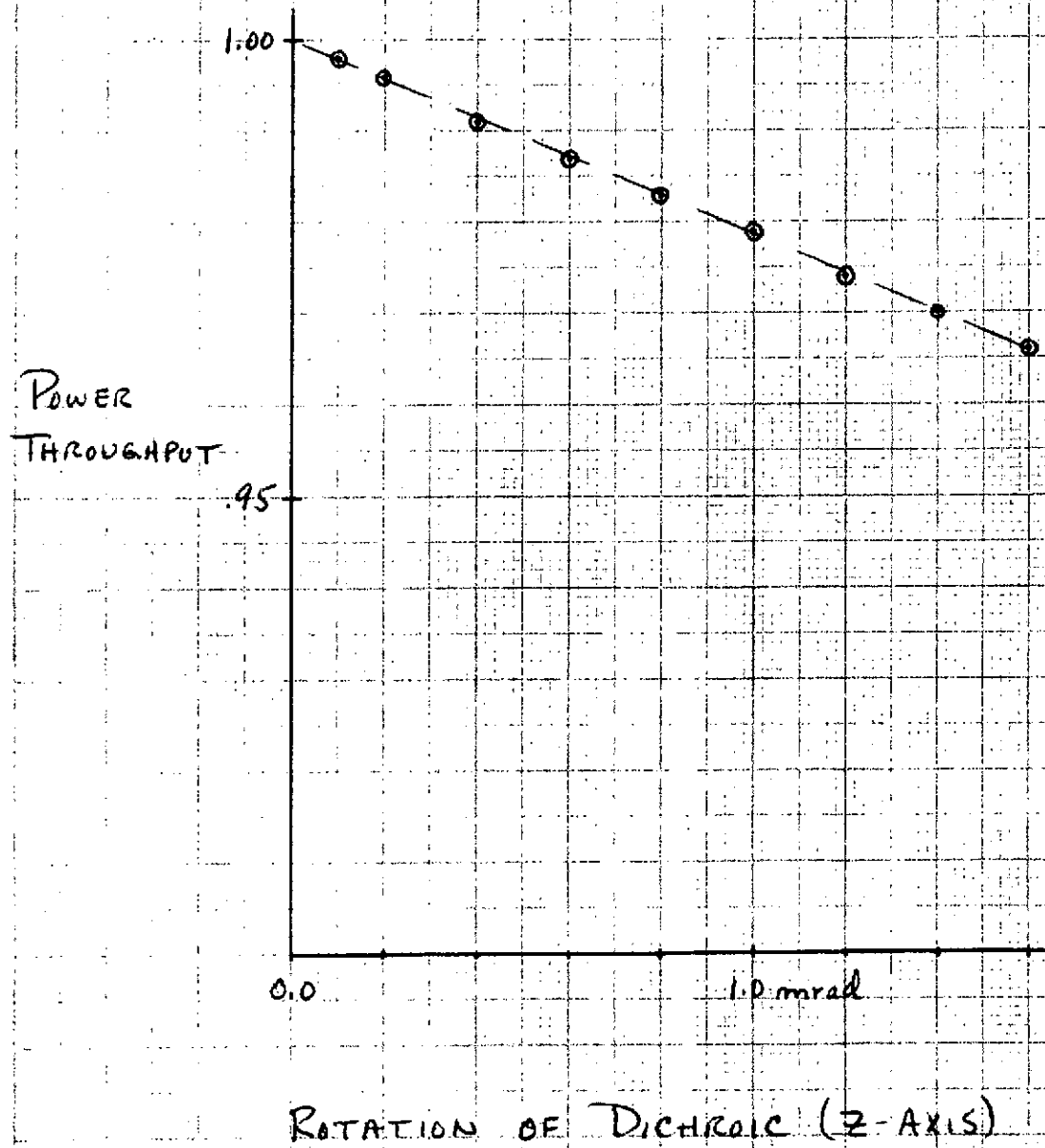
III. MECHANICAL DESIGN

A.   Introduction

Figure 11 depicts the present MJS IRIS & R configuration.
Figure 12 gives details of a preliminary interferometer layout.

With the exception of the tubular member which inter-
faces between the IRIS and the spacecraft scan platform, housings
and structural members are fabricated of beryllium. Regarding
the tubular mounting member, several candidate materials are
being considered. The following discussions outline the rationale
governing materials choices:

B.   Instrument Mounting and Boresighting

Previous IRIS instruments have been three-point
mounted through intervening elastomeric shockmounts. The more
severe MJS'77 mission requirements preclude using this same mount-
ing scheme. Criteria used in selecting the tubular hard-mounted
interface approach are:

IRIS line of sight must be aligned with respect to
two other experiments, with a total or composite boresight error
not to exceed 0.9 milliradians. Therefore,sway and deflections
during fly-by or scan platform articulations must be held to a
minimum, and must be highly predictable.

Mission duration of four years, at an operating temper-
ature of 200^{0}K, with exposure to severe radiation levels, confines
material choices to those for which long-term exposure to space
environment is well documented.

The chosen mounting method must not induce thermal
bending stresses in the IRIS instrument.

Thermal flux through the IRIS/scan platform interface
must be controlled, to within the approximate range of 0.4 to
0.5 watts maximum.

Various hardmounted configurations were examined and
discarded as unsuitable due to either thermal stresses or bore-
sight uncertainty. The tubular mounting approach was finally
selected for weight effectiveness, and for its very predictable
response characteristics.

The interfacing tubular member will be permanently
attached to a projecting boss located on the IRIS central structure,
probably using a combination of tapered pins and a structural
adhesive. The boss on the instrument will be located such that
the tube axis will pass through the center of gravity of the IRIS
& R assembly.

25<
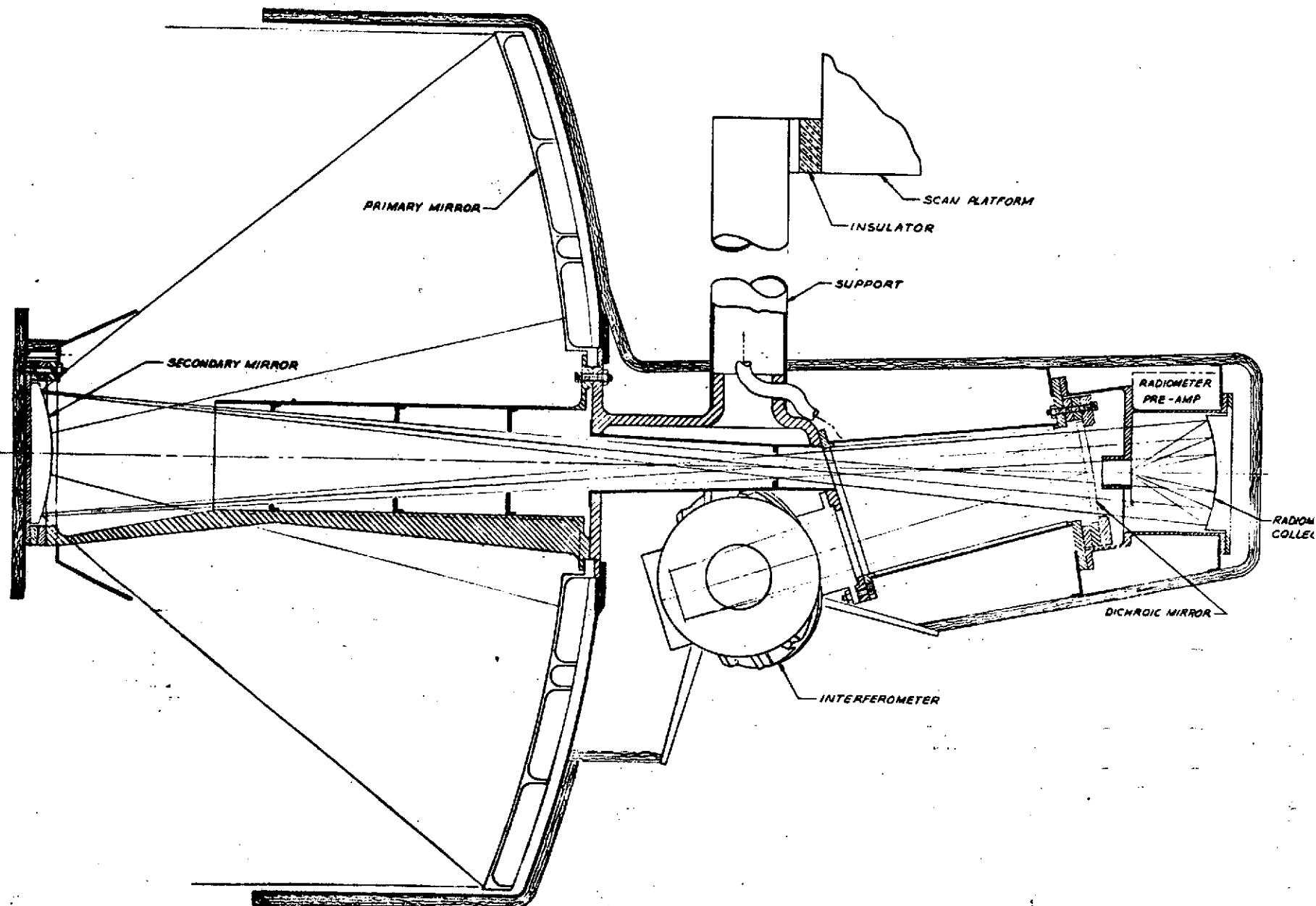
FIGURE 11. MJS IRIS & R CONFIGURATION
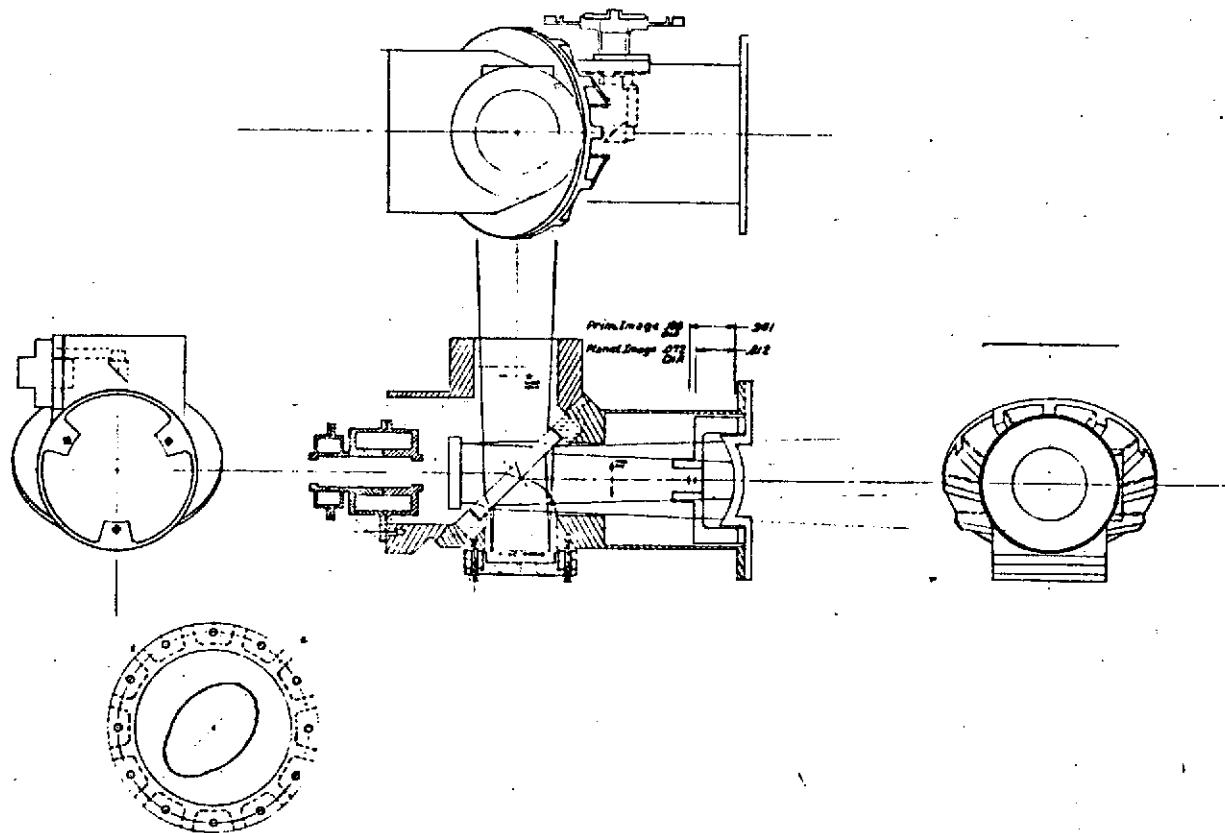
FIGURE **12.**

The spacecraft end of the mounting tube will fit into a flanged socket assembly as shown in Figure 13.

The scan platform side of the mounting flange will be oriented such that it is most nearly perpendicular to the IRIS line of sight, and then permanently affixed to the mounting tube.

Final boresighting is accomplished through a ceramic shim located between the scan platform and mounting flange. This shim will be ground to produce any wedge angles required for exact pointing. A ceramic material is chosen for this shim because of its inherent dimensional stability, and because it provides some further thermal impedance.

The material to be used for the mounting tube itself has not been finally selected at this time. Table 2 lists candidate materials, together with appropriate comments influencing the final choice.

As shown in Figure 11, the tubular mounting system lends itself to use as a conduit for cable routing, should this prove desirable.

C.   Materials Selection

Beryllium is used throughout the IRIS instrument, for housings and structural subassemblies. Stiffness-to-weight and dimensional stability considerations, and good thermal conductivity are the primary reasons for this choice.

Beryllium has a crystalline grain structure, and therefore is anisotropic to an extent which makes wrought beryllium unacceptable for precision optical systems. This anisotropy is offset through the use of beryllium prepared by powder metal techniques; however, a tradeoff is encountered in that yield strengths diminish proportionally as truly isotropic behavior is approached. Initial IRIS design is being performed assuming the use of one of the so-called "optical grades" of beryllium. These materials have moderate anisotropy and yield strength, and are fairly readily available. Additionally, considerable testing has been done for these materials, providing reasonably complete sets of engineering property values for detailed design studies.

Initial stress, thermal and thermal deflection analyses will be performed with optical grade beryllium properties as the baseline. Should findings from these studies prove this choice to be inadequate, matallurgists from both kewecki-Berylco and Brush-Wellman are available to act as consultants in selecting a more suitable grade of beryllium.

CERAMIC SHIM

SCAN PLATFORM
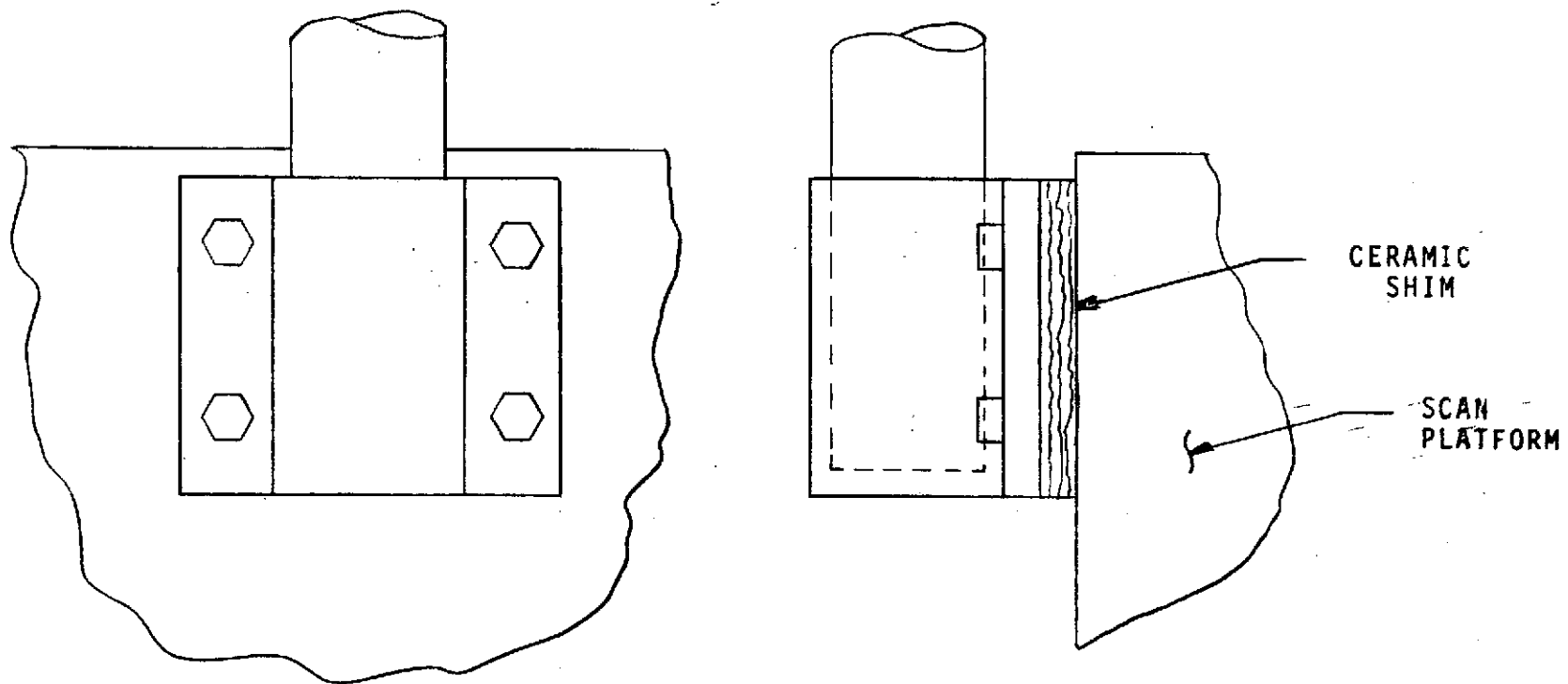
FIGURE 13. SUPPORT TUBE MOUNTING ASSEMBLY

TABLE 2.

IRIS MOUNTING TUBE MATERIALS

MATERIAL	COMMENTS
Stainless Steel	Additional thermal impedance is required to obtain an adequate relationship between thermal conduction and bending stiffness.
Fiberglass	Tends to be heavy. Radiation effects must be evaluated.
Boron/Epoxy Composite	The most promising candidate. Presently working with vendors to obtain optimum performance/weight behavior. Radiation effects on epoxy must be evaluated.

D.   IRIS & R Structures and Housings

1.   Central Structure

As seen in Figure 11 the MJS'77 IRIS & R is assembled about a single continuous central structure, which provides for surfaces referencing the telescope, interferometer, radiometer, and spacecraft interface. This approach is chosen as being the most weight - effective means of providing a reliable, repeatible "set" of reference surfaces. Figure 14 pictorially depicts this machined central structure.

2.   Interferometer

The interferometer is kinematically bolted to the central structure. Since the interferometer housing and its corresponding interface surface are made of the same material, no thermal stress problems are anticipated. As shown in Figure 12, the two interferometer housings are configurationally very similar to those of the M'71 instrument, the primary differences being a size reduction and change from aluminum to beryllium.

3.   Supporting Structure, Dichroic & Radiometer

Incoming energy from the telescope is directed onto a dichroic mirror, which transmits visible light to the radiometer and reflects the infrared energy into the interferometer. The dichroic element and radiometer are supported and positioned by an intermediate skeleton structure as shown in Figure 15. This skeleton support will consist of four slender structural members, brazed at each end to interfacing or reference plates. Following the initial assembly by brazing, both reference surfaces will be ground to achieve the proper dimensional and angular relationships. Four thin sheet beryllium panels will serve to enclose the skeleton structure. This general approach was chosen because it represents a significant weight saving relative to a comparable fully-machined housing.

4.   Radiometer Housing

The radiometer will be packaged in a manner such that it can be repeatably removed and reinstalled, with no effect on the alignment of the rest of the system. The exact housing configuration is expected to be selected following com- pletion of the optical obscuration analysis.

5.   Mirror Mounting

Figure 16 shows a typical MJS mirror mounting configuration. The mirror element is bonded onto a beryllium mounting ring, which in turn is clamped in place over appropri- ately-sized beryllium shim rings, using three screws. The shim rings will be ground and polished such that a slight wedge angle is present. The clamping screws pass through slotted holes in the wedge rings, permitting angular alignment to be accomplished

31<
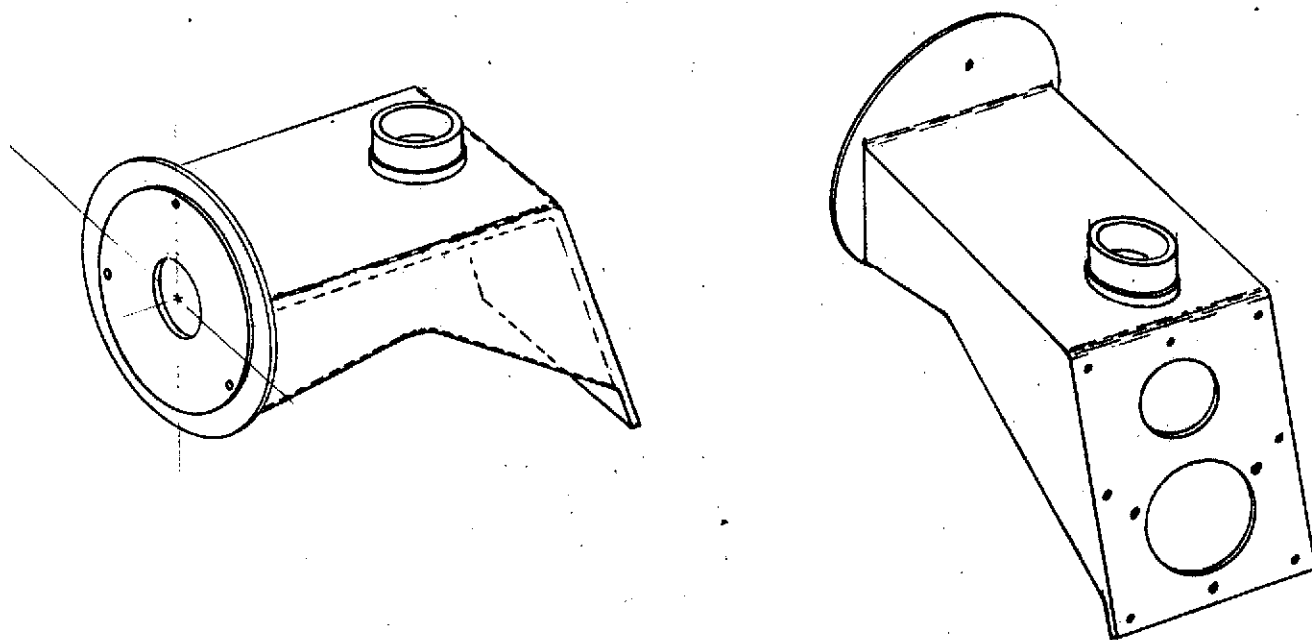
FIGURE 14. CENTRAL STRUCTURE

32<
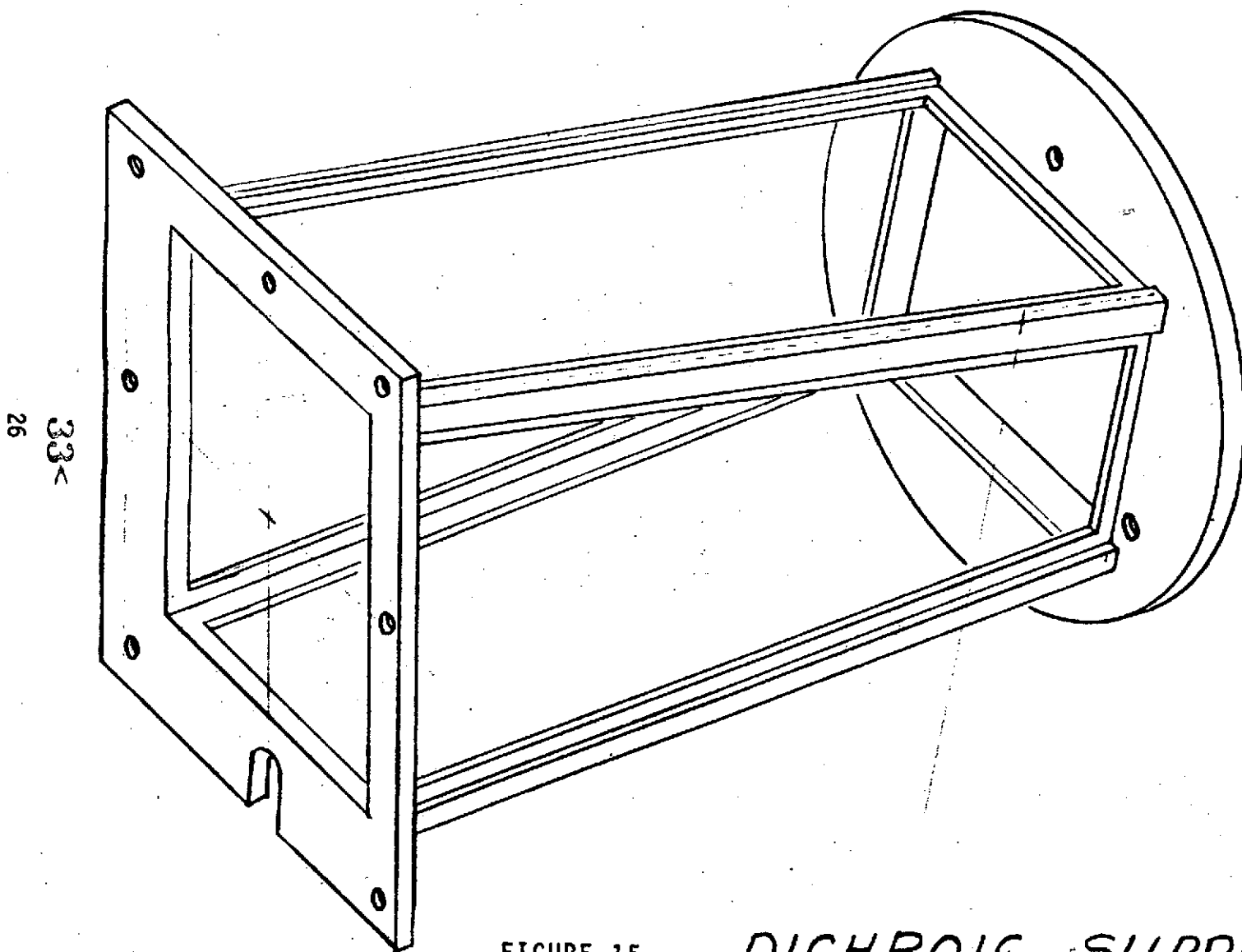
FIGURE 15. DICHROIC SUPPORT

SECONDARY MIRROR
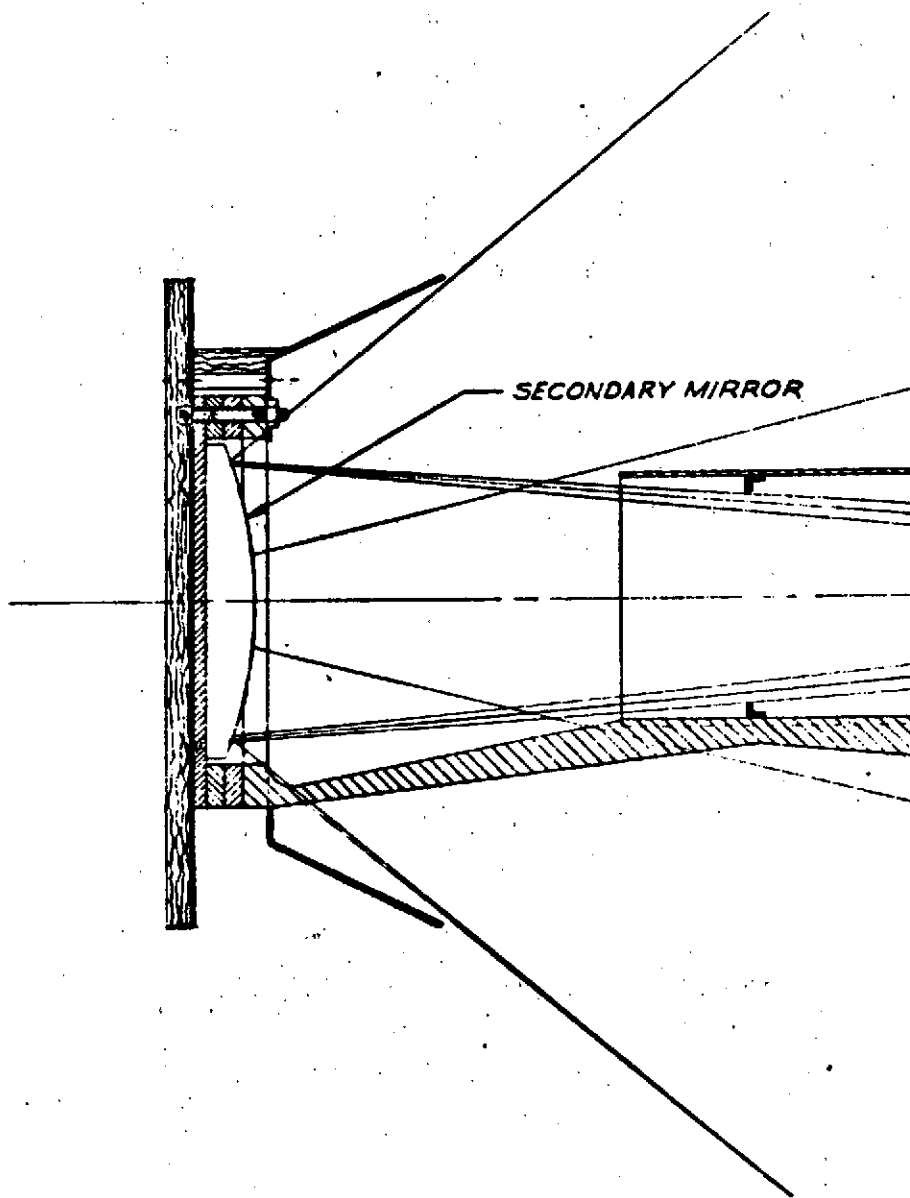
FIGURE 16. MIRROR MOUNT

by rotation of one wedge ring with respect to the other. While alignment by this method is somewhat tedious to accomplish, the certainty of alignment retention following thermal cycling is extremely good. Additionally, this mounting approach is weight-effective, and provides a predictable thermal interface. This general mounting and adjusting means is chosen for the fixed mirror, interferometer and radiometer collectors, dichroic element, and telescope secondary mirror.

      E.   Beamsplitter Study

          1.   Coating

The beamsplitters used on past IRIS systems employed a series of "equivalent layers" of varying refractive indices to match the beamsplitter substrates to the actual beam-splitter surface coating, usually Ge. Each equivalent layer is itself composed of three or more layers of material. The transmission/reflectance curves of beamsplitters prepared this way tend to exhibit large excursions in T and R toward longer wavelengths. This can be minimized by increasing the number of equivalent layers utilized. However, increasing the number of layers decreases the thickness of each layer, and a serious problem in deposition control arises.

Another approach can be taken to obtain the desired gradient in the refractive index of the material between the substrate and beamsplitter surface. Since the stepped equivalent layers are actually an approximation to a smooth gradient, the deposition of a layer of uniformly varying refractive index suggests itself. The large excursions in T and R are reduced considerably, and the problems inherent to coatings with discrete layers are somewhat minimized.

The preferred construction method for the MJS IRIS beamsplitter coating will be the continuously varying layer, if the technical problems associated with a continuous deposition process can be overcome. A backup process will be the finite layer matching scheme used on previous missions.

          2.   Mounting

The extremely low elastic modulus of the Cesium Iodide beamsplitter material requires that particular emphasis be placed on the mounting design for this element. Previous IRIS beamsplitters have been successfully mounted by bonding them into an aluminum housing via an annular ring of RTV-630.

For the MJS IRIS beamsplitter, it is planned to use essentially the same mounting technique; bonding the CsI into place with a flexible adhesive. However, several factors must be considered:

The operating temperature will be 50°K lower than for previous instruments.

The CsI will be bonded to beryllium rather than aluminum, increasing the mismatch of thermal expansion coefficients.

Potentially, these two factors could contribute to an overstressed condition. Partially offsetting the lower temperature and greater difference in thermal expansion coefficients is the reduced size of the CsI beamsplitter. It can be shown that the use of an intervening elastomeric material between components having different thermal coefficients of expansion can produce a system wherein the change in stress on the innermost component is zero over a given temperature range, provided that the elastic modulus of the elastomer does not change greatly. Figure 17 shows a CsI substrate mounted in such a way as to utilize this principle.

Figure 18 presents elastic modulus as a function of temperature, for several elastomeric adhesives. From this figure, it is obvious that the RTV-630 which was successfully used at 250°K, is inadequate at 200°K. During the design study, the selection of a suitable adhesive was recognized as critical to the mounting of the MJS'77 beamsplitter. To date, several candidate adhesive materials have been procurred for test verification of their low-temperature properties. Test fixtures have been fabricated, and preliminary specimens using RTV-630 prepared, primarily to establish handling and testing techniques. Table 3 lists some adhesives considered and Table 4 gives the evaluation criteria to be used.

F. Michelson Motor

A redesign of the MM'71 IRIS Michelson Motor was required in order to meet various spacecraft and instrument requirements for the MJS'77 IRIS. These requirements are reflected in the goals for the Michelson Motor redesign listed below:

1. Reduce external magnetic field to meet space-craft requirements.

2. Increase velocity coil signal to provide more accurate monitoring and control of mirror velocity.

3. Reduce weight.

4. Reduce power required.

5. Optimize dynamic response of motor.

36<

BONDING MATERIAL

.004 INCH

C$_s$I SUBSTRATE

MOUNT

B/S COATING

.004 INCH
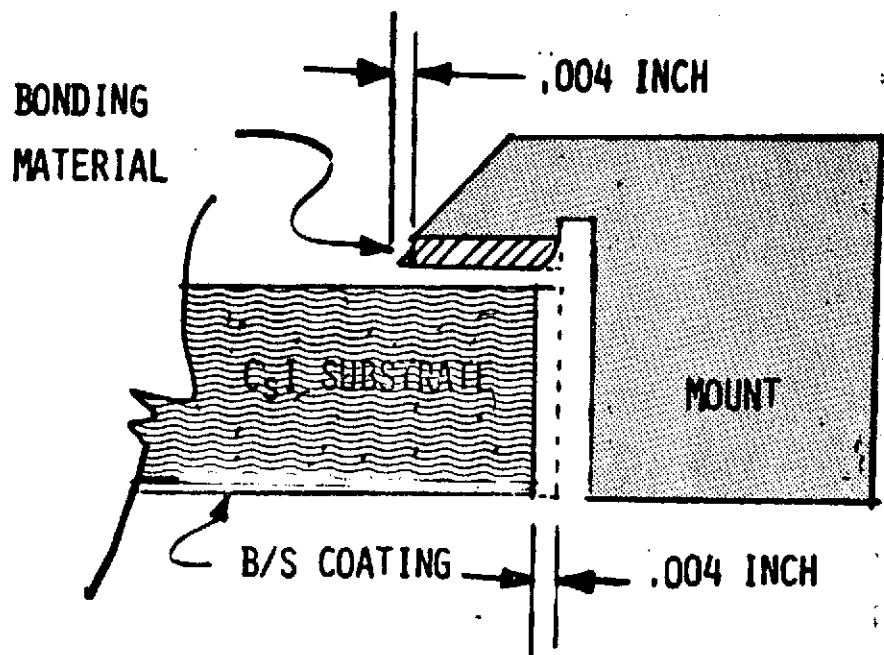
ZERO STRESS MODEL

T = 200°K

FIGURE 17. BEAMSPLITTER MOUNT

37<
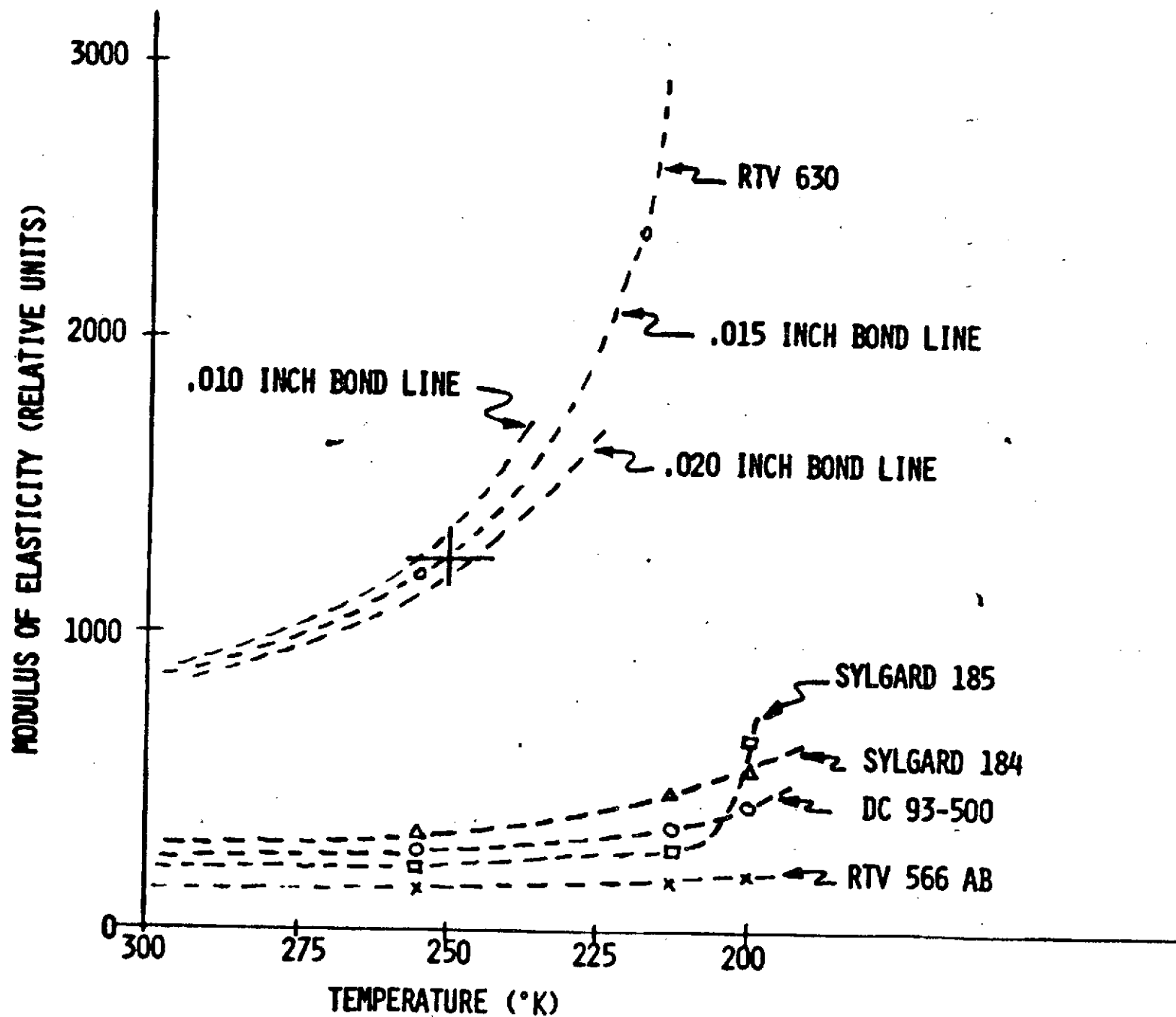
FIGURE 18. ELASTIC MODULUS VS TEMPERATURE

TABLE 3. BONDING MATERIALS

(ALL WITH BRITTLE POINT BELOW -110°C)

● **SPACE GRADE MATERIALS**

  ● DC-61106 (WL .14/VCM .03)

  ● DC-93-500 (WL .35/VCM 0.1, VERY LOW VISCOSITY)

  ● DC-61104 AND DC-61109 (WL .2/VCM 0.1,
                                    MOISTURE CURE)

  ● RTV-566-AB (WL .07/VCM .03, MOISTURE CURE)

OTHER MATERIALS

  ● RTV-566-A/9811 CATALYST (VACUUM CURE)

  ● RTV-560/9811 CATALYST (VACUUM CURE)

  ● RTV-560 (MOISTURE CURE)

  ● SYLGARD 187

  ● RTV-630/655

  ● SYLGARD 185 (VERY LOW VISCOSITY)

  ● SYLGARD 184 (VERY LOW VISCOSITY)

TABLE 4. <u>EVALUATION CRITERIA</u>

- MODULUS OF ELASTICITY VERSUS TEMPERATURE

- BOND STRENGTH -- PRIMERS/CsI/Be

- WEIGHT LOSS/VCM

- VISCOSITY/HANDLING PROPERTIES

- VACUUM CURE CAPABILITY

- LOW TEMPERATURE CURE CAPABILITY

- COMPATIBLE WITH CsI

- REACTION TO SEVERE ELECTRON RADIATION

40<

Measurements made on the external magnetic field of a spare MM'71 Michelson Motor indicated that the velocity pick-up coil was providing most of the leakage flux. The flux at a distance of one meter was found to be 350 nanotesla for the spare motor and only 12 nanotesla for a spare drive circuit housing. Therefore, it was concluded that the velocity pick-up coil was providing the excess flux leakage and that a different design concept was necessary.

The velocity coil design selected consists of a radially magnetized permanent magnet surrounded by an enclosed housing, similar to the drive circuit design. This enclosed housing design should result in a reduced external magnetic field which implies more efficient use of the magnetic flux provided by the magnets. The design is shown in Figure 19.

In order to produce a greater signal from the drive circuit and the velocity pick-up circuit, stronger permanent magnets (samarium-cobalt) will be used in both circuits. With the use of these magnets, for which the demagnetizing curve is shown in Figure 20, a savings in both power and weight and an increase in the velocity coil signal may be realized. Figure 20 shows that for a given value of B/H, that is, for a given geometry, the SmCo magnets provide a higher flux density than the ALNICO 8 magnets which were used on the MM'71 IRIS Michelson Motor. This increase in flux density may be converted into a reduction in power required for operation of the motor. Figure 20 also shows that for a given flux density a smaller value of B/H may be obtained with a smaller magnetic circuit. Since the weight and power required, in general, vary inversely, there is obviously a trade-off concerning the amount of reduction in each which may be obtained. It was necessary to analyze these trade-offs with consideration given to the various system requirements.

In order to meet spacecraft requirements for the static electro-magnetic field at a distance of one meter from the motor, it will be necessary to manufacture the motor housing from a material with higher permeability than steel. The amount of steel which would be necessary to meet the EMI requirement would cause an excess of the motor weight budget. An iron-cobalt alloy called Permendur and its modifications possess extremely high permeability and residual induction. The use of this alloy should provide a means of reducing the external electro-magnetic field to the level specified in the spacecraft requirements. The results of the analysis of external field versus housing material are given in Table 5.

The output of the drive circuit is best expressed in terms of the force/current ratio. The force acting on a single conductor of length L carrying current I, at angle $\emptyset$ to flux density B is given by:

$F = IL \times B$ where F, L, & B are vector quantities

or in scalar form: $F = ILB \sin \emptyset$.
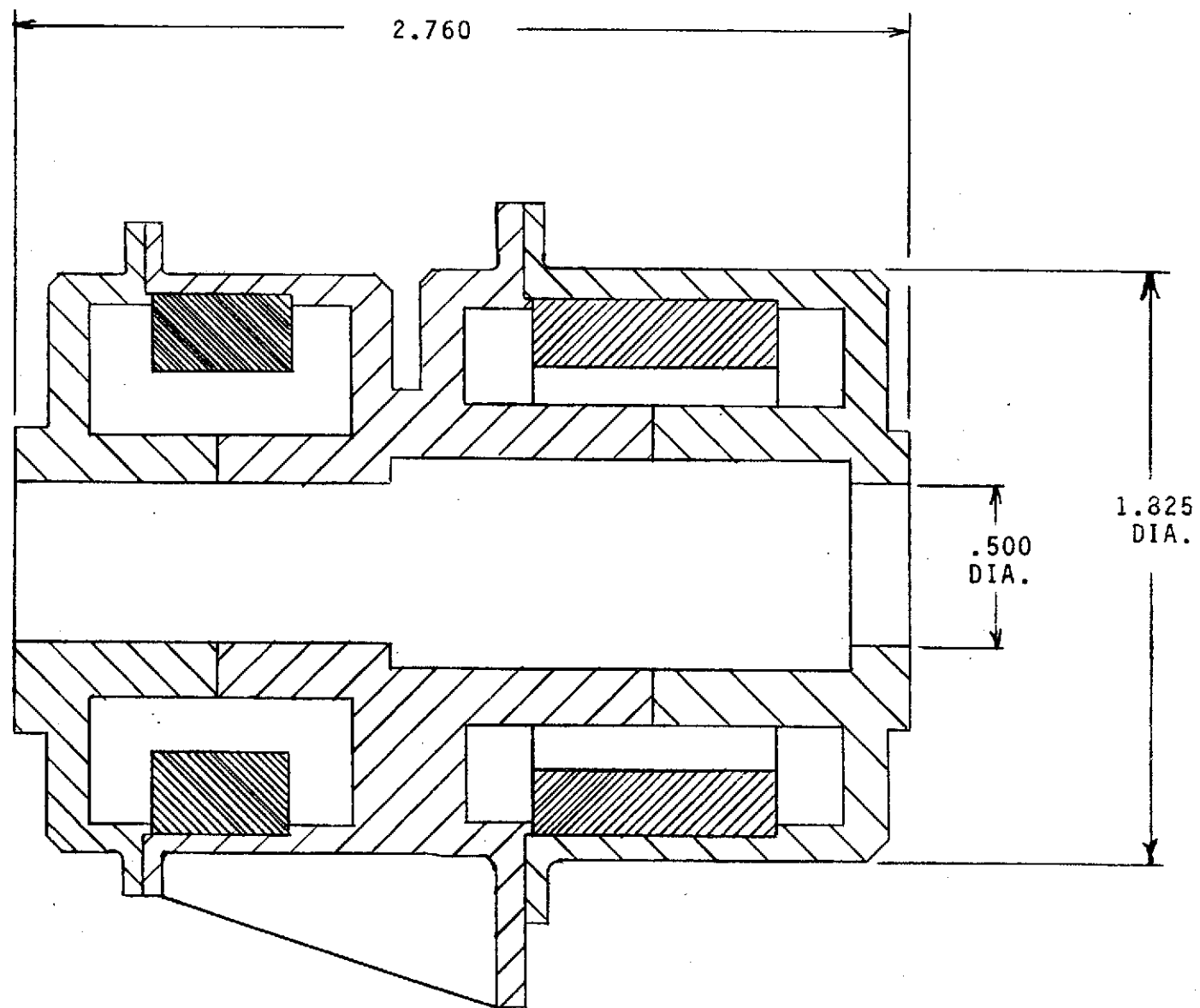
FIGURE 19.   MICHELSON MOTOR HOUSING
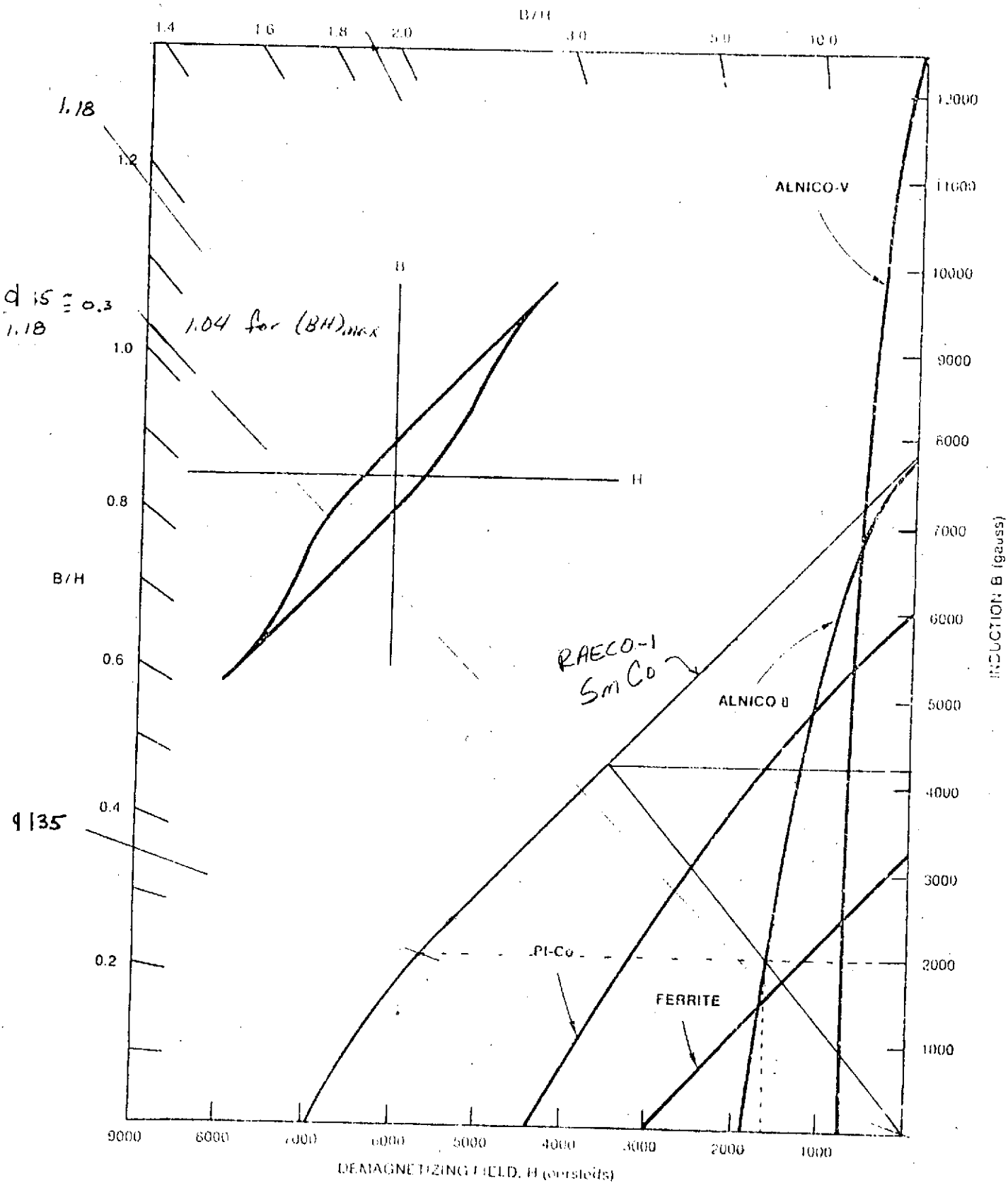
FIGURE 20.

DEMAGNETIZING CURVES FOR SEVERAL PERMANENT
MAGNET MATERIALS COMPARED WITH RAECO-I

36 43<

TABLE 5

MICHELSON MOTOR HOUSING MATERIALS TRADE-OFF

	PERMENDUR (50%Fe,50%Co)	STEEL	DOUBLE-WALL STEEL
STATIC FLUX AT 1 METER (nano tesla)	10	100	20
HOUSING WEIGHT (LB)	1.5	1.42	1.85

For N coils of length L carrying current I perpendicular to flux density B, the total force acting on the coils is:

$$F = NILB$$

and its direction is along an axis mutually perpendicular to L and B and in the direction defined by the cross product of L and B.

The effectiveness of the Michelson Motor magnetic circuit is defined by the force versus current ratio or:

$$\frac{F}{I} = NLB$$

where

N = number of turus

L = length per turn

B = flux density in air gap

For the circuit shown in Figure 19, this value is

$$\frac{F}{I} = 6.24 \frac{lbf}{amp}$$

which compares with a measured value of

$$\frac{F}{I} = 4.42 \frac{lbf}{amp}$$

on the MM'71 IRIS Michelson Motor.

With an effective spring rate of 7.73 lbf/in this gives a mirror displacement versus current ratio of

$$\frac{X}{I} = (4.42 \frac{lbf}{amp})/(7.73 \frac{lbf}{in})$$

$$= .573 \ in/amp$$

For a total mirror travel of .16 cm (.08 cm on each side of the zero current position), the required current is

$$Imax = \frac{(.08 \ cm)}{(2.54 \ cm/in) \ (.573 \ in/amp)} = .055 \ amp$$

$$= 55 \ ma.$$

The current versus position plot is shown in Figure 21.

45<
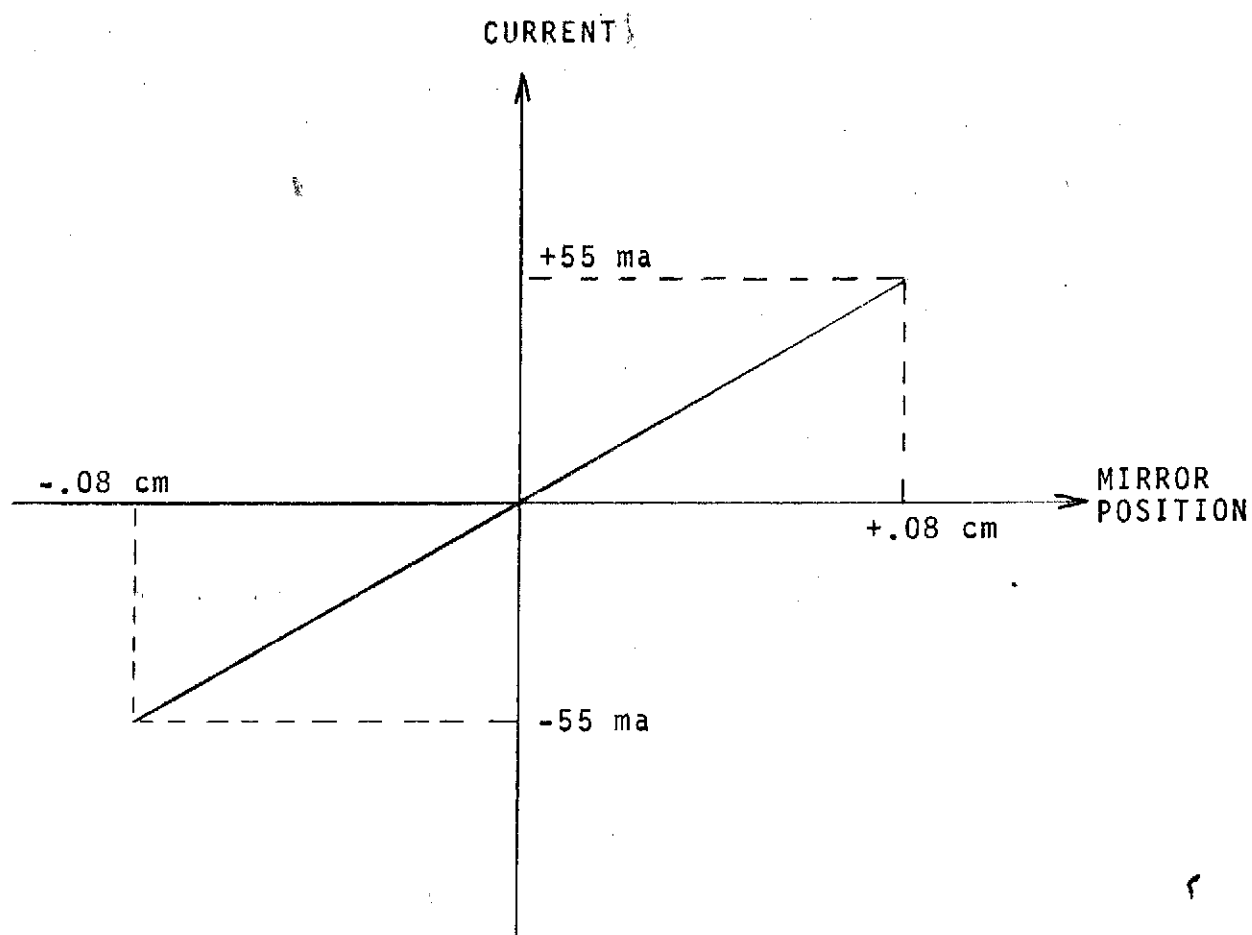
FIGURE 21.

MICHELSON MIRROR POSITION VS DRIVE CURRENT

46<

The coil is wound with approximately 260 feet of #36 wire which has a resistance of .415 ohms/foot or 108 ohms. So the maximum power required to drive the mirror is

$$P = I^2R = (.055 \text{ amp})^2(108 \text{ ohm})$$

$$= .327 \text{ watts}$$

Velocity Coil Signal

The emf generated in a single conductor of length L at an angle ∅ to flux density B and moving at velocity v is

$$V = BLv \sin ∅.$$

So, for N turns of length L positioned perpendicular to a flux density B, the voltage versus velocity ratio is

$$\frac{V}{v} = NBL = 80.0 \frac{V}{m/sec}$$

compared to 8.0 $\frac{V}{m/sec}$ for the MM'71 Michelson Motor velocity coil.

The mirror velocity for the MJS'77 IRIS will be 3.51×10^{-5} m/sec and will provide a signal of

$$V = (80.0 \frac{V}{m/sec})(3.51 \times 10^{-5} \text{ m/sec})$$

$$= 2.8 \text{ mV}$$

compared to 1.875 mV at a velocity of 2.35×10^{-4} m/sec for the MM'71 mirror. The voltage change for 0.50 percent velocity variation is 14 microvolts.

The major design output parameters for the MJS'77 Michelson Motor magnetic circuit and the corresponding values for the MM'71 motor are given in Table 6. Table 7 summarizes the magnetic design changes.

In order to improve the dynamic response of the Michelson Motor, it was first necessary to characterize the reference, MM'71, motor. The motor was modeled as a linear system of springs, masses, and dashpots as shown in Figure 22. The inputs to the system are the force on the mirror shaft due to the current-carrying coils in the magnetic field and the vibrational input to the motor housing. The output of interest is the mirror shaft velocity or position.

After writing the differential equations of motion for the system, these equations may be put into block diagram form as shown in Figure 23. By the use of superposition of inputs and block diagram algebra, the block diagram may be reduced to

TABLE 6
COMPARISON OF MM'71 AND MJS'77
MICHELSON MOTOR MAGNETIC CIRCUIT PARAMETERS

	HOUSING WEIGHT (LB)	POWER REQUIRED (WATTS)	VELOCITY COIL OUTPUT (V/M/S)	SIGNAL AT CONSTANT VELOCITY (mV)
MM'71 (ACTUAL)	2.0	0.35	8.0	1.875
MJS'77 (PREDICTED)	1.5	0.327	80.0	2.80

48<

TABLE 7. MICHELSON MOTOR MAGNETIC DESIGN CHANGES

DRIVE CIRCUIT

Change		Result
(1) Stronger (SmCo) Magnets	(a)	Increased force due to higher flux density
	(b)	Reduce weight
	(c)	Reduce power required
(2) Permendur Housing		Reduce flux leakage

VELOCITY SENSING CIRCUIT

Change	Result
(1) Enclosed Housing Design	Reduce flux leakage by more efficient use of magnetic flux
(2) Increase Number of Turns	Increase output signal
(3) Stronger (SmCo) Magnet	Increase output signal
(4) Permendur Housing	Reduce flux leakage

49<
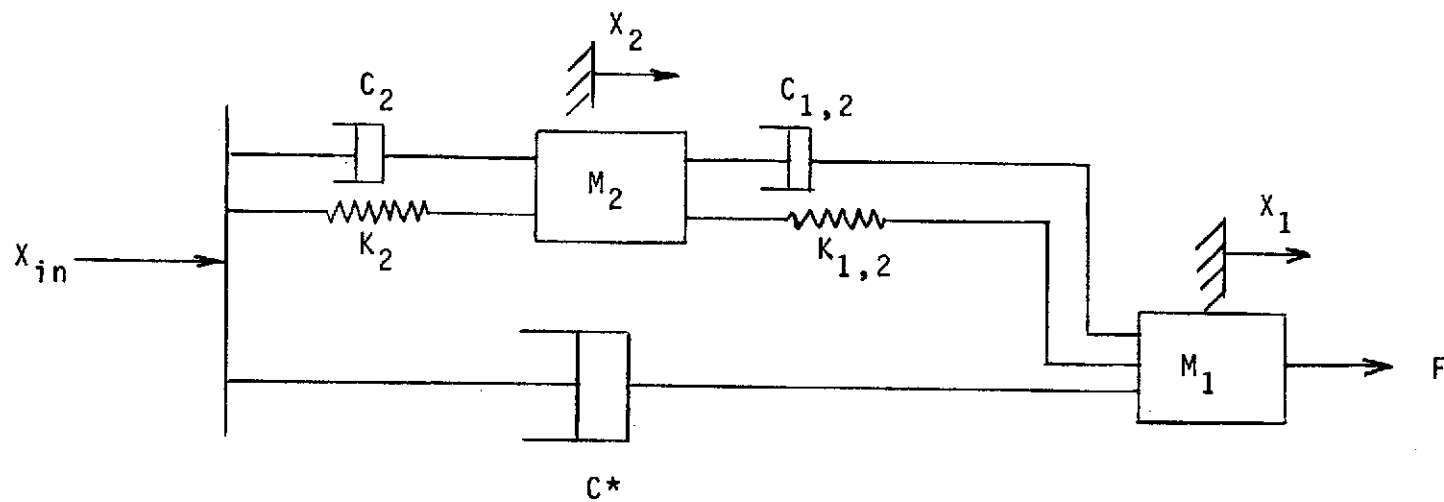
F = Force On Armature.

M_1 = Mass Of Armature

M_2 = Mass of Outriggers

K_2, $K_{1,2}$ = Spring Constants

C_2, $C_{1,2}$ = Damping Constants

C* = Magnetic Damping Constant

X_1 = Position of Armature

X_2 = Position of Outriggers

X_{in} = Vibrational Input to Housing

FIGURE 22.

MICHELSON MOTOR VIBRATIONAL MODEL
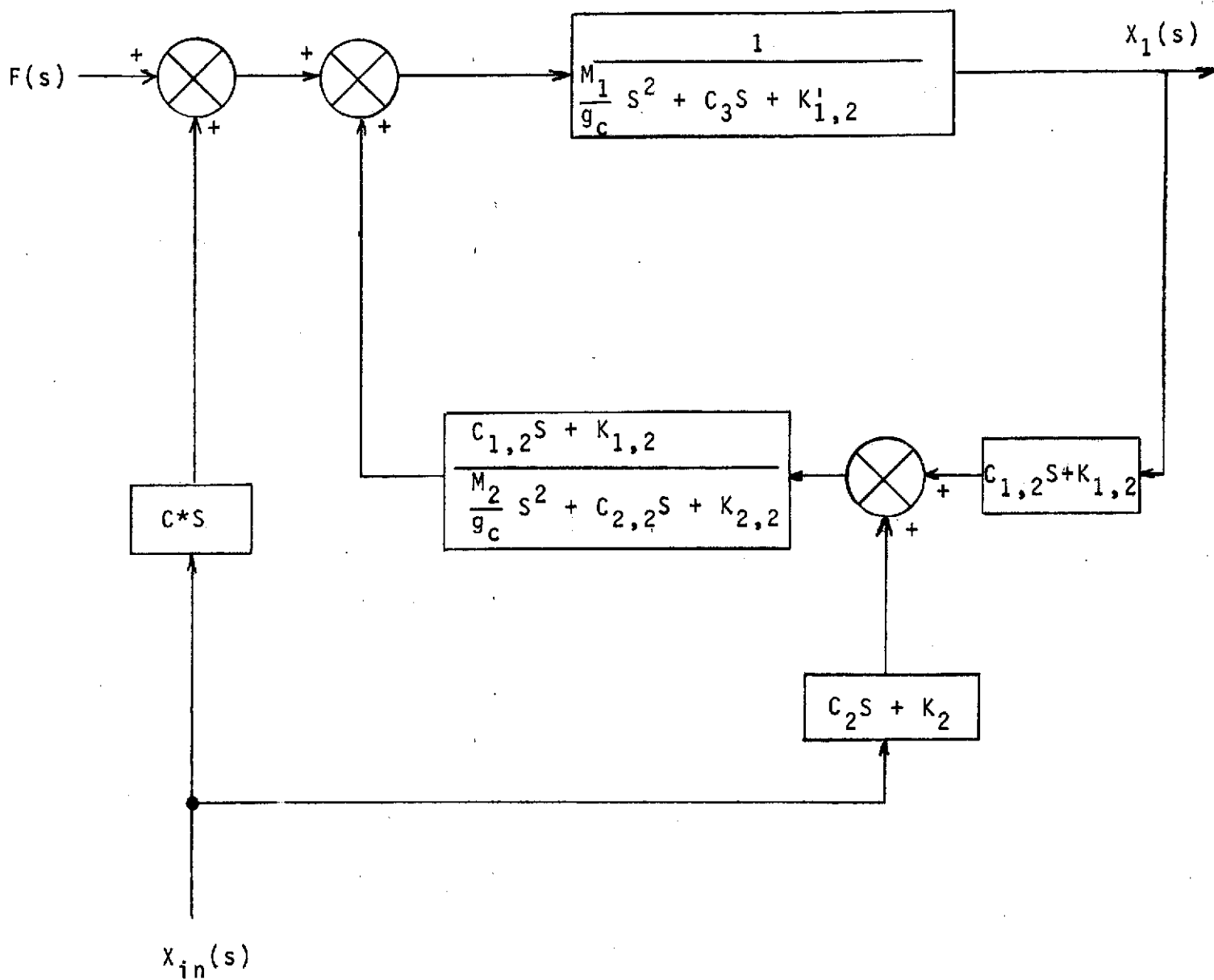
FIGURE 23.
MICHELSON MOTOR MODEL BLOCK DIAGRAM

that shown in Figure 24. This diagram also shows how the effect
of spacecraft vibrational input on mirror motion may be predicted
by determining the transfer function relating the scan platform
motion and the motor housing motion.

Using experimentally and analytically determined
values for the spring constants, masses, and damping constants
for the MM'71 Michelson Motor, the transfer functions $G_2(S)$ and
$G_3(S)$ in Figure 24 were defined. The comparison of the dynamic
response of the modeled motor with experimentally determined
responses for two MM'71 motors is shown in Figure 25.

Since the magnetic damping of the mirror shaft is
proportional to the flux density across the air gap squared, a
much higher damping ratio is expected on the MJS'77 motor. Also,
the use of silicon rubber damping of the outriggers provides
increased damping of the outrigger motion. These changes are
reflected in Figure 26 and Figure 27. Figure 26 shows the dynamic
response of the mirror shaft to an electrical input from the drive
coil. Figure 27 shows the mirror response to vibrational input
to the motor housing. As shown in Figure 27, the increased mag-
netic damping of the mirror shaft has decreased the peak value
of the gain at the mirror resonance but has given a seven db
increase in the gain at high frequencies.

The model will be up-dated with any changes which may
be made to the motor design or with more accurate data as it is
obtained. This model, along with the model relating scan plat-
form vibration to motor housing vibration, will be used as aids
in the design of the phase-locked loop control system.

G.   Purging

Prior to launch, a continuous flow of dry nitrogen
gas through the IRIS must be provided, to protect the hygroscopic
Cesium Iodide beamsplitter. Because of the large openings within
the optical train, some sort of additional flow restriction must
be provided to keep the gas flow rate within reason.

To date, the most viable candidate for a means of
providing this additional flow restriction is a fitted plastic
cover to enclose the telescope. This would provide protection
for the telescope, and has the advantage over a flow restrictor
placed within the instrument in that the risk of instrument
damage during removal is minimal.

H.   Weight Estimate

Table 8 presents the current IRIS & R weight breakdown.
These figures may be expected to change somewhat as the stress
and thermal analyses near completion during the hardware program.
(The numbers given are based on simplified stress calculations,
using deflections which are assumed to be acceptable optically).

52<
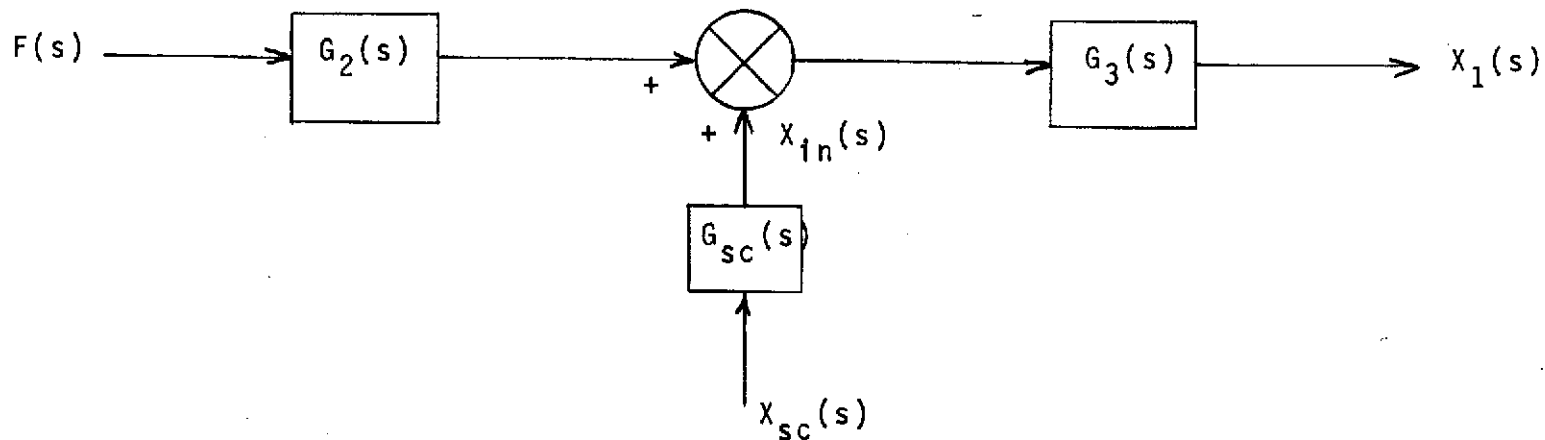
$$G_2(s) = \frac{M_2 S^2 + C_{2,2}S + K_{2,2}}{M_2 C* S^3 + (C*C_{2,2}+C_{1,2}C_2)S^2 + (C*K_{2,2}+C_2 K_{1,2}+C_{1,2}K_2)S + K_{1,2}K_2}$$

$$G_3(s) = \frac{M_2 C* S^3 + (C*C_{2,2}+C_{1,2}C_2)S^2 + (C*K_{2,2}+C_2 K_{1,2}+C_{1,2}K_2)S + K_{1,2}K_2}{M_1 M_2 S^4 + (M_1 C_{2,2}+M_2 C_3)S^3 + (M_1 K_{2,2}+C_3 C_{2,2}+M_2 K_{1,2}-C_{1,2}^2)S^2 + (C_3 K_{2,2}+}$$

$$C_{2,2}K_{1,2}-2C_{1,2}K_{1,2})S+K_{1,2}K_2$$

Where:
$$K_{2,2} = K_2 + K_{1,2}$$
$$C_{2,2} = C_2 + C_{1,2}$$
$$C_3 = C_{1,2} + C*$$

FIGURE 24.   MICHELSON MOTOR TRANSFER FUNCTIONS

FIGURE 25. MM'71 MICHELSON MOTOR RESPONSE
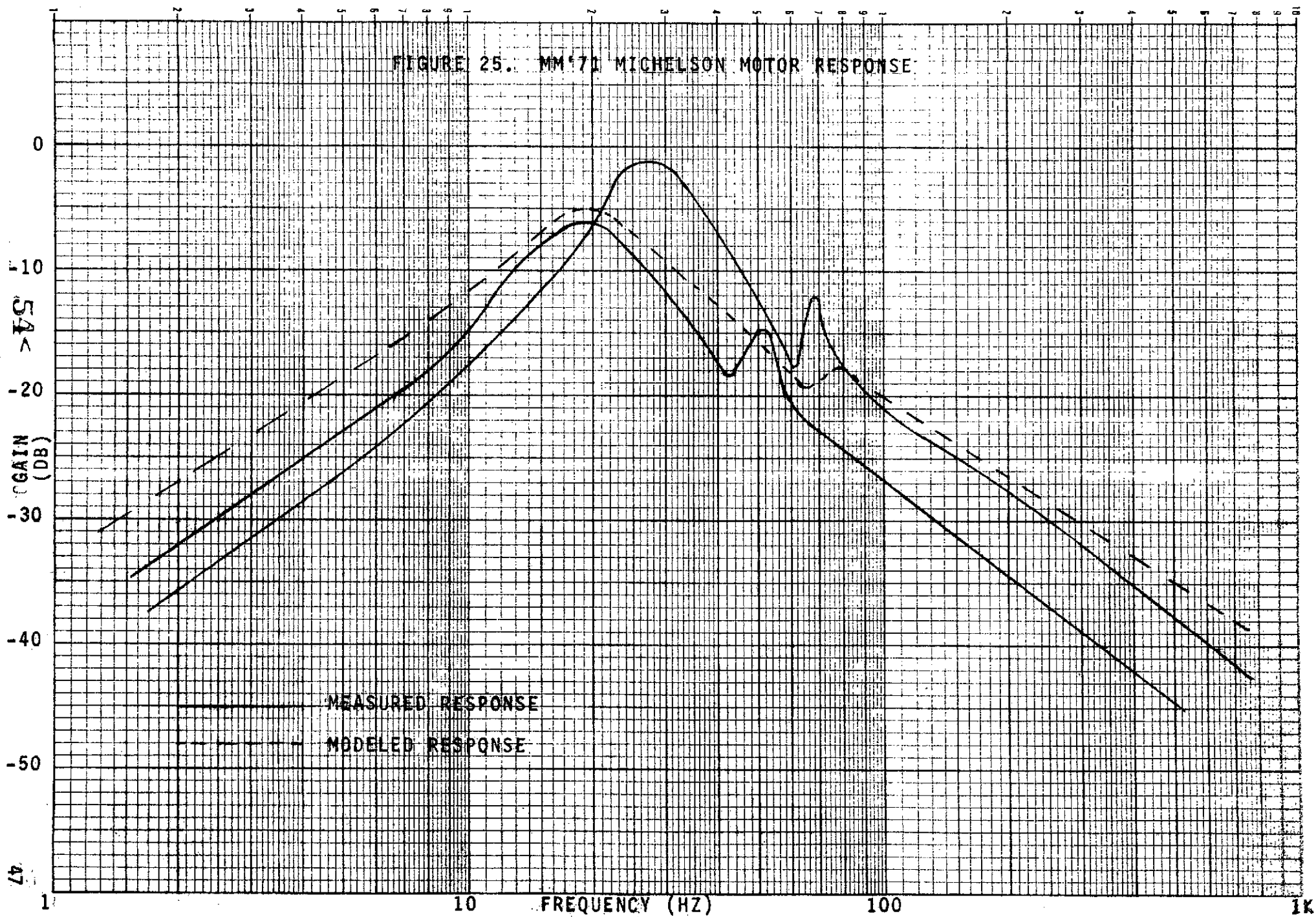
FIGURE 26. MIRROR VELOCITY VS FREQUENCY
FORCE ON SHAFT
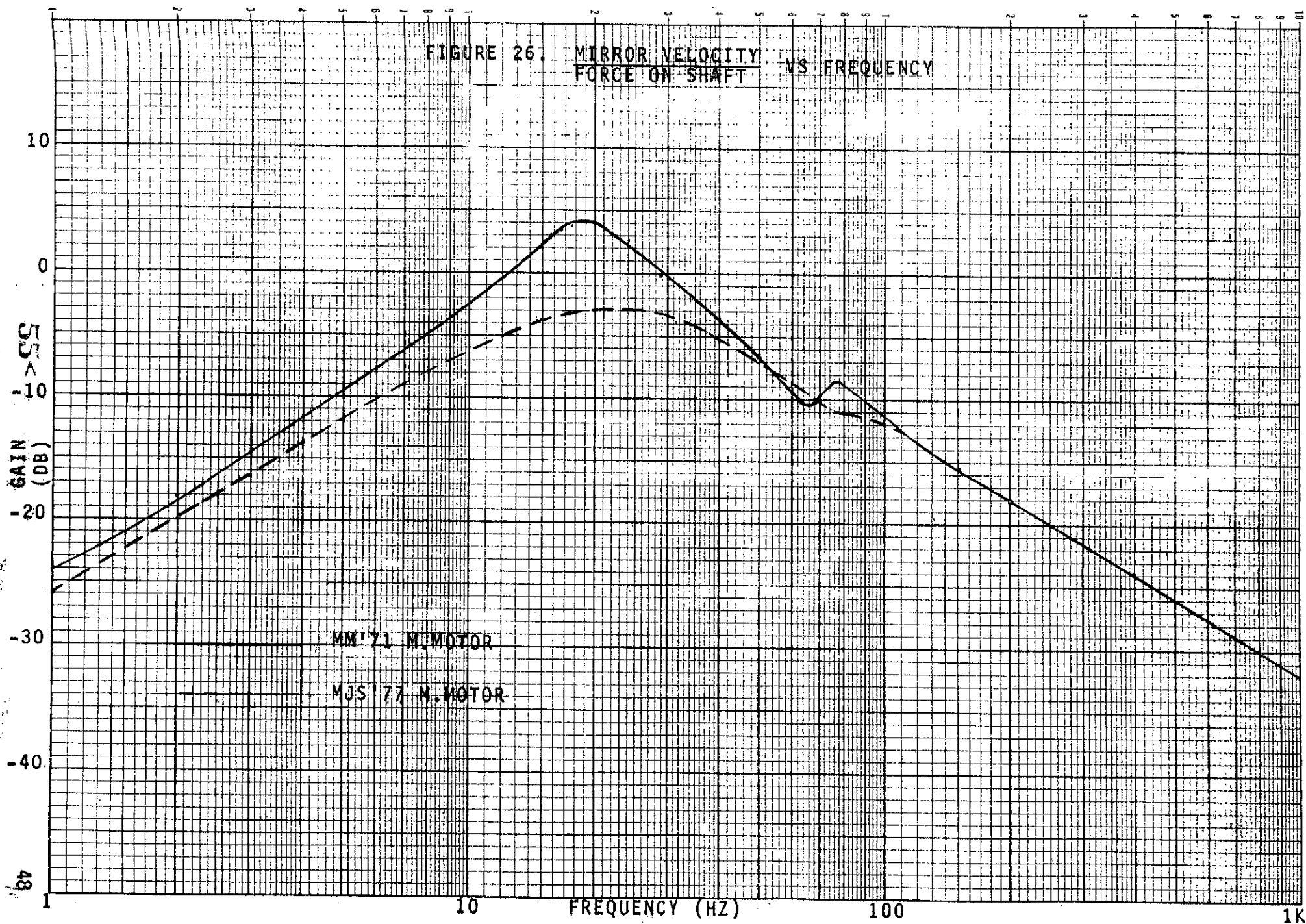
FIGURE 27. MIRROR DISPLACEMENT
HOUSING DISPLACEMENT VS FREQUENCY
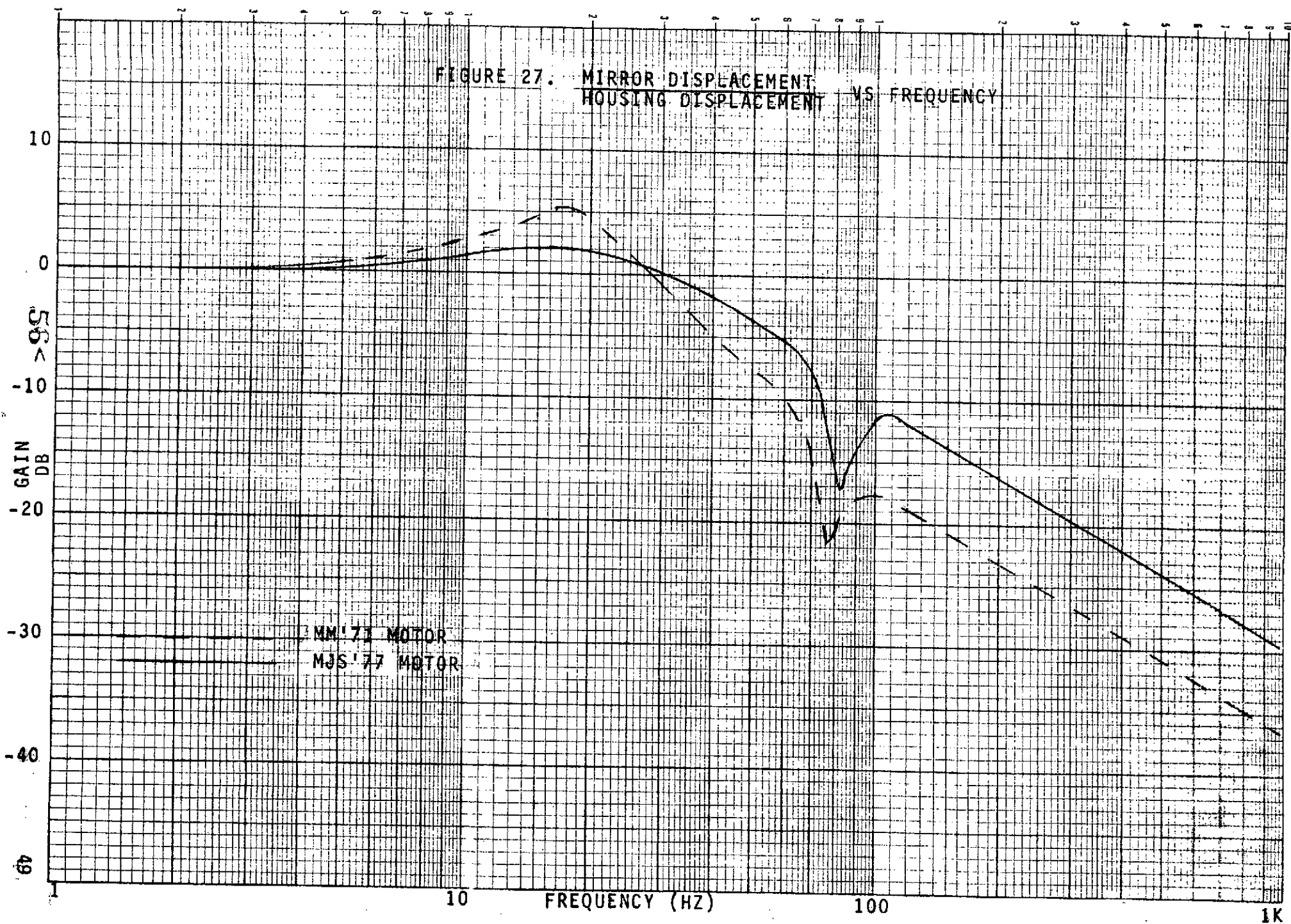
TABLE 8. MJS IRIS & R WEIGHT ESTIMATE

TELESCOPE SECONDARY & SUPPORT	.75	LBS.
TELESCOPE PRIMARY MIRROR	4.00	
INSTRUMENT CENTRAL STRUCTURE	.50	
DICHROIC MIRROR & SUPPORT	.59	
RADIOMETER	.52	
INTERFEROMETER	5.10	
MAIN RADIATOR	.88	
BAFFLING & INSULATION	1.72	
MOUNTING TUBE	.40	
TOTAL	14.46	LBS.

57<

A significant portion of the increased weight (>1.0 pound) is due to the change from an aluminum honeycomb primary mirror to a beryllium one. The estimated 4.0 pounds for this mirror is conservative; however, further analysis will be required to determine exactly how light this critical item can be safely made.

No work was done on the electronics package during the study program, and therefore no updated weight estimate is available.

I.   Telescope Design

1.   Primary Mirror Fabrication

During the design study, major attention has been given to selecting a fabrication method for the telescope primary mirror. Criteria used were:

Desirable weight $\leq$ 3 pounds

Maintain acceptable figure over the temperature range of 300° to 200°K.

Completely elastic behavior under launch conditions

Long-term stability of figure at 200°K

No degradation from exposure to expected radiation levels

Reflectance > 90%, 0.3 to 50 μm

Scatter < 1%, 0.3 to 2.0 μm

The following discussion summarizes the different fabrication methods evaluated.

a.   Replication: In this process, aluminum is sputtered onto a glass master mandrel. A reinforcing substrate (aluminum honeycomb for this application) is then epoxied to the sputtered aluminum film. Thermal shock is then used to separate the replicated surface from the glass master. Generally, a layer of silver is deposited prior to sputtering the aluminum, to aid in removal of the mirror from the master. This process is attractive because the end product is extremely lightweight, and costs to produce are moderate. However, several risk areas exist:

For replicated mirrors larger than about 8 or 10 inches, stress levels in the epoxy film are expected to exceed the adhesion strength of the epoxy at 200° Kelvin. Most probably this failure mode is associated with a type of surface wrinkling described as "orange peel".

Unless the epoxy film is almost infinitesimally thin, the differences in thermal expansion coefficients of the epoxy and aluminum will result in thermal bending at other than the curing temperature.

Expected electron radiation levels will adversely affect the epoxy layer.

There is no adequate history establishing the long-term stability of large replicated mirrors at low temperatures.

b.   Electrodeposition: This is essentially a process of plating material over a glass mandrel to build up whatever thickness is required. Machined structural parts can be "grown" into the deposited material. Surface quality and stability can be quite good. This process was discarded for the MJS for the following reasons:

Materials applicable to the electrodeposition process (nickel or copper, generally) are inconsistent with the three-pound weight goal.

In large diameters, the glass master is frequently destroyed in removing the finished mirror.

c.   Lightweight Aluminum: Assuming that a way could be found to polish it, a minimum weight aluminum primary mirror was designed with launch loads as the only criteria. It was found that this minimum structure would weigh 3.4 pounds. Since aluminum is not directly polishable, nickel coating is required. To avoid bimetallic bending effects, both front and back surfaces would have to be plated. A .005" thick overall nickel coating would weigh approximately 0.9 pounds, leading to a 4.3 pound mirror having marginal strength and doubtful stability.

d.   Beryllium: A beryllium primary mirror machined in an "eggcrate" configuration for reduced weight and enhanced stiffness, appears to be the best choice. The three pound weight goal can be closely approached without jeopardizing mirror stability. Figure 28 depicts a possible mirror configuration. One major advantage in choosing beryllium is that a number of large lightweighted mirrors have been fabricated and evaluated for long-term stability. By utilizing the results obtained from various study programs and by drawing on vendor experience, technical risks can be minimized. A key consideration in selecting a beryllium mirror vendor is the technique used to produce a low-scatter surface, Kanigen (nickel) coating or direct polishing of the beryllium. A discussion of the tradeoffs involved in this choice is given below.

(1)   Kanigen coating: Beryllium suitable for use as a mirror blank is prepared by vacuum hot pressing

WT. = 2.95 LBS

ω_n = 362 HERTZ

.50"

.25"

.08"

2.5"

10.05"

1.5"

.25"

.08"

.63"
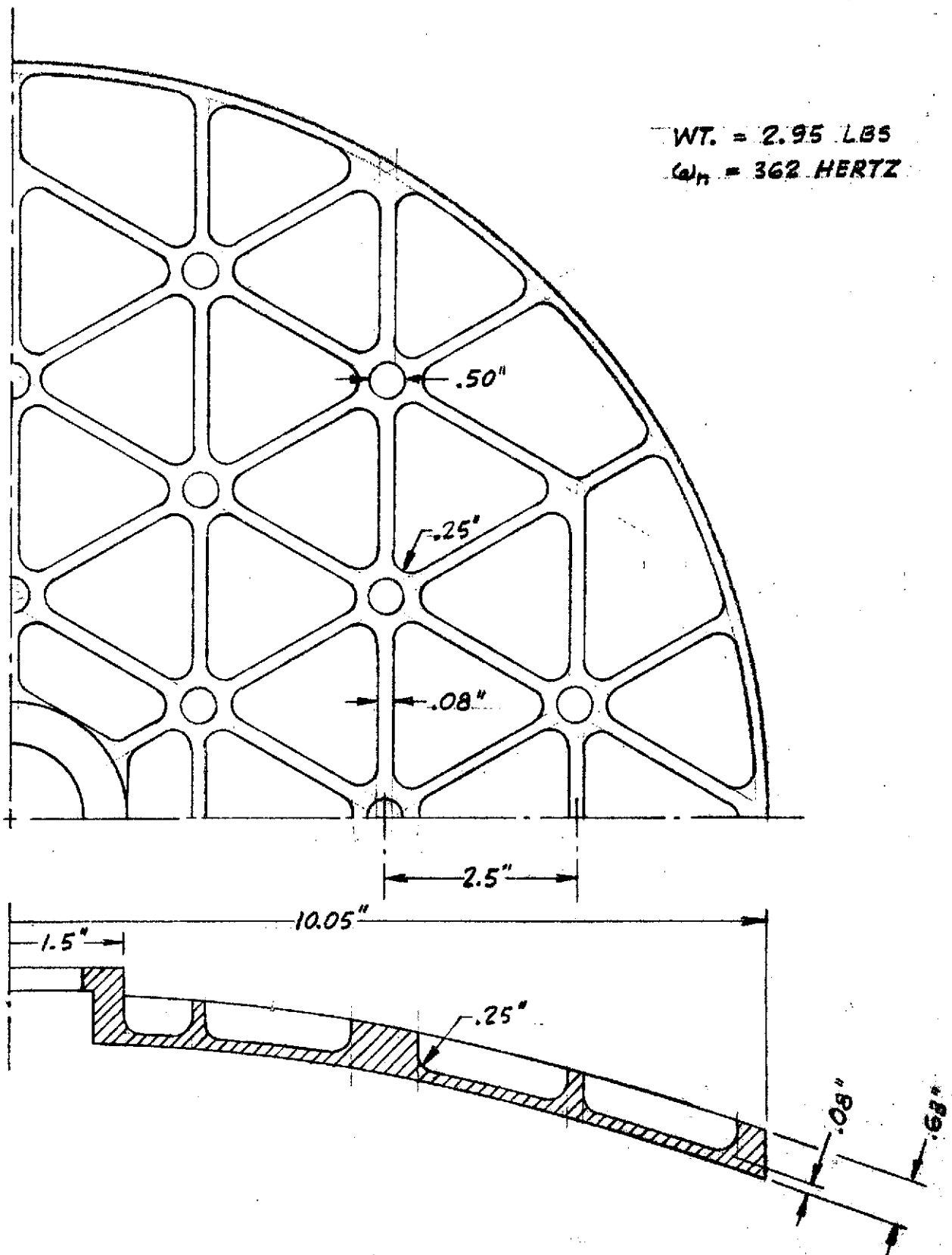
MJS TELESCOPE PRIMARY
PRELIMINARY DESIGN
(PERKIN-ELMER)

FIGURE 28.

or hot isostatically pressing of beryllium powder. Consequently, the polished surface tends to be somewhat grainy. Scattering is high, and the reflectance low in the visible region. Traditionally, Kanigen coatings (an electroless nickel plating process) have been used to provide a polishable surface, circumventing both the scatter and reflectance problems. Kanigen coating is at this time the most generally accepted approach to obtaining an adequate optical surface on beryllium; however, there are some disadvantages.

Kanigen coatings have a history of not adhering well to beryllium. There are reports of peeling, chipping, and delamination occurring a year or more after mirror fabrication.

The nickel coating would add almost a pound of weight to a 20-inch diameter mirror.

Bimetallic bending effects are introduced.

A high (33,000 psi) interface stress level is reported to be inherent in the Kanigen process. This effect can be expected to cause long-term dimensional creeping of the relatively weak optical grades of beryllium.

(2)   Polished Bare Beryllium: In view of the apparent problems associated with Kanigen coating, at least one mirror vendor (Perkin-Elmer) has been actively working to achieve low-scatter surfaces by direct polishing with various chemical/mechanical polishing techniques. Figure 29 presents results obtained as of December 1973. The curves of Figure 29 represent the Bidirectional Reflectance Distribution Function (BRDF), with units of watts scattered/watt incident/steradian, versus angle of incidence. Perkin-Elmer reports achieving values for total visible integrated scatter between 0.03 and 0.06 percent, polishing on bare optical grades of beryllium. Also shown on Figure 29 is a scattering curve obtained by sputtering beryllium powder onto a polished beryllium surface, indicating the possibility of achieving performance equivalent to that of a polished nickel mirror. Finally, visible reflectance is augmented as shown in Figure 30 by vapor deposition of aluminum.

e.   Recommendations: Machined beryllium appears to be the only truly suitable fabrication method for the MJS primary mirror. Technical risks are confined to the question of surface preparation (bare versus nickel-coated) and the weight goal is most nearly met. With an all beryllium system, thermal interface stresses are eliminated, and thermal gradient control should be very good.

Three beryllium mirror vendors are under active consideration; Speedring, Applied Optics, and Perkin-Elmer. Currently, Texas Instruments is working with these vendors
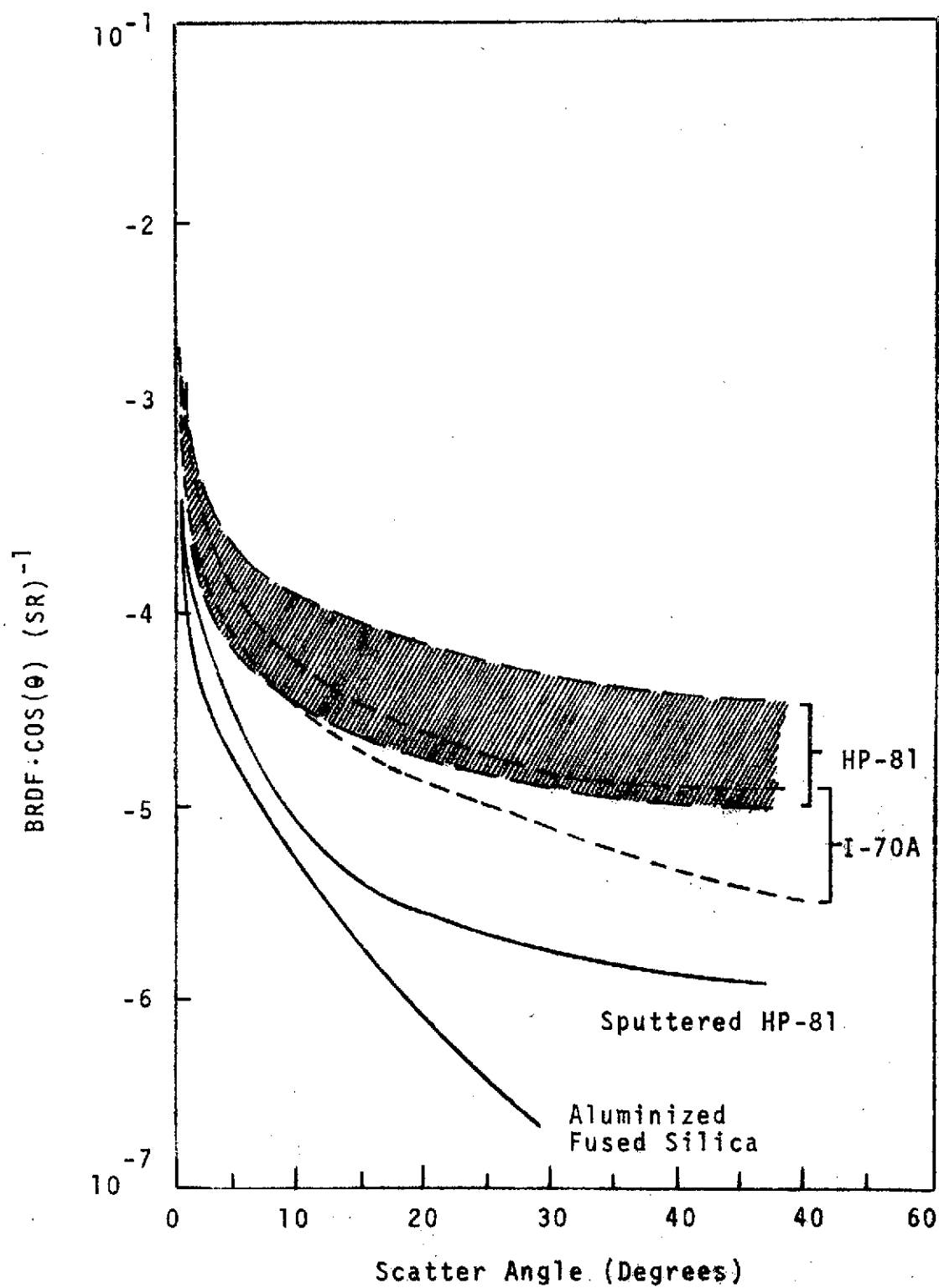
61<

FIGURE 29.

SCATTER AT 10.6μM OF POLISHED BERYLLIUM

62<
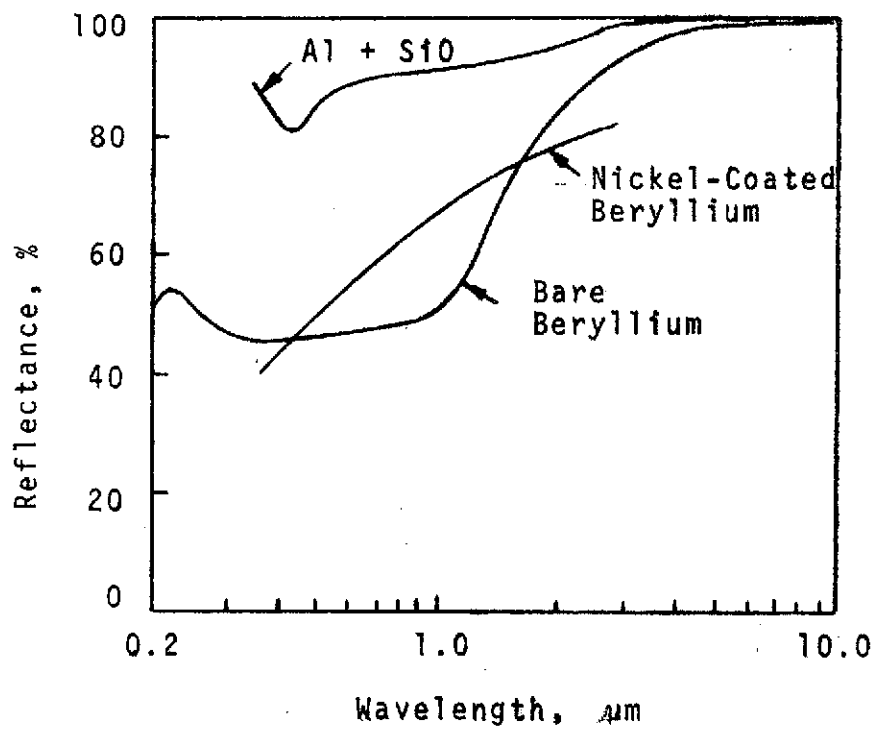
REFLECTANCE COMPARISON

FIGURE 30.

to determine the most cost and weight effective approach. The following points and questions are primary considerations:

Speedring and Applied Optics claim that carefully controlled electroless nickel coatings (not the proprietary Kanigen process) produce stable mirrors. The long-term history of such optics produced by these vendors is being investigated. Nickel coating is still of interest because the cost savings can be considerable, relative to bare polished beryllium.

Some technical risk is incurred with bare beryllium, in that Perkin-Elmer's techniques have been developed on flat mirrors of about 3" diameter and less. A 20" parabola would be expected to have somewhat more scatter.

Cost and risk both vary appreciably as weight is reduced; machining time, polishing time, risk of damage in handling, and the possibility of "print through" of the rib pattern all must increase as weight decreases. As an example, a 3.0 pound bare beryllium primary mirror would be a fairly conservative design, with no particular difficulties in design or fabrication. Plating this mirror would reduce the total cost, but the weight would then be approximately 3.6 pounds. If the total weight is to be held at 3.0 pounds, then the beryllium substrate must weigh 2.4 pounds; the additional cost to accomplish this would almost certainly offset any cost savings realized through nickel plating.

2.   Secondary Mirror and Support

Figure 31 shows the configuration chosen for positioning the telescope secondary mirror with respect to the primary mirror. Figure 32 pictorally represents the configuration of the beryllium support structure.

The secondary mirror is mounted and adjusted as discussed above, using rotatable wedge rings. Structurally, the secondary support member consists of three tapered ribs located 120° apart. The tubular section serves primarily to provide torsional coupling for the ribs, and to support the optical baffles.

Figure 31 shows the secondary support structure screwed to the IRIS central structure, and clamping the primary mirror in place. This somewhat unconventional approach to retaining a metal mirror has been tentatively selected in anticipation of a need to maximize the thermal contact area for both the secondary support and the primary mirror. As a consequence of this choice, extreme precision and flatness ($\sim 1\lambda$) will be required on all involved interfacing surfaces to avoid primary mirror distortions. Fortunately, a mirror retention scheme similar to this has already been tried and found successful, with careful attention to lapping of surfaces and torquing of the screws.

64<

PRIMARY MIRROR
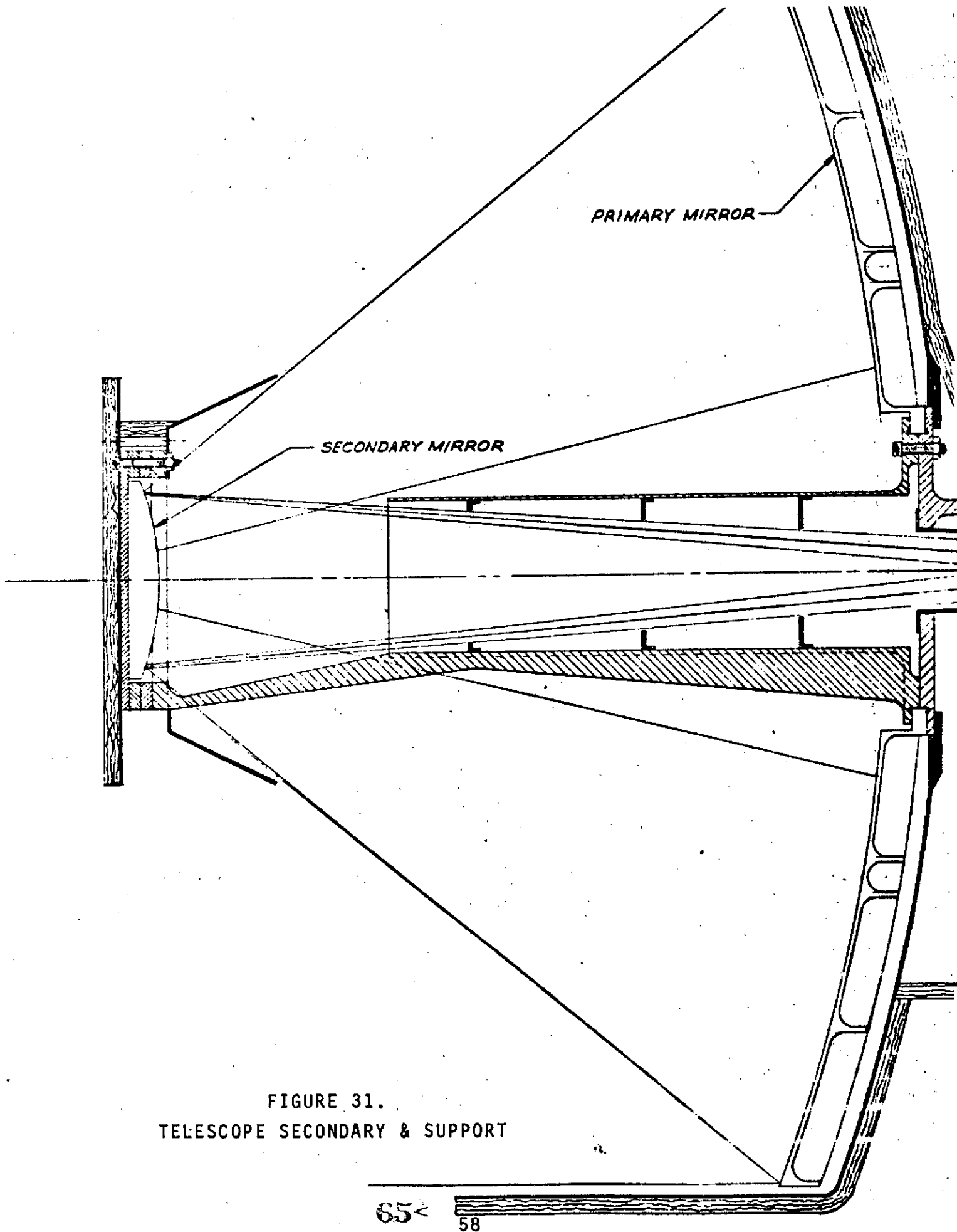
SECONDARY MIRROR

FIGURE 31.
TELESCOPE SECONDARY & SUPPORT

65<
58
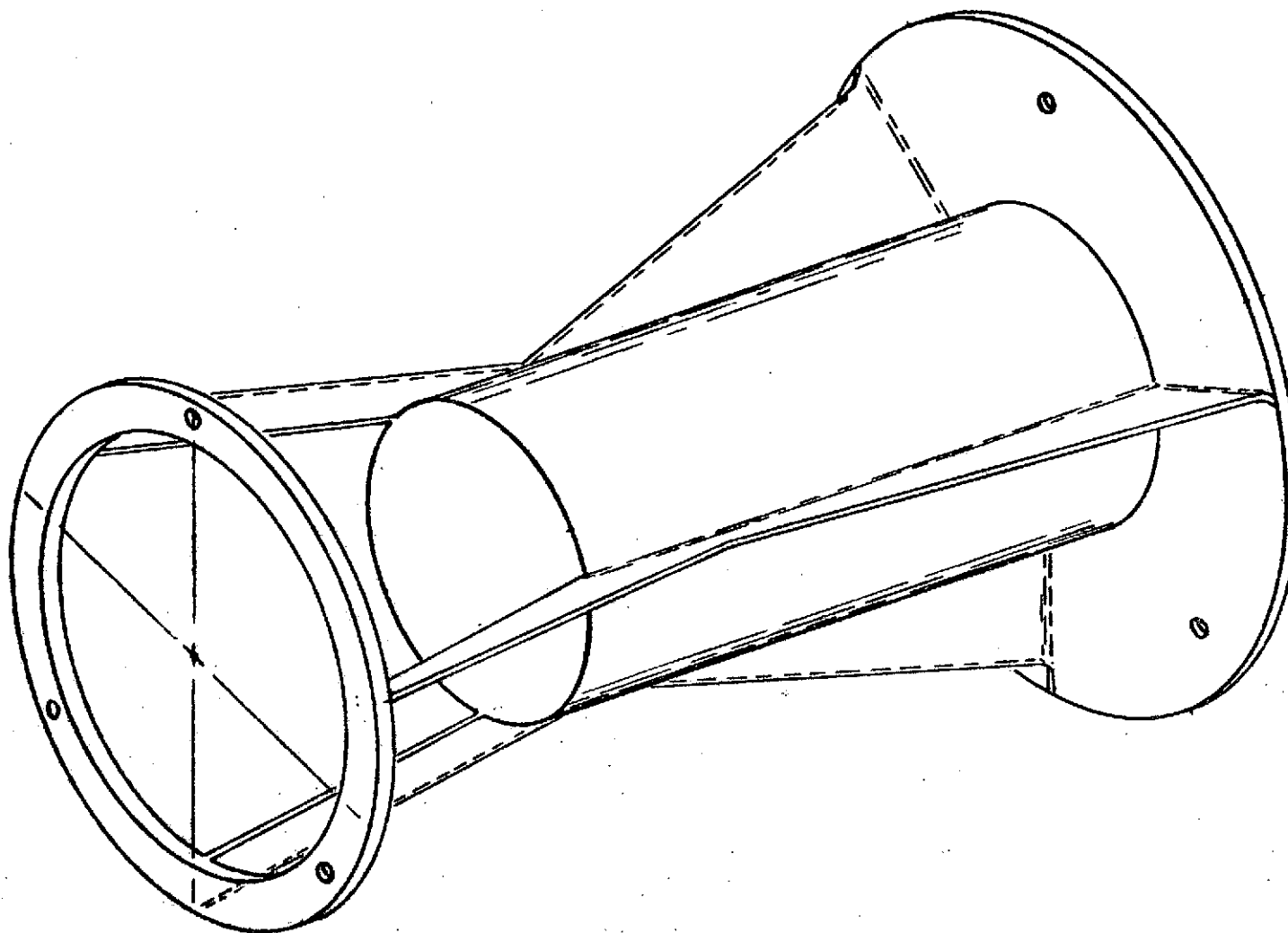
FIGURE 32. SECONDARY MIRROR SUPPORT

IV. ELECTRONIC DESIGN

A. Data Channel Analysis

In order to perform the required data channel analyses, a digital simulation of the data channel has been constructed. Presently, there are still problems in the simulation. These problems will be corrected and the analyses completed early in the MJS IRIS hardware program. Goals of these analyses are as follows:

1. Select IR filter function based on tradeoffs of effects of detector/electronic noise and effects of mirror perturbations on system NER.

2. From above analysis, determine allowable neon phase jitter, thus specifying PLL performance requirements.

3. Determine required neon S/N ratio in order not to degrade NER.

4. Determine time delay accuracy requirements in order not to degrade NER.

A block diagram of the data channel simulation is shown in Figure 33. A more detailed description of the simulation model is included as Appendix A of this report. Capabilities of the data channel model include the items listed below:

1. Sinusoidal or random Michelson mirror perturbations may be specified.

2. IR detector/electronic noise may be specified.

3. Neon signal/noise ratio may be specified.

4. Zero crossing detector threshold values may be specified, simulating threshold errors, hysteresis, etc.

5. Time delay error may be specified, as well as shift register clock periods.

6. Filter frequency breakpoint and roll-off rate may be specified.

7. Number of ADC quantization bits may be specified.

8. In the N1 X N2 summation, N1 and N2 may be specified.

9. Can specify plot of signal (or spectrum) at any of numbered points of Figure 33.

67<
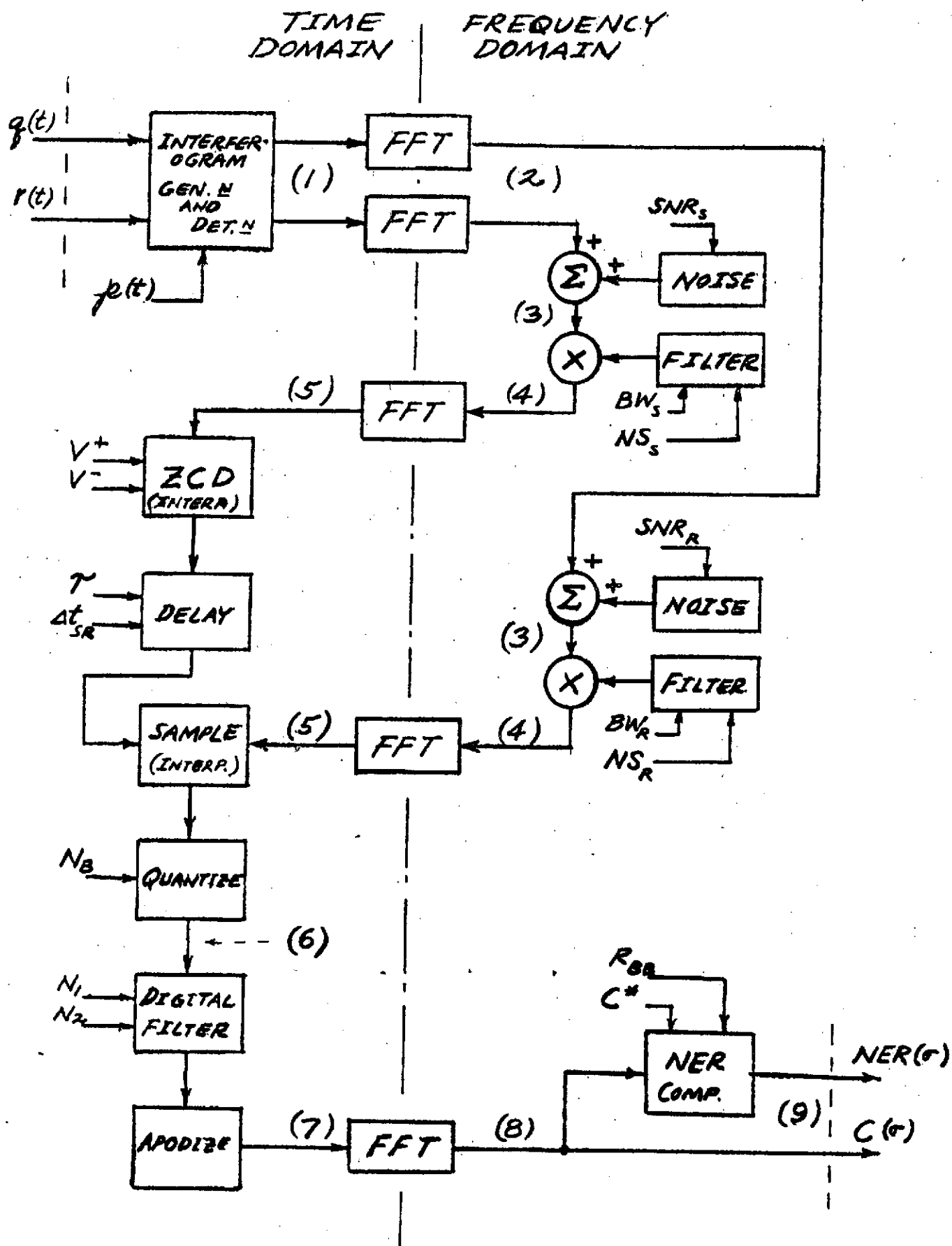
Figure 33. Block Diagram of the IRIS Interferometry Simulation

61

68<

10.   The effects of above items on system NER may
      be observed.

Typical output of the model is shown in Figure 34.
This figure shows (1) the blackbody function for a $200^\circ K$ blackbody,
(2) system NER resulting from a 0.3 radian/30 Hz modulation of
the neon frequency for an electronic filter bandwidth of 56 Hz,
and (3) the error as a function of wave number due to the modulation.

B.   Michelson Motor Drive Phase Lock Loop

Effort on the phase lock loop (PLL) during the design
study consisted of:

1.   Reviewed IRIS-71 PLL design with respect to
     vibration performance.

2.   Looked at alternate implementations of PLL - did
     not identify a better approach than present one.

3.   Supported Michelson motor design effort by
     evaluating changes to motor response charac-
     teristics (with respect to PLL vibration
     performance).

The design requirements for the PLL as specified in
the Statement-of-Work (SOW) are listed in Table 9. The major
design task in the PLL design is to minimize the effects of vibra-
tion inputs to Michelson mirror velocity.

A block diagram of the PLL showing vibration inputs
is shown in Figure 35. The vibration input from the spacecraft
is applied to the PLL components through G4 and G5, the mechanical
transfer functions from the spacecraft to the Michelson motor
support and the optics supports respectively. The motor transfer
function is divided into G2 and G3 so that the vibration is applied.
at the appropriate location. The disturbance input to the motor
support, U_1 (S), is the primary concern since the Michelson mirror
is spring mounted to the motor support.   From Figure 35, the
phase error due to disturbance U_1 (S) is

$$\frac{\phi_{out}}{U_1(S)} = \frac{1}{G_p G_1 G_2} \left(\frac{\phi_{out}}{\phi_{ref}} \right)$$

The phase error due to disturbance $U_2(S)$ is

$$\frac{\phi_{out}}{U_2(S)} = G_{pp} \left(1 - \frac{\phi_{out}}{\phi_{ref}} \right)$$

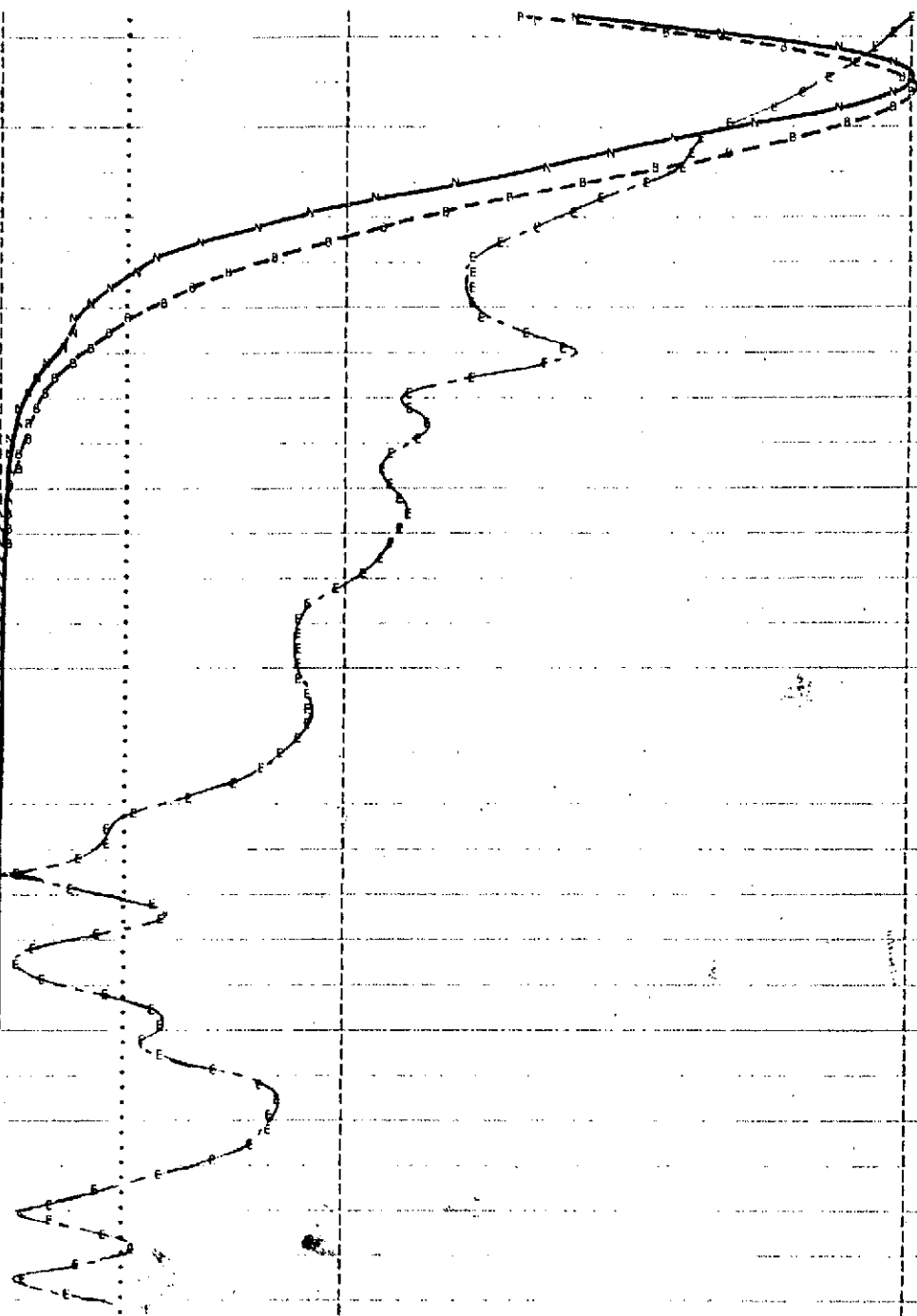The symbols used are defined in the figure.

69<

WAV.NO. STD.DEV. dBR NER

I	(C-C*)	(WATT CM)
CM.	C*	(CM**2 STER)

RELATIVE MAGNITUDES OF NER (N) AND 200-DEGREE KELVIN BLACKBODY RADIANCE (B)

X133   X13-6   X13-9   0 ****** 0.1 ***** 0.2 ***** 0.3 *****,0.4 ***** 0.5 ***** 0.6 ***** 0.7 ***** 0.8 ***** 0.9 ****** 1

178.70	0.1238	2.600	3.218
223.17	0.1212	3.332	4.040
268.05	0.1193	3.707	4.663
312.72	0.1164	4.298	5.004
357.40	0.1128	4.507	5.085
402.07	0.1094	4.551	4.978
446.75	0.1048	4.456	4.668
491.42	0.0987	4.252	4.193
536.10	0.0945	3.471	3.767
580.77	0.0943	3.640	3.431
625.45	0.0927	3.283	3.042
670.12	0.0875	2.920	2.553
714.83	0.0816	2.564	2.093
759.47	0.0776	2.227	1.728
804.15	0.0732	1.915	1.402
848.82	0.0677	1.632	1.105
893.50	0.0645	1.380	0.893
938.17	0.0648	1.158	0.753
932.85	0.0650	0.565	0.627
027.52	0.0638	0.800	0.513
072.20	0.0655	0.659	0.432
116.87	0.0720	0.540	0.383
151.55	0.0772	0.441	0.343
236.22	0.0739	0.358	0.264
253.90	0.0638	0.289	0.185
295.57	0.0561	0.233	0.131
340.24	0.0556	0.187	0.104
384.92	0.0577	0.150	0.086
429.59	0.0567	0.120	0.068
474.27	0.0554	0.095	0.051
518.94	0.0520	0.075	0.033
553.62	0.0533	0.060	0.032
608.29	0.0549	0.047	0.026
652.97	0.0554	0.037	0.021
697.64	0.0547	0.029	0.016
742.32	0.0533	0.023	0.012
736.99	0.0516	0.018	0.009
831.67	0.0440	0.014	0.007
975.34	0.0452	0.011	0.005
021.02	0.0419	0.008	0.004
065.59	0.0408	0.007	0.003
013.37	0.0413	0.005	0.002
055.04	0.0413	0.004	0.002
099.72	0.0410	0.003	0.001
144.39	0.0412	0.002	0.001
193.07	0.0418	0.002	0.001
233.74	0.0423	0.001	0.001
278.42	0.0422	0.001	0.000
323.09	0.0407	0.001	0.000
367.77	0.0380	0.001	0.000
412.44	0.0353	0.000	0.000
457.11	0.0317	0.000	0.000
501.79	0.0256	0.000	0.000
546.46	0.0199	0.000	0.000
591.14	0.0154	0.000	0.000
635.81	0.0146	0.000	0.000
633.49	0.0116	0.000	0.000
725.16	0.0328	0.000	0.000
769.84	0.0101	0.000	0.000
814.51	0.0207	0.000	0.000
859.19	0.0218	0.000	0.000
903.86	0.0136	0.000	0.000
948.54	0.0043	0.000	0.000
993.21	0.0019	0.000	0.000
037.89	0.0067	0.000	0.000
082.55	0.0146	0.000	0.000
127.24	0.0207	0.000	0.000
171.91	0.0219	0.000	0.000
216.59	0.0203	0.000	0.000
261.26	0.0223	0.000	0.000
305.94	0.0293	0.000	0.000
350.61	0.0359	0.000	0.000
195.29	0.0381	0.000	0.000
139.96	0.0376	0.000	0.000
184.64	0.0367	0.000	0.000
229.31	0.0343	0.000	0.000
173.99	0.0293	0.000	0.000
418.66	0.0220	0.000	0.000
463.33	0.0118	0.000	0.000
738.01	0.0076	0.000	0.000
552.68	0.0040	0.000	0.000
597.35	0.0146	0.000	0.000
542.01	0.0184	0.000	0.000
586.71	0.0106	0.000	0.000
731.38	0.0043	0.000	0.000
776.06	0.0135	0.000	0.000
720.73	0.0212	0.000	0.000

NOISE EQUIVALENT RADIANCE STATISTICS   (WATT CM)/(CM**2 STER)

MEAN VALUE, NER	0.68944517E-09
VARIANCE, NER	0.20350397E-17
STD. DEVIATION, NER	0.14265482E-08
MAX. VALUE, NER	0.50850346E-08

POWER DENSITY SPECTRUM ERROR STATISTICS   (PERCENT, REL. TO THE *IDEAL* CASE)

MEAN VALUE, PDS ERR.	0.47069393E-01
VARIANCE, PDS ERR.	0.97994646E-03
STD. DEVIATION, PDS ERR.	0.31304095E-01
MAX. VALUE, PDS ERR.	0.12377244

70<

FIGURE 34.   DATA CHANNEL MODEL OUTPUT FORMAT

FIGURE 35. PLL BLOCK DIAGRAM
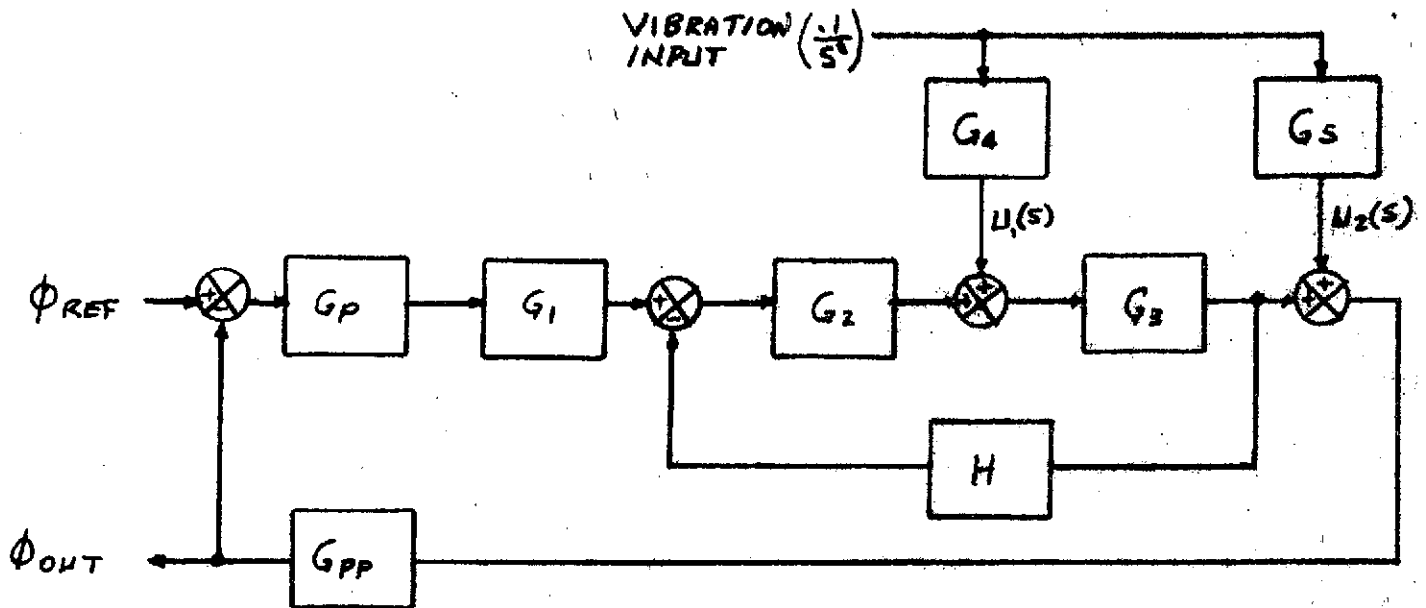
G_p = GAIN OF PHASE COMPARATOR (VOLTS/RADIAN)

$G_1(S)$ = TRANSFER FUNCTION OF LEAD NETWORKS & INTEGRATORS

$G_2(S)$ $G_3(S)$ = TRANSFER FUNCTION OF MOTOR

G_{PP} = GAIN OF NEON DETECTOR (RADIAN/METER)

G_4 = MECHANICAL TRANSFER FUNCTION, SPACECRAFT INTERFACE TO MICHELSON MOTOR SUPPORT

G_5 = MECHANICAL TRANSFER FUNCTION, SPACECRAFT INTERFACE TO OPTICS SUPPORT

$U_1(S)$ = DISTURBANCE INPUT TO MICHELSON MOTOR SUPPORT

$U_2(S)$ = DISTURBANCE INPUT TO OPTICS SUPPORTS

PHASE ERROR DUE TO $U_1(S)$

$$\frac{\emptyset OUT}{U_1(S)} = \frac{1}{G_p G_1 G_2} \left(\frac{\emptyset OUT}{\emptyset REF}\right)$$

PHASE ERROR DUE TO $U_2(S)$

$$\frac{\emptyset OUT}{U_2(S)} = G_{PP} \left(1 - \frac{\emptyset OUT}{\emptyset REF}\right)$$

71<

By using the transfer functions from the IRIS-71 PLL design and a .01G sinusoidal vibration input for $U_1(S)$ the phase error as a function of vibration frequency was computed and is shown in plot (1) of Figure 36. Plot (2) of the figure shows the effects of the measured mounting feet transfer function (G4 of Figure 35) on plot (1). Plot (3) shows data extrapolated from measured IRIS-D PLL vibration data. As can be seen from the figure, the major phase error problem (due to vibration input) occurs in the frequency range which coincides with the mounting feet resonance and the motor outrigger resonance.

Using the most recent model for the MJS motor design, the phase error plot for .01G vibration input was determined and is shown in plot (1) of Figure 37. The error is slightly higher above 20 Hz than is shown in Figure 36, plot (1), for the IRIS'71 design. Plot (2) of Figure 37 shows the effects of the estimated mechanical transfer function from the spacecraft to the Michelson motor support (G4 of Figure 35) for the MJS IRIS design.

In reviewing the PLL design, it was determined that the following should be done to optimize PLL vibration performance:

1. Maximize optics mount resonant frequency

2. Minimize effects of outrigger resonance

3. Minimize velocity loop bandwidth

4. Maximize PLL closed loop bandwidth.

TABLE 9. PLL DESIGN REQUIREMENTS

1.	Mirror Travel		≥ 0.16 cm during output data sampling
2.	Mirror Velocity	$=$	3.51×10^{-3} cm/sec
3.	Mirror Velocity Control		(a) constant within 0.5% under specified operational temperature and vibration
			(b) constant within 0.1% if vibration minimized
4.	Neon Frequency	$=$	120 Hz
5.	Operational Vibration		≤ 0.01 G's (0 to peak) over a sinusoidal frequency of 5 to 640 Hz

FIGURE 36.

Chart labels:
- (1 RAD), (db), (.1 RAD), (.01 RAD)
- PHASE ERROR
- (3) EXTRAPOLATED FROM MEASURED DATA (IRIS-D)
- (2) PLOT (1) WITH MEASURED MOUNTING FEET TRANSFER INCLUDED
- (1) COMPUTED ERROR WITH OUT RIGGERS MODELED AS ONE DEGREE OF FREEDOM (IRIS-II MOTOR)
- PHASE ERROR DUE TO .01 G VIBRATION (SINUSOIDAL) APPLIED VS FREQUENCY OF VIBR. (IRIS-II MOTOR)
- FREQUENCY (H3)

FIGURE 87

PLOT (1) WITH (2)
COMPUTED MOUNT
TRANSFER INCLUDED

PHASE ERROR DUE
TO .01 G VIBRATION
(SINUSOIDAL) APPLIED
VS
FREQUENCY OF VIBR
(MJS MOTOR)

COMPUTED ERROR
WITH OUTRIGGERS
MODELED AS ONE
DEGREE OF FREEDOM
(MJS IRIS MOTOR)

PHASE ERROR

FREQUENCY (HZ)

67

C.   Radiometer

Current specifications for the radiometer channel
are listed in Table 10. A block diagram of the proposed radiometer
implementation is shown in Figure 38. The thermopile detector
output is chopped using FET analog switches at a 480 Hz rate.
The chopped signal is transformer coupled into a preamplifier and
amplifier, full wave demodulated, then amplified in a 1 Hz band-
width DC amplifier. To provide some gain stability, DC feedback
is provided.

Three data outputs are presently planned for the
radiometer: high gain and low gain outputs to the FDS; and an
output to the IRIS housekeeping (HK) multiplexer. The HK output
is integrated for the interferogram time of 45 seconds.

If a detector-noise limited system is assumed, then
the radiometer signal-to-noise ratio when viewing a target with
radiance of 2.5×10^{-4} Wcm^{-2} Sr^{-1} may be determined from

$$S/N = \frac{\xi\, N\, A\Omega \sqrt{\tau}}{NEP}$$

where

ξ = efficiency = 0.35

N = Radiance of source $- 2.5 \times 10^{-4}$ $Wcm^{-2}Sr^{-1}$

$A\Omega$ = Aperture x FOV = 3×10^{-2} $cm^2 Sr$

τ = integration time = 1 second

NEP = Detector noise equivalent power = 5×10^{-10} $Watts/\sqrt{Hz}$

The calculated signal-to-noise ratio for the radiometer output
to FDS is

$$S/N = 5250$$

For the HK radiometer output the integrator offset
error is a potential source of error. However, it appears that
an offset error of .025 percent maximum can be achieved by use
of a matched dual FET (2N5196).

D.   FDS/IRIS Interfaces

Table 11 is a listing of FDS/IRIS Interface Signals.
These interfaces are described in the following paragraphs.

>75<

TABLE 10. RADIOMETER SPECIFICATIONS

SPECTRAL RANGE : 5000 TO 33,000 cm^{-1} (2 μ to .3 μ)

SPECTRAL RESPONSE : FLAT WITHIN $\pm$ 20% OVER THE SPECIFIED
SPECTRAL RANGE

FIELD-OF-VIEW : 1.49 X 10^{-5} Sr
(COINCIDE WITH INTERFEROMETER)

DETECTOR : THERMOPILE
SIZE - 6 to 7 MM DIAMETER
RESISTANCE - $\simeq$ 15K
RESPONSIVITY - $\simeq$ 30 VOLTS/WATT
NEP - $\simeq$ 5 X 10^{-10} WATTS/$\sqrt{Hz}$
TIME CONSTANT $\simeq$ 1 SECOND

SIGNAL-TO-NOISE : $\geq$ 100 WHEN VIEWING SOLAR SIMULATOR
WITH RADIATION OF 2.5 X 10^{-4} W cm^{-2} Sr^{-1}

DATA OUTPUTS : (A) FDS OUTPUT 1 (LOW GAIN)
(B) FDS OUTPUT 2 (HIGH GAIN, X16)
(C) HK CHANNEL OUTPUT

DYNAMIC RANGE : (A) FDS OUTPUT 1 AND FDS OUTPUT 2
COMBINATION - 4096
(B) HK OUTPUT - 4096

OPERATING TEMPERATURE : (A) DETECTOR, CHOPPER, PREAMP - 200°K
(B) REMAINDER OF ELECTRONICS - 263°K
TO 318°K

POWER ESTIMATE : .315 WATTS
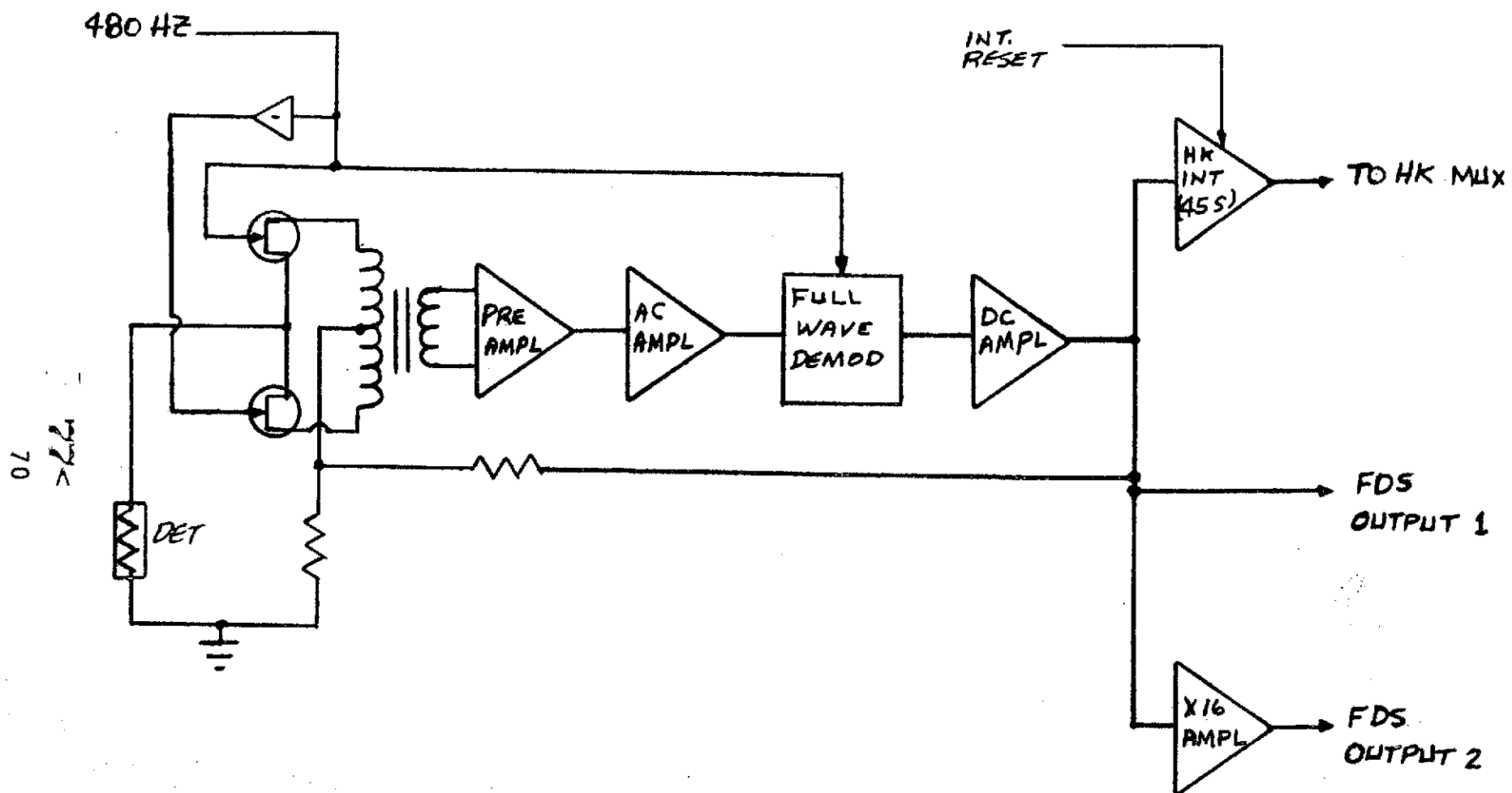
FIGURE 38. BLOCK DIAGRAM, MJS IRIS RADIOMETER CHANNEL

TABLE 11. FDS/IRIS INTERFACES

A.   DIGITAL INTERFACES
    1.   IRIS 14.4 kHz SHIFT CLOCK
    2.   IRIS PLL CARRIER
    3.   IRIS FRAME START
    4.   IRIS 480 Hz NEON REFERENCE FREQUENCY
    5.   IRIS CALIBRATE
    6.   IRIS SCIENCE DATA

B.   ANALOG INTERFACES
    1.   IRIS NEON ANALOG
    2.   IRIS RADIOMETER ANALOG LOW GAIN
    3.   IRIS RADIATING SURFACE HEATER ANALOG
    4.   IRIS PRIMARY MIRROR HEATER ANALOG
    5.   IRIS SECONDARY MIRROR HEATER ANALOG
    6.   IRIS RADIOMETER ANALOG HIGH GAIN

C.   TEMPERATURE CHANNELS
    1.   IRIS RADIATING SURFACE TEMPERATURE
    2.   IRIS PRIMARY MIRROR TEMPERATURE
    3.   IRIS SECONDARY MIRROR TEMPERATURE
    4.   IRIS ELECTRONICS TEMPERATURE

D.   CIRCUIT COMMONS
    1.   IRIS CIRCUIT COMMON 1
    2.   IRIS CIRCUIT COMMON 2

1.   Digital Interfaces

With the exception of IRIS PLL CARRIER, all digital interfaces will use the standard digital interface circuit developed by JPL. This circuit is shown in Figure 39 (a) and (b). Figure 39 (a) is the circuit for 10 volt logic supply; Figure 39 (b) is the circuit for 5 volt logic supply. The logic supply voltage for IRIS will be 10 V. All interface transmitting circuits must use 10 volt supply.

For the IRIS PLL CARRIER, the Harris HD-9-245-2 and HD-9-246-2 interface circuits using + 5 and - 5 VDC will be used.

Positive logic signal conventions apply. The output is a '1' (high = + 10 V) when the signal is present and "0" (low = 0 V) when not present.

FDS TO IRIS

a.   IRIS 14.4 kHz SHIFT CLOCK

This continuous clock shifts IRIS SCIENCE DATA and IRIS STATUS DATA into the FDS. The timing between this clock (Aϕ) and the IRIS FRAME START is shown in Figure 40. The clock pulses are 11.57 μsecond wide and will be synchronized with the 2.4 kHz power frequency so that power transitions occur between the leading edges of the 14.4 kHz A and B phases. The IRIS SCIENCE DATA is shifted on the trailing edge of the SHIFT CLOCK. The receiving subsystem will sample the serial data on the leading edge of the SHIFT CLOCK.

b.   IRIS PLL CARRIER

This signal is a continuous 403.2 kHz squarewave. Sub-multiples of this clock are used in the Michelson mirror drive phase-locked loop (PLL), Analog to Digital Converter (ADC), summation unit, and neon signal delay generator. There are no phase relationship requirements between this signal and any other FDS supplied signals. The interface circuit will be the HD-9-245-2 and HD-9-246-2 interface circuits using + 5 and - 5 VDC.

c.   IRIS FRAME START

This discrete pulse (11.57 μsec) initiates an IRIS scan and occurs every 48 seconds. It is derived from the FDS internal 14.4 kHz Bϕ clock. Its relationship with the 480 Hz neon reference and the IRIS SHIFT CLOCK is shown in Figure 40.

d.   IRIS 480 Hz NEON REFERENCE FREQUENCY

This continuous squarewave is used to derive the 120 Hz neon reference, the 80 Hz science data word rate, and various other IRIS timing signals. It is derived from the FDS internal 14.4 kHz Bϕ clock. One of its falling edges is coincident with the leading edge of the IRIS FRAME START as shown in Figure 40.

79<

a) CMOS to CMOS or CMOS to Hi-level TTL

b) CMOS to TTL

FIGURE 39. MJS77 FDS NON-ISOLATED DIGITAL INTERFACE CIRCUITS

PARTS LIST

PART TYPE	PART NUMBER	MANUFACTURER
CMOS Hex Inverter	CD4049AK	RCA
Diode Flatpack	BC 751	TIX
Resistor Flatpack	(Sim. to ST 11541)	Beckman
Capacitor	ATC-100-62	Amer. Tech. Ceramics

There are 8 diodes per flatpack and either 2 or 3 resistor networks per flatpack.

FIGURE 40.   IRIS/FDS INTERFACES

FDS TO IRIS TIMING RELATIONSHIPS
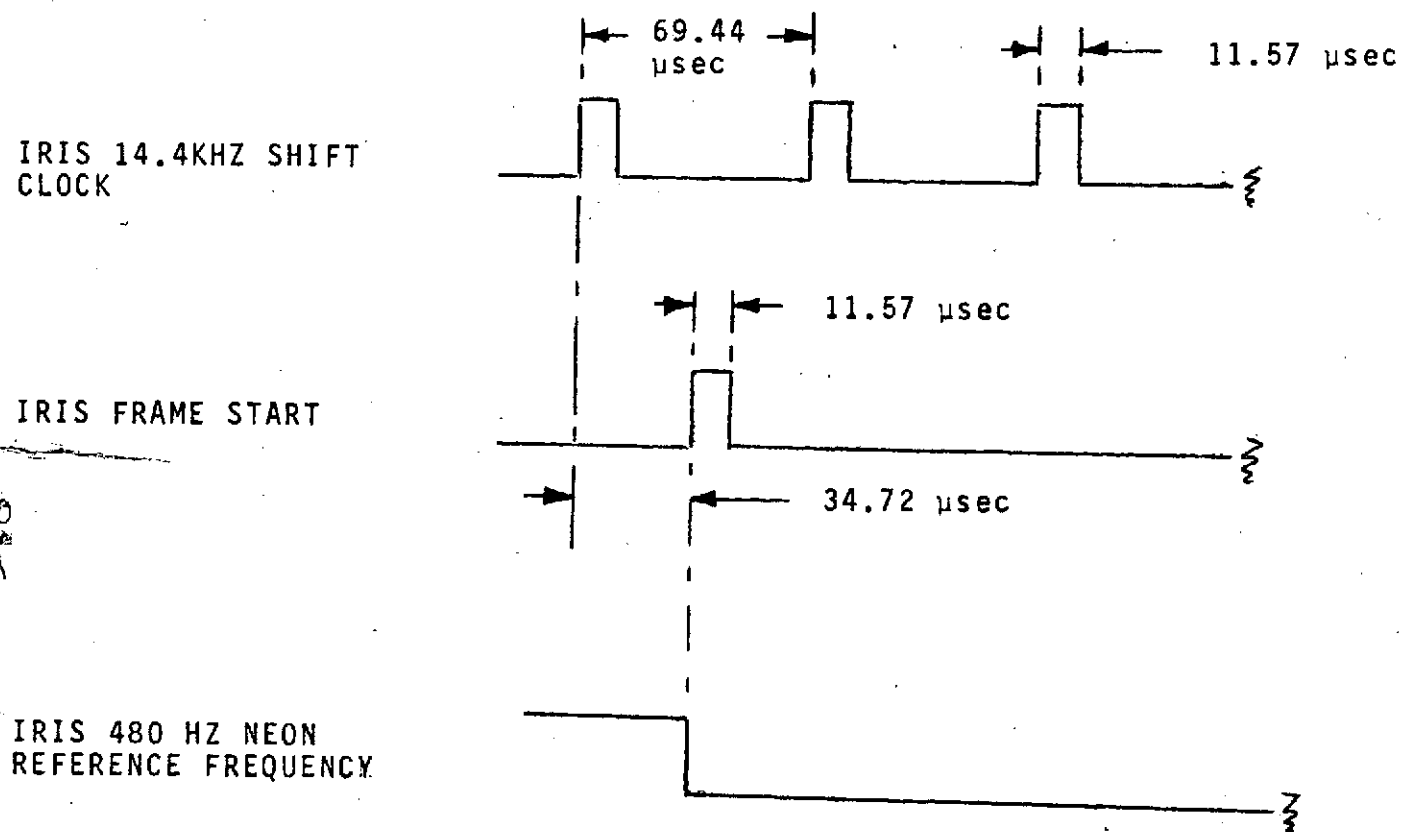
e.   IRIS CALIBRATE

This clock, coincident with SHIFT CLOCK, commands IRIS to calibrate. The FDS will gate this clock on and off in response to ground command 2.5 ms after IRIS FRAME START.

IRIS TO FDS

f.   IRIS SCIENCE DATA

This serial NRZ science word is 14 bits long. It is shifted into the FDS LSB first by the 14 SHIFT CLOCK pulses following the third falling edge of the 480 Hz neon reference frequency after IRIS FRAME START (6.25 ms) and every 6th falling edge thereafter. The timing is shown in Figure 41. The format and timing of data for a complete frame is shown in Figure 42.

2.   Analog Interfaces

All analog interfaces originate in the IRIS and are measured through the FDS engineering tree. All analog interface circuits must meet the following specifications:

Signal Level	0-3 Volts
Source Impedance	5 KΩ (Maximum)
Capacitance	1000 pf (Maximum)
Absolute Voltage Range	- 1 V to + 7 V

If the absolute range is exceeded, there will be permanent damage to the FDS engineering tree. The analog sending circuit must be able to withstand a possible FDS tree switch failure that would connect the FDS + 10 volts to the interface line through a diode and an 1 K ohm resistor or the - 3 volts through a diode and 300 ohms without affecting other subsystem functions.

The accuracy of these monitors is determined by the FDS quantization error, q, and other FDS error sources, t. For the FDS 8-bit ADC, the quantizing error is $q = .2\%$; other error tolerance is $t = .61\%$. Total error is $q + t = .81\%$.

IRIS TO FDS

a.   IRIS NEON ANALOG

This 0-3 volt signal indicates the voltage of the reference interferometer neon signal. This signal

82<

75

FIGURE 41. IRIS/FDS INTERFACES

IRIS SCIENCE DATA
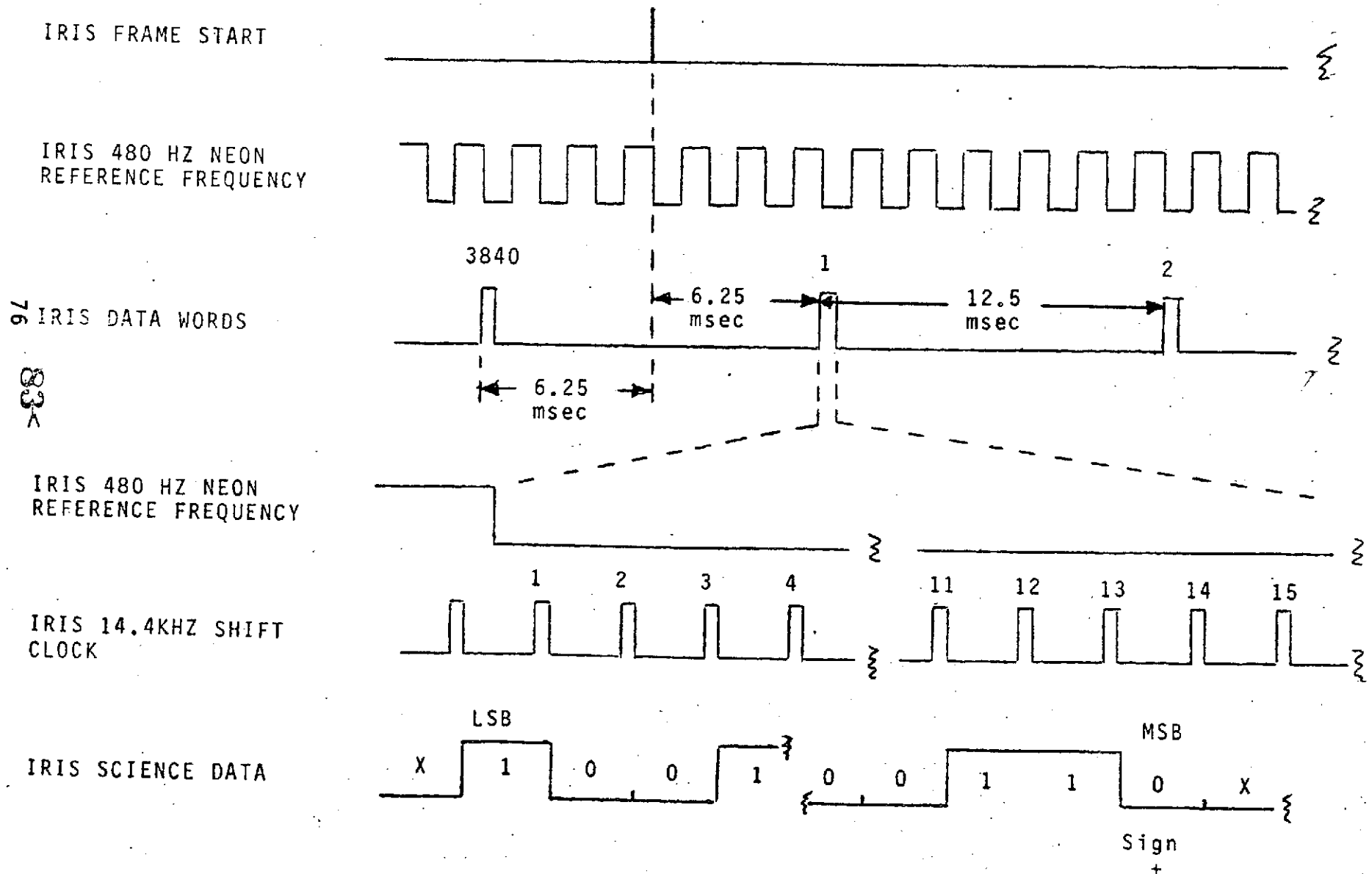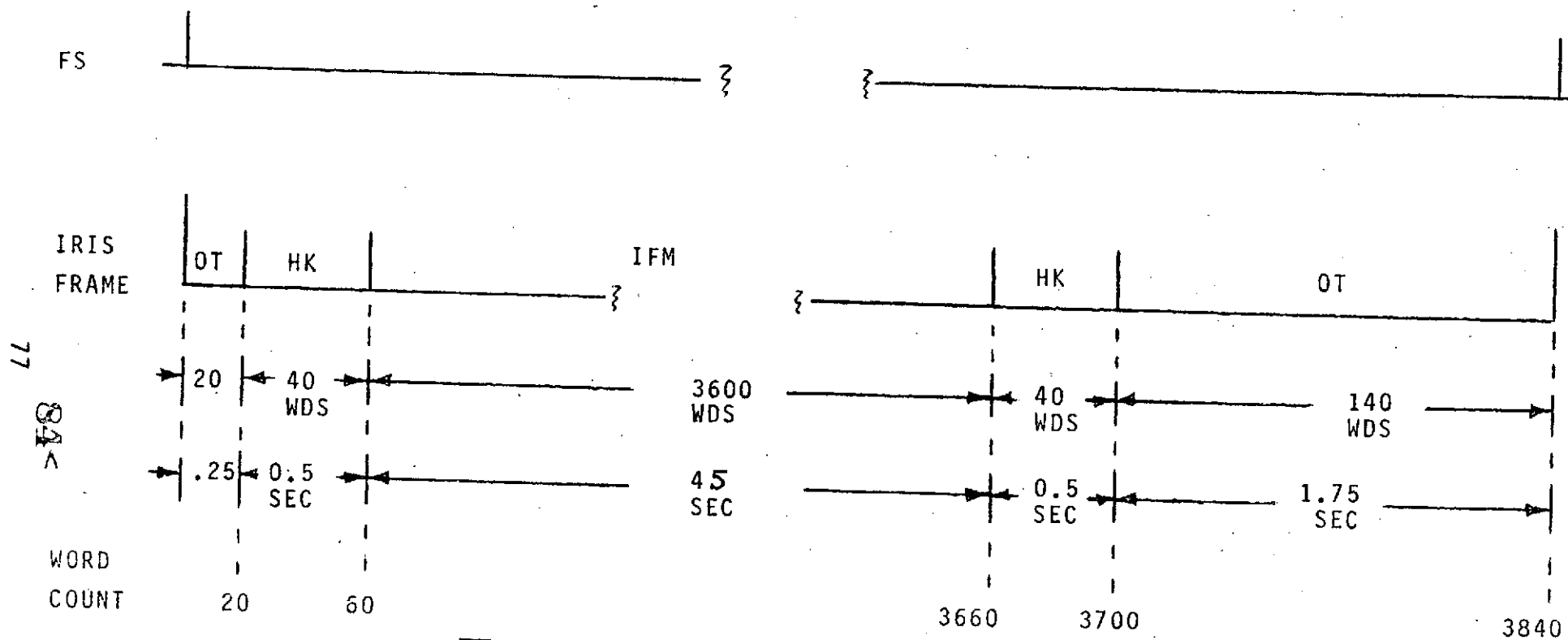
FIGURE 42. IRIS FRAME TIMING

WORD COUNT	SCIENCE DATA WORD
1-20	OFF TIME WORDS
21-60	HOUSEKEEPING
61-3660	INTERFEROGRAM DATA
3661-3700	HOUSEKEEPING
3701-3840	OFF TIME WORDS

will be sampled TBD times per frame.

      b.   IRIS RADIOMETER ANALOG

This 0-3 volt signal indicates the output voltage of the radiometer channel. This signal will be sampled one time per second.

      c.   IRIS RADIATING SURFACE HEATER ANALOG

This 0-3 volt signal indicates the power being dissipated in the radiating surface heater. The circuit configuration shown in Figure 43 will be used to provide one heater monitor output for the redundant heater circuits. This signal will be sampled at 10 to 15 minute intervals.

      d.   IRIS PRIMARY MIRROR HEATER ANALOG

This 0-3 volt signal indicates the power being dissipated in the heater for the telescope primary. See (c.) for more details.

      e.   IRIS SECONDARY MIRROR HEATER ANALOG

This 0-3 volt signal indicates the power being dissipated in the heater for the telescope secondary. See (c.) for more details.

      3.   Temperature Channels

To measure temperatures, the FDS generates a 1.0 ma constant current that is sent to temperature transducers in the IRIS subsystem. The FDS measures the resulting 500 to 600 mv voltage across the transducer resistor divider network shown on Figure 44. Transducer characteristics are given in the following equation.

TRANSDUCER CHARACTERISTICS

$$R_T/R_0 = 1 + \alpha \left\{ T - \delta \left(\frac{T}{100} - 1 \right) \left(\frac{T}{100} \right) - \beta \left(\frac{T}{100} - 1 \right) \left(\frac{T}{100} \right)^3 \right\}$$

    T = temperature in $^{\circ}C$

    R_T = transducer resistance at T

    R_0 = transducer resistance at the ice point

α, β, δ constants supplied with each transducer. (R_0 also supplied.)
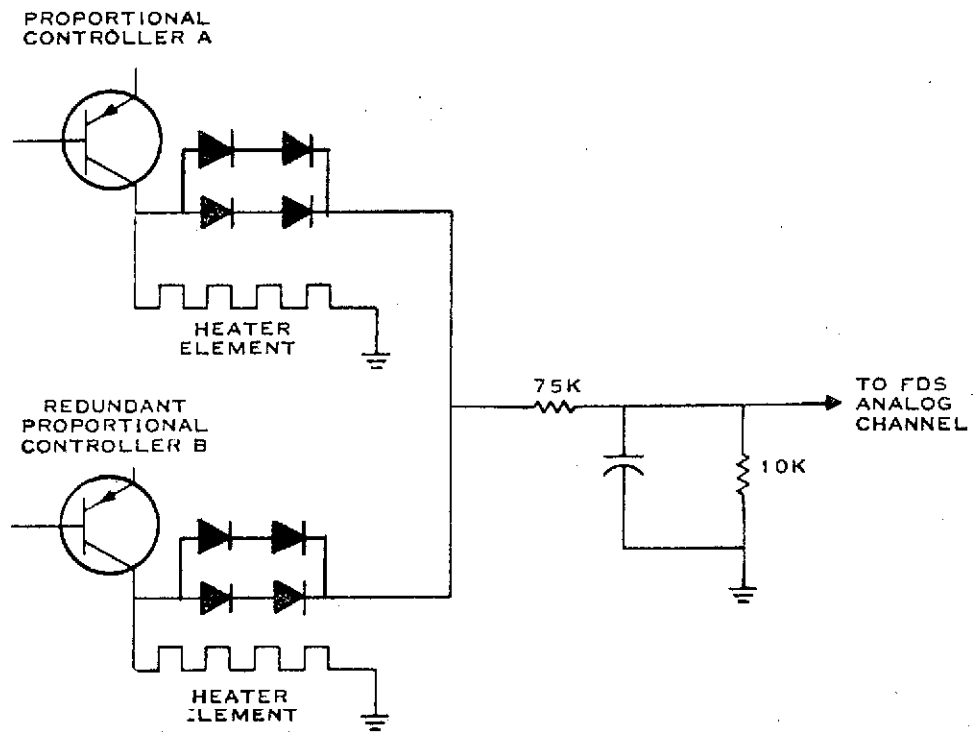
85<

FIGURE 43. HEATER MARGIN MONITOR

CONSTANT CURRENT SOURCE — 1 MA

V_{OUT}

R_{SR} (SERIES)

R_{SH} (SHUNT)

R_T (TRANSDUCER)

R_{SR} & R_{SH} ARE TYPICALLY 0.1% RESISTORS.

FDS

IRIS

Conditions:

1. For any particular measurement, ΔR (of the entire network) shall be 100 Ω.

2. At the coldest temperature, the network shall be 500 Ω.

$$\Delta R = 100\ \Omega = \frac{R_T \max \times R_{SH}}{R_T \max + R_{SH}} - \frac{R_T \min \times R_{SH}}{R_T \min + R_{SH}}$$

$$R_{SR} = 500\ \Omega - \frac{R_T \min \times R_{SH}}{R_T \min + R_{SH}}$$

FIGURE 44. TEMPERATURE MEASUREMENTS

87<

TYPICAL VALUES

R_0 = 500 Ω

α = 0.00392

β = 0.11 (neg. temp.)

   = 0.00 (positive temp.)

δ = 1.49

The measurement accuracy of the FDS is determined by the FDS quantization error, q, and other FDS error sources, t. For the FDS 8 bit ADC, the quantizing error is q = 0.2%, other error tolerance is 0.61%. Total error is q + t = 0.81%.

Two interface lines are supplied with each transducer; the signal and signal return.

a.   IRIS RADIATING SURFACE TEMPERATURE

This temperature is measured through the FDS Engineering tree as described above.

b.   IRIS PRIMARY MIRROR TEMPERATURE

This temperature is measured through the FDS Engineering tree as described above.

c.   IRIS SECONDARY MIRROR TEMPERATURE

This temperature is measured through the FDS Engineering tree as described above.

d.   IRIS ELECTRONICS TEMPERATURE

This temperature is measured through the FDS Engineering tree as described above.

E.   Detectors

To achieve system Noise Equivalent Radiance (NER) requirements for the MJS IRIS, the infrared detector used must have a Noise Equivalent Power (NEP) of 1 X 10^{-10} watts/$Hz^{1/2}$ or better over the data frequency band. Additional detector specifications are shown in Table 12. During the design study, a survey has been made of available detectors and several have been purchased for evaluation. Table 12 lists the detectors ordered and the procurement status of these devices. Table 13 gives the detector test status; Figures 45-48 show the detector test results to date.

88<

TABLE 12. DETECTORS

MAJOR SPECIFICATIONS:

SIZE	2mm ϕ
SPECTRAL RANGE	2.5 to 50 μm
NEP	$\leq 1 \times 10^{-10}$ watt/$H_z^{1/2}$
DATA FREQUENCY BAND	1.4 to 28 H_z
OPERATING TEMPERATURE	200°K

DETECTOR SELECTION PHILOSOPHY

BUY AVAILABLE, STANDARD DETECTORS FOR EVALUATION WHILE PURSUING METHODS AND TECHNIQUES FOR NEP IMPROVEMENT WITH THE DETECTOR MANUFACTURERS.

DETECTORS ORDERED

MANUFACTURER	MODEL NO.	STATUS
BARNES ENG.	L-400 SERIES	RECEIVED
LASER PRECISION	KT-2120	RECEIVED
MOLECTRON	P1-42	DUE 3/29
MOLECTRON	P1-12	RECEIVED
MATSUSHITA	-	DUE
REEDER	RDE-1 (1X1 mm)	PURCHASED DURING COMPATIBILITY STUDY

ALL OF THESE DEVICES ARE LITHIUM TANTALATE ($LiTaO_3$) PYROELECTRIC DETECTORS WITH THE EXCEPTION OF THE MATSUSHITA DEVICE WHICH IS A LEAD TITANATE ($PbTiO_3$) PYROELECTRIC DETECTOR AND THE REEDER DEVICE WHICH IS A THERMOPILE DETECTOR.

89<

TABLE 13. DETECTOR TEST STATUS

DETECTOR TEST STATUS

- TEST ARE BEING PERFORMED ON TEST SET-UP AT TI CENTRAL RESEARCH LABORATORY, DETECTOR R&D GROUP.

- TESTS PERFORMED TO DATE ARE AS FOLLOWS:

    1. REEDER THERMOPILE NEP MEASUREMENT, 300°K

    2. BARNES DEVICES (2) NEP MEASUREMENT, 300°K AND 200°K, VACUUM.

    3. LASER PRECISION DEVICE NEP MEASUREMENT, 300°K, AMBIENT PRESSURE AND VACUUM.

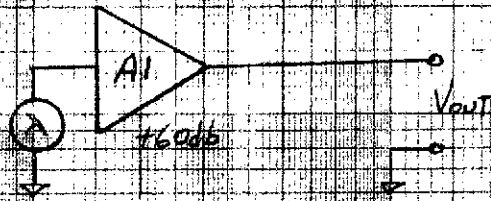   4. MOLECTRON P1-12 DEVICE NEP MEASUREMENT, 300°K, AMBIENT PRESSURE.

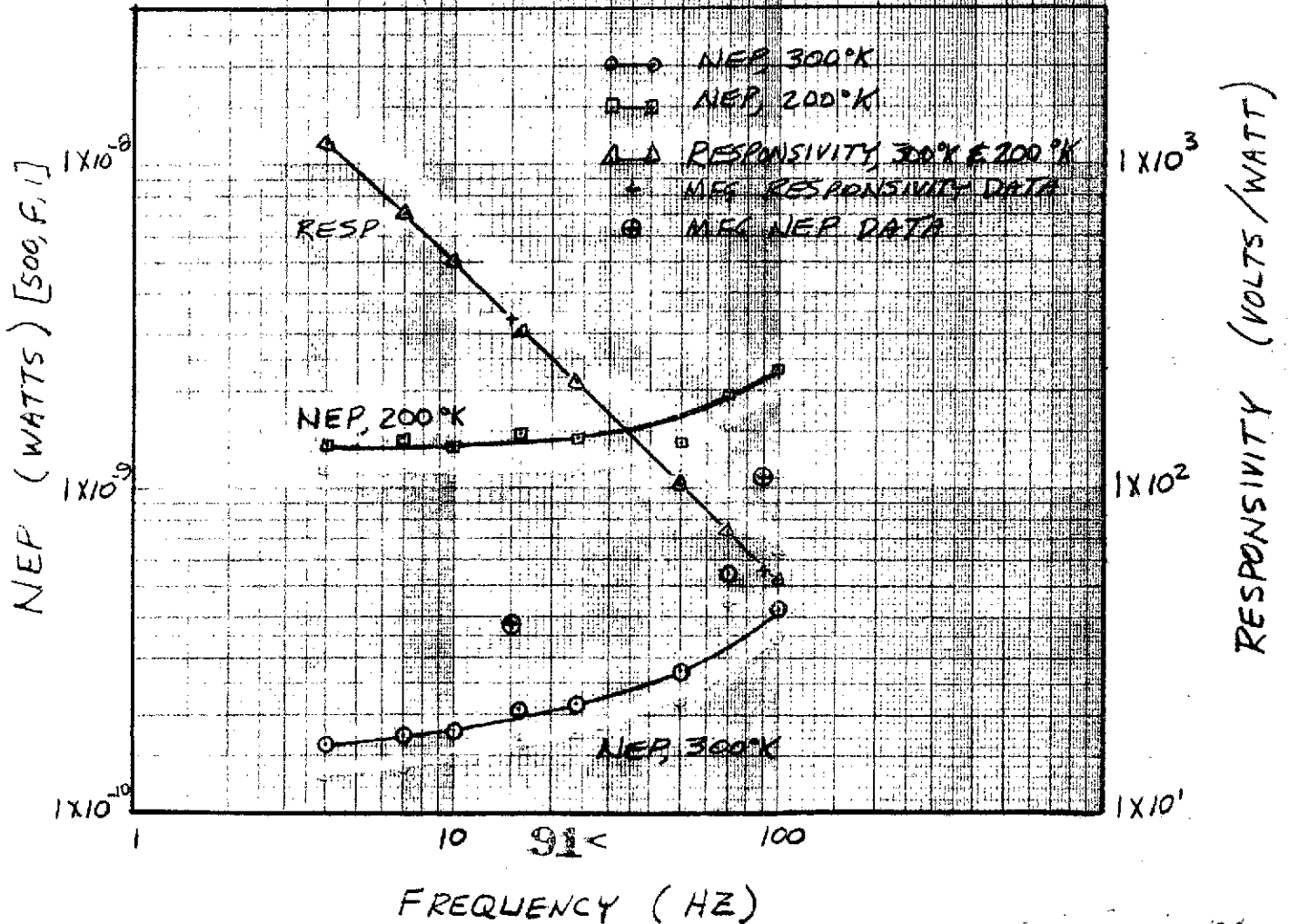TEST RESULTS

SHOWN ON FOLLOWING FIGURES

FIGURE 45.

BARNES L-400 PYROELECTRIC
S/N 11882

NOTES:

(1) A1 — HgCdTe AMP ZT #4, GAIN = 1000

(2) OUTPUT MEASURED WITH QUAN-TECH 304 TDL
1 HZ BANDWIDTH, 10 SEC METER TIME CONSTANT

FREQUENCY (HZ)

84

FIGURE 46.

BARNES L-400 PYROELECTRIC
S/N 11884

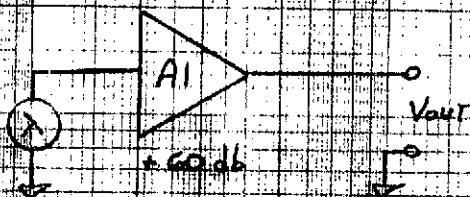NOTES:
(1) A1 = H_gC_dTe AMP 2 T H.A. GAIN = 1000
(2) OUTPUT MEASURED WITH QUANTECH 304 TDL
1 HZ BANDWIDTH, 10 SEC METER TIME CONSTANT
(3) OUTPUT MEASURED WITH QUAN-TECH 2449
5.8 HZ BANDWIDTH, 10 SEC METER TIME CONSTANT
4. FOR RUN 2 AT 200°K STABILIZE TIME WAS
INCREASED TO ~ 2.5 HRS.

NEP, 300°K
NEP, 200°K, 1ST RUN
NEP, 200°K, 2ND RUN
RESPONSIVITY, 300°K & 200°K
MFG RESPONSIVITY DATA
MFG NEP DATA

RESP

NEP
200°K

NEP, 300°K

92<

FREQUENCY (HZ)

NEP (WATTS) (500, f, 1)

RESPONSIVITY (VOLTS/WATT)

85
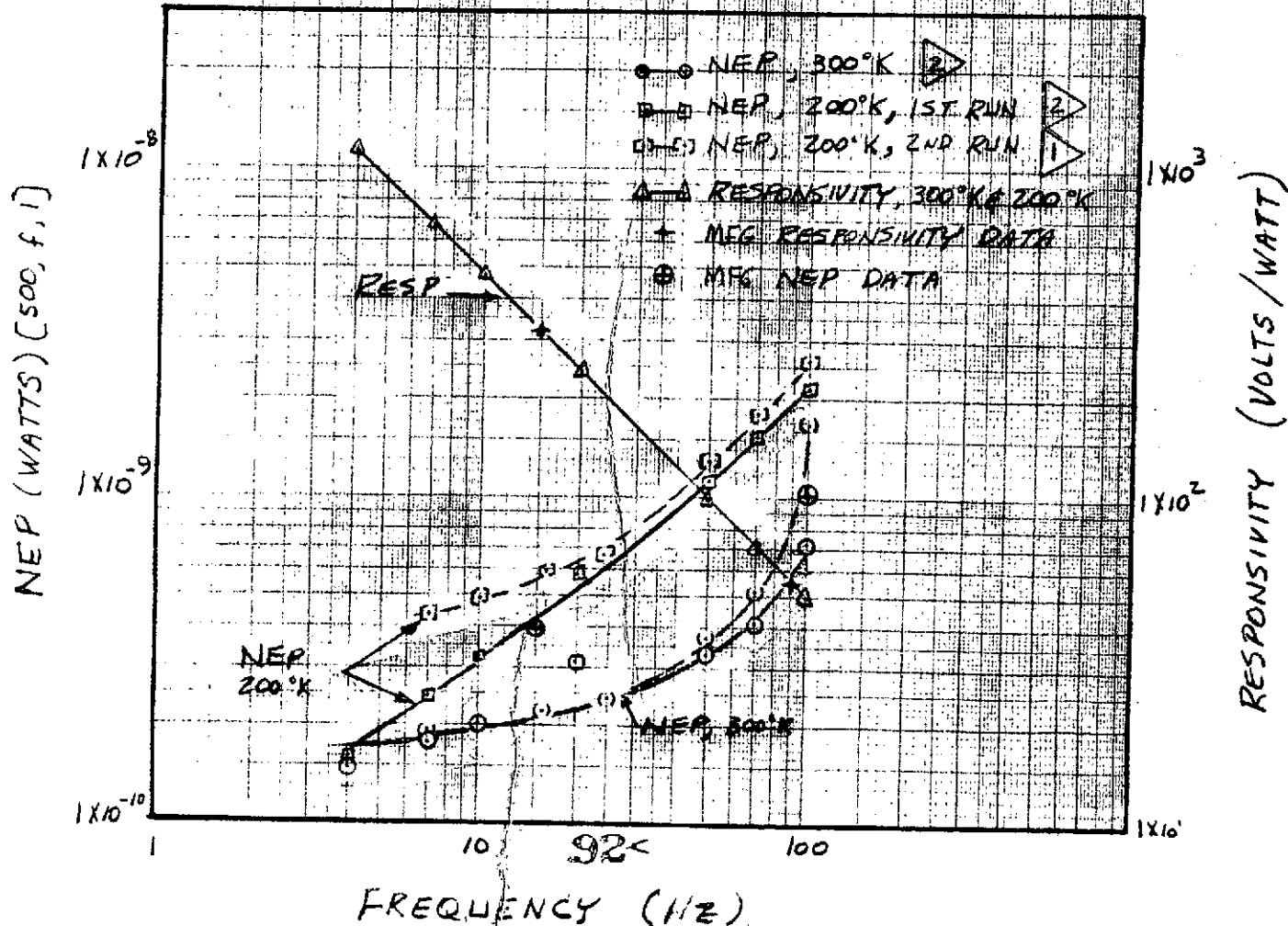
FIGURE 47.

LASER PRECISION PYROELECTRIC
KT-2120H, SN K-308-1
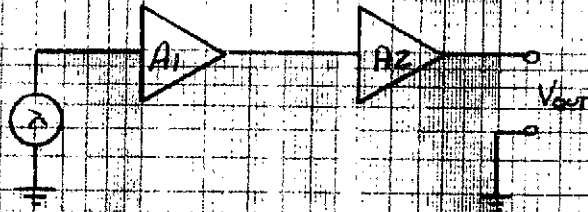
NOTES:
(1) A1 — LASER PREC. KTM 211 AMPLIFIER
(2) A2 — OP AMPLIFIER (LM108), 20db GAIN
(3) OUTPUT MEASURED WITH QUAN-TECH 304 TDL
    1 HZ BW — 10 SEC METER TIME CONSTANT
(4) RESPONSIVITY MEASUREMENT INCLUDES
    AMPLIFIER A1
(5) A1 AND A2 OUTSIDE OF DEWAR

NEP AND RESPONSIVITY
VS FREQUENCY,
300°K
o—o NEP
△—△ RESP
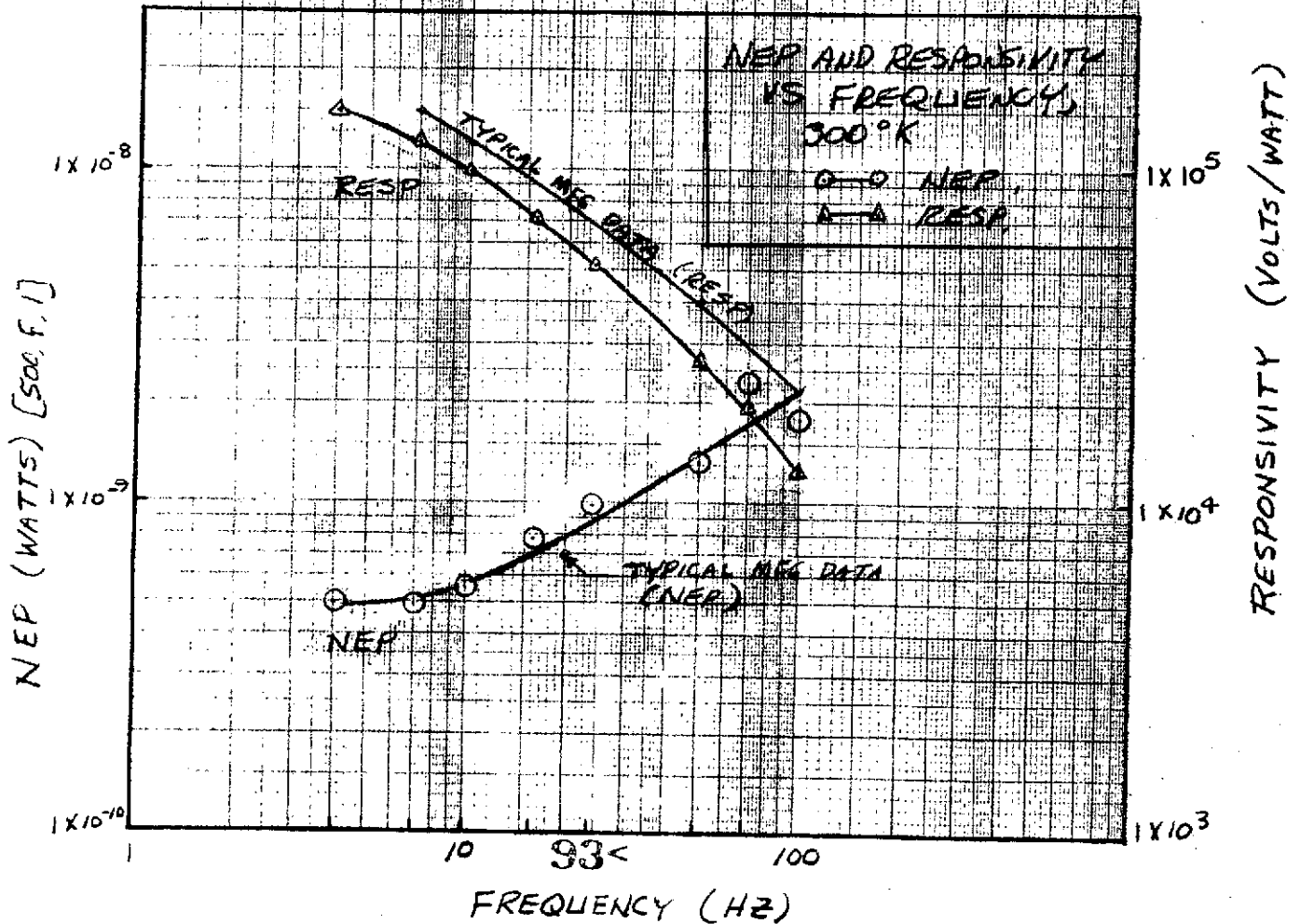
FIGURE 48.

Reeder Thermopile
RDE-1
S/N H-14764

+40db   +20db   +60db

1:100

A₁   A₂

V_OUT
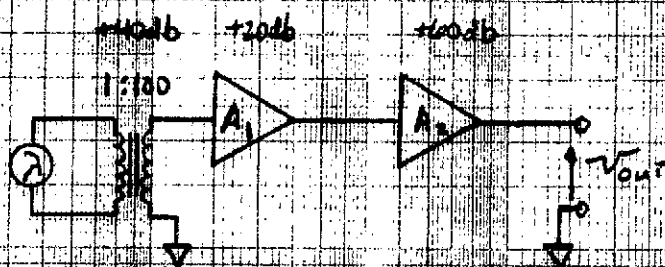
A₁ - Ithaco 167
A₂ - HgCdTe Amp 2T #4

Output Measured with Quan-Tech 304 TDL
1 Hz BW - 1 sec Meter Time Constant

NEP(500,f,1)

NEP ◯—◯
Rᵥ △—△

94<

87
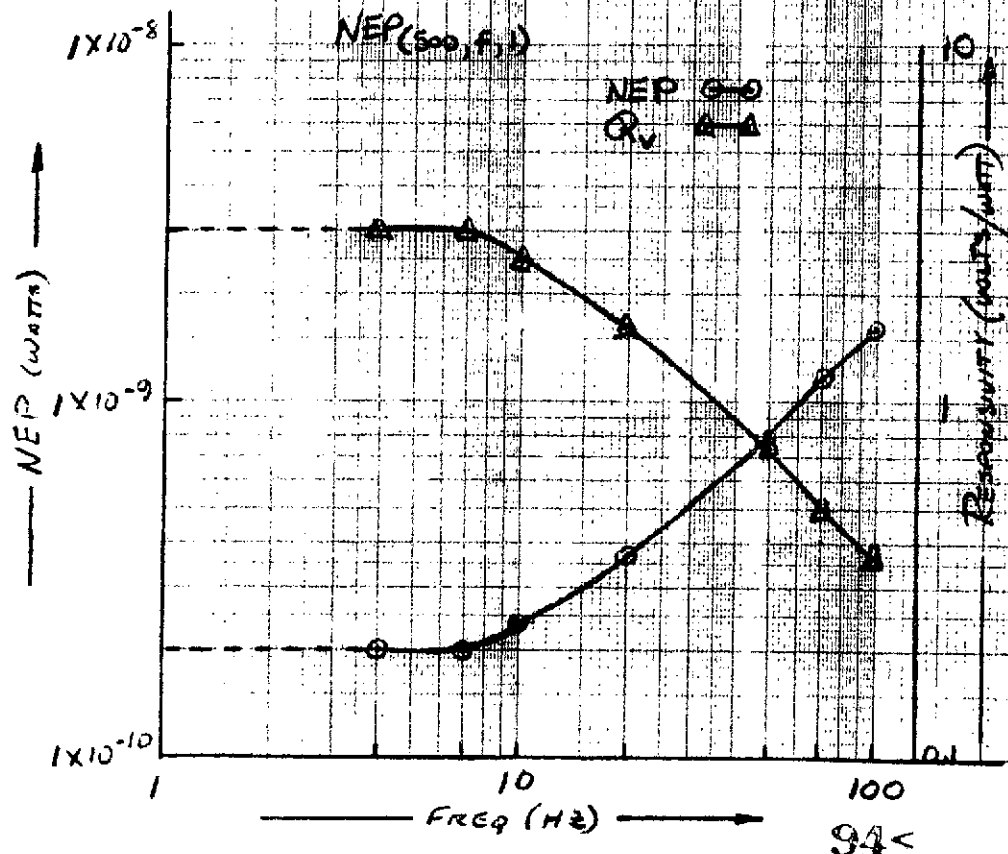
Two Barnes L-400 series devices were tested at 300°K and 200°K. Data for these devices are shown in Figure 45 and Figure 46. The 300°K NEP of both devices was measured to be approximately a factor of 2 better than indicated by the Barnes data sheet. However, the Noise of both devices increased significantly at 200°K. This increase in noise was unexpected since almost every relevant parameter of the detector and FET (which is included in the detector case) theoretically improves with decreasing temperature. However, practically no data exists for 200°K operation.

To try to isolate the cause of the increased noise at 200°K, the following action is planned:

1.   Barnes will measure the change in resistance of the detector load resistor with temperature.

2.   Repeat 200°K noise measurements with detector looking at itself to eliminate effects of possible temperature variations of detector.

3.   Barnes is wiring another FET (TI England device) in one of the detectors so that possible FET noise sources may be identified.

Figure 47 shows the test results from tests of the Laser Precision KT-2120 device. The measured NEP at 300°K was slightly worse than the value calculated from the manufacturer's data sheet. Further tests are planned on this device with a larger dewar so that the KTH211 preamplifier may be mounted at the detector rather than outside the dewar.

Figure 48 shows the results from tests of a 1 x 1 mm thermopile detector built by Reeder. Based on these test results, the Reeder thermopile detector appears to be a viable backup to the pyroelectric detector if responsivity can be boosted to approximately 10 volts/watt and the time constant can be reduced to approximately 5 milliseconds as claimed by Mr. Reeder.

Because of the low impedance and low responsivity of the thermopile, a transformer coupled preamplifier is required. The tests were performed with a transformer with a low frequency - 3 db point at 3 Hz and weight of 8 ounces. In the MJS application the response must be flat down to 1.4 Hz and the phase must be near zero degrees at 1.4 Hz. This implies a low frequency breakpoint of 0.1 Hz, which is impractical. An alternative is to use a transformer with flat response over the data band and to add phase correction as shown in Figure 49.

Since none of the commercially available detectors meet the MJS IRIS NEP requirements, the pyroelectric detector manufacturers have been contacted in regard to possible improvements to detector NEP. Techniques for improving the detector NEP are listed in Table 14. Table 15 shows the NEP equation

95<
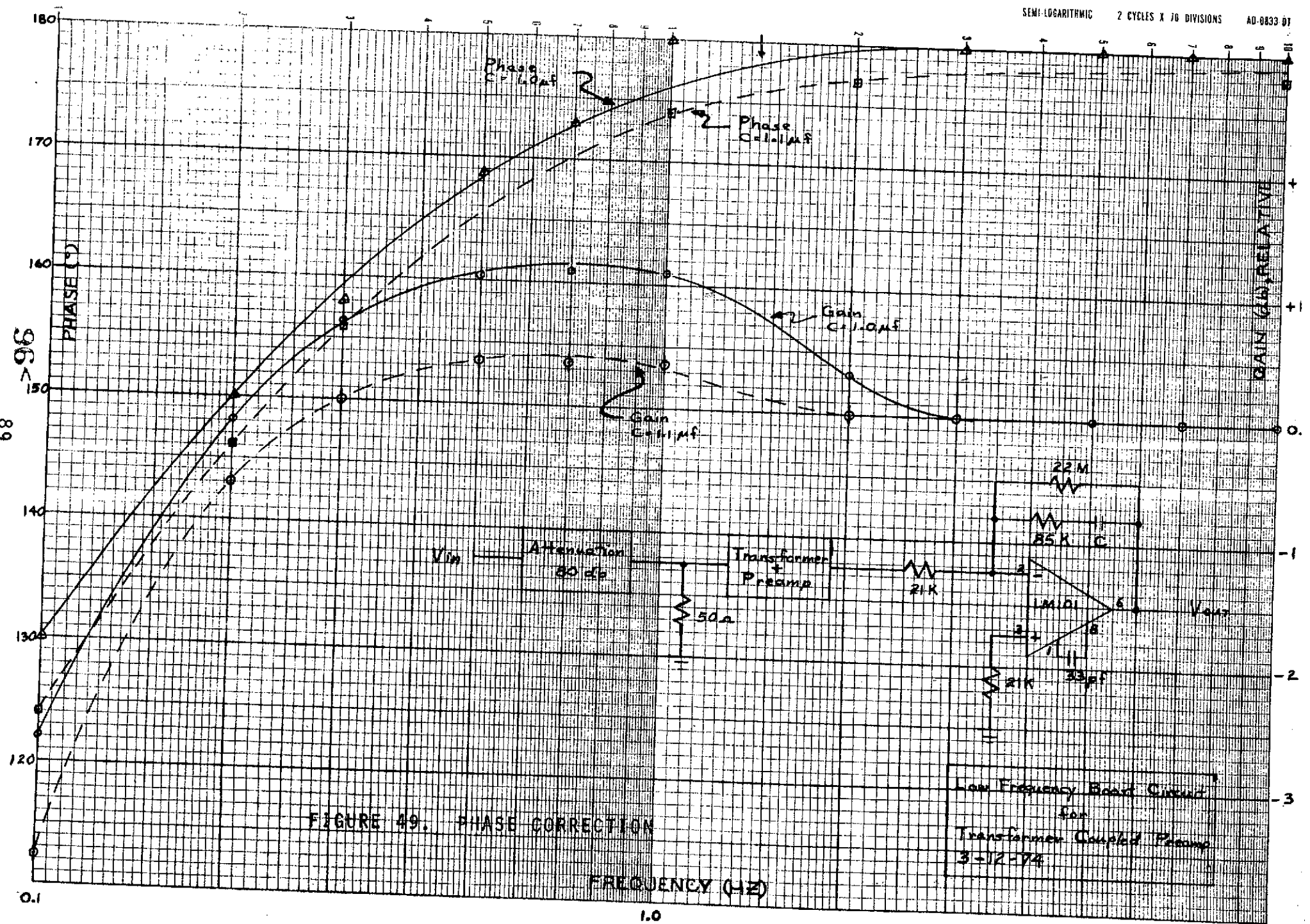
FIGURE 49. PHASE CORRECTION

TABLE 14. DETECTOR IMPROVEMENT TECHNIQUES

● SELECT MATERIAL FOR

    1.   LOWEST SPECIFIC HEAT

    2.   LARGEST PYROELECTRIC COEFFICIENT

● SELECT FET FOR

    1.   MINIMUM GATE LEAKAGE CURRENT

    2.   MINIMUM SHORT CIRCUIT NOISE

● INCORPORATE A MINIMAL THICKNESS OF PYROELECTRIC MATERIAL

● INCORPORATE LARGEST PRACTICAL FET BIAS RESISTOR

● REDUCE REQUIRED DETECTOR AREA BY USE OF A CONE COLLECTOR OR A COLLECTOR WHICH UTILIZES BOTH SIDES OF DETECTOR FLAKE.

97<

TABLE 15. NEP EQUATION

The expression for Noise Equivalent Power[*] is:

$$NEP = \left[2qI_{GSS}h^2 + \frac{4KTh^2}{R_L} + 4KT\tan\delta\, h\omega\epsilon A + V_{SC}^2\omega^2\epsilon^2 A^2 \right]^{\frac{1}{2}} \left(\frac{S}{dPs/dT}\right)$$

| Leakage Current | Bias Resistor | Loss Tangent | FET Short Circuit |

The symbols are defined:

Q = Charge on detector - coulombs

W = Radiant power on detector - watts

C = Detector capacitance - farads

ΔT = Temperature change caused by W - °K

dPs/dT = Pyroelectric coefficient - coulombs cm^{-2} °K^{-1}

h = Detector thickness - cm

A = Detector Area - cm^2

ϵ = Dielectric constant (x permittivity of free space)

Z = Thermal impedance between detector and its surroundings - °K W^{-1}

S = Thermal capacitance of detector element - Joules cm^{-3} °K^{-1}

H = Heat capacity of detector element - Joules °K^{-1}

ω = Radiation modulation frequency - radians sec^{-1}

ω_T = Thermal break frequency - radians sec^{-1}

R = Voltage responsivity - VW^{-1}

R_L = FET bias resistance - ohms

q = Electron charge - 1.602×10^{-19} coulombs

I_{GSS} = FET gate leakage current - amperes

K = Boltzmann constant

T = Ambient temperature - °K

$\tan\delta$ = Loss tangent of the detector (dissipation factor)

V_{SC} = FET short circuit noise - volts $Hz^{-\frac{1}{2}}$

[*] BARNES

(as expressed by Barnes) from which the relationship of the various parameters may be noted. Both Barnes and Molectron feel that a pyroelectric detector can be built which meets MJS NEP requirements as well as the environmental requirements by utilizing a combination of the improvement techniques listed in Table 14.

99<

APPENDIX A

IRIS DATA CHANNEL SIMULATION

SECTION I

INTRODUCTION

A. PURPOSE

The FORTRAN code *TR7401* is an analytical tool recently developed within the Signal Processing Systems Section of the Systems Analysis Branch (in the Advanced Development Department of the Radar and Digital Systems Division). It was developed for Marcus Rhodes of the Space Systems PCC to assist in analyzing (by simulation) the effects of various error and noise sources within the MJS'77* IRIS (infrared interferometer spectrometer). The simulation model of the IRIS instrumentation assumes a flat spectral input and is sufficiently general to permit the investigator to specify the error sources, their magnitudes and noise statistics to be considered during simulation.

B. THE MICHELSON MIRROR

The IRIS instrument is basically a Michelson interferometer which simultaneously generates the interference patterns of an infrared source (viewed through a telescope) and an internal reference source. The [neon] reference is approximately monochromatic and of a sufficiently higher frequency than the highest spectral component in the band of target frequencies as to satisfy the Nyquist criterion when employed to sample the target signal interferogram.

In a grossly simplified description of a Michelson interferometer, consider an infrared source which is assumed to emit a perfectly collimated beam of linearly polarized, truly monochromatic light. The interferometer is assumed to be a perfectly aligned instrument having perfect optical components. Critical elements of the interferometer include a beamsplitter,

---

* MJS'77 denotes the Mariner mission to Jupiter and Saturn scheduled for 1977.

a fixed mirror, and a mirror which is moved in a straight line at constant speed. As imaged by the beamsplitter, the moving mirror is oriented perfectly parallel to the fixed mirror.

The beam of light entering the instrument is amplitude divided by partial reflection and partial transmission upon first encountering the beamsplitter. Ideally, half the energy is subsequently reflected back toward the beamsplitter by the fixed mirror, and the other half is similarly reflected back toward the beamsplitter from the moving mirror. A second division of amplitude takes place with (ideally) half of the incident energy being reflected back toward the source; the transmitted half consists of two beams which are still collimated and have the same direction of propagation depending upon the difference in optical path length between the paths associated with the fixed mirror and the moving mirror. Addition of the emerging beams can vary from full constructive interference to complete destructive interference.

From a modulation-theory viewpoint, the difference in optical path length produces an interference pattern which can be considered to be the modulation of a light-frequency signal in the fixed-length path by a similar signal in the variable-length path. Product detection of the interference pattern in a device whose time constant is much longer than a period of the light, but much shorter than the modulation frequencies introduced by the mirror motion (i.e., the instantaneous difference in optical path length) results in a demodulation of the interference pattern. The detector output (i.e., the demodulation) is termed an "interferogram."

The utility of the Michelson mirror lies in the fact that, ideally, the interferogram is the autocorrelation of the input. In the Michelson mirror, the beam associated with the moving-mirror path differs from the beam in the fixed-length path only (ideally) by the time difference corresponding to the difference in optical path length. In a detector sensitive to the energy in the input, the nonconstant part of the detector output is proportional to the integral of the product of the signal and its delayed replica, producing (by definition) the signal autocorrelation function. In a subsequent section, the generation of reference channel and signal-channel interferograms are considered individually, in turn.

C. AN OVERVIEW OF THE IRIS INTERFEROMETRY SIMULATION

A fundamental principle embodied in the IRIS instrument is that detection of the interference pattern produced by the Michelson mirror yields an "interferogram" - the [central segment of the] autocorrelation function of the light-frequency (infrared) target viewed by the instrument. Hence the target power density spectrum can be inferred from the [Fourier transform of the] interferogram. As outlined in the block diagram representation of the IRIS in Figure 1, the interferogram is detected in a square law device, and the detector output voltage (electrical signal) is filtered, sampled, quantized and smoothed (by a digital filtering scheme). In its ultimate application, the digital representation of the interferogram is transmitted back to earth for subsequent data processing (e.g., apodization, Fourier transformation, etc.).

Within the IRIS instrumentation, the interferogram of the target is sampled at a rate dictated by the zero-crossings of a [neon] reference interferogram simultaneously generated witin the instrument optics. Deviations from constant mirror velocity distort the [target] signal and reference waveforms in the same sense, at each instant. Hence, perturbations of the ideally-constant mirror speed would be "cancelled" by the self-sampling scheme if interferogram bandwidths were sufficiently wide to pass the "distorted" waveforms completely, and if time coherence between signal and reference channels were preserved.

Within the simulation framework provided by the FORTRAN code *TR7401*, the user can investigate the deleterious effects of such departures from a perfect interferometry system as: perturbations of the mirror drive, filtering of the interferograms, lack of coherence between signal and reference channels, noise in the electronics, threshold errors, quantization, and digital smoothing. In assessing the degradation of IRIS processing due to practical limitations of the instrument, simulation results are presented as errors in the output power density spectrum (relative to the "ideal" spectrum corresponding to an error-free simulation of the IRIS) and in terms of noise equivalent radiance (NER).

In addition to statistical summaries and plots of spectral errors and NER, the interferograms or their frequency-domain representations also can be observed at the points in the simulation indicated in Figure 1 by numbers in parentheses.

103<
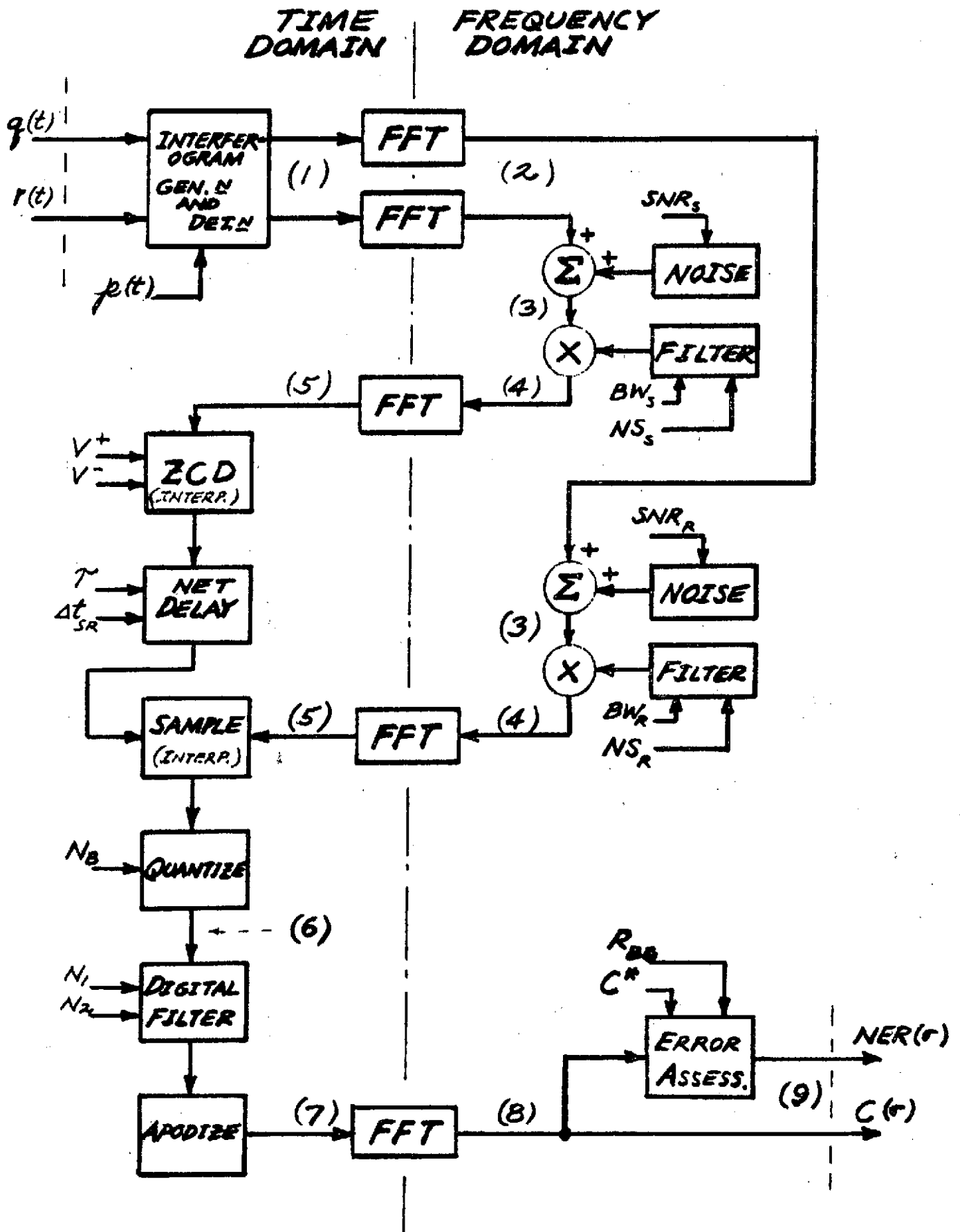
Figure 1. Block Diagram of the IRIS Interferometry Simulation

SECTION II
THE SIMULATION MODEL

A. GENERAL CONSIDERATIONS

To assess the degree of degradation in the IRIS output attributable to various error sources, the IRIS instrumentation was modelled and coded in FORTRAN IV (as the simulation program *TR7401*) for execution on the IBM System 360. Figure 1 is a block diagram of the simulation flow. The major elements of the IRIS model are shown boxed; the inputs, outputs, and user-specified parameters are indicated by labelled arrows.

A decision that had to be made at the outset concerned the choice between a purely digital simulation versus hybrid computation. The hybrid computer offers several attractive advantages: the waveforms at different points in the simulation would be readily observable (and recordable); user interaction with the computer would be facilitated; and the computer charges would be less. The decision not to use the hybrid computer was based on the following considerations: the time to develop a simulation program was relatively short; the size and complexity of the model would probably strain (or exceed) the capacity of the system (in which case the question is moot); and it would be more difficult to set up and run simulations at later dates. However, the most important considerations concern the repeatability and accuracy of the simulation. Since the desired information concerns the deviation from "ideal" output power spectrum values (on the order of one part in 10,000, nominally) that result under specified processing conditions, a digital simulation was indicated.

In the subsequent sections, the major elements of the simulation model are discussed in turn.

B. THE REFERENCE SOURCE AND ITS INTERFEROGRAM

The neon reference is assumed to be a monochromatic source, $r(t)$, of wavelength, λ_R (frequency ν_R). Characterizing the reference beams emerging from the fixed-mirror path and the moving-mirror path of the Michelson mirror by their respective electric fields, R_F and R_M, we have

$$R_F(t) = A_R\cos[2\pi\nu_R(t + x/c)]$$

and

$$R_M(t) = A_R\cos[2\pi\nu_R(t + x/c) + \Delta(t)]$$

where

F denotes the fixed-mirror path

M denotes the moving-mirror path

A_R is the amplitude of the reference wave

λ_R is the wavelength of the reference wave

ν_R is the frequency of the reference wave

c is the speed of light

t is the time variable

x is the distance variable,

$\Delta(t)$ is the phase difference between the two beams due to the difference in optical path length at the time t.

Combining the beams from the fixed-mirror and moving-mirror paths as the single reference waveform, R(t), where

$$R(t) = R_F(t) + R_M(t)$$

then since the difference in optical path length varies very slowly in comparison to detector response times, $\Delta(t)$ is assumed to be constant over time intervals on the order of the detector time constant, so that

$$R(t) = A_R\cos[2\pi\nu_R(t + x/c)] + A_R\cos[2\pi\nu_R(t + x/c) + \Delta]$$

$$= 2A_R\cos[2\pi\nu_R(t + x/c) + \Delta/2]\cos(\Delta/2)$$

Since the detector output is proportional to the energy, or power, in the input -- the time average of the square of the electric field -- the detector output (interferogram) is expressed as follows:

$$I_R(\Delta) = \frac{k}{T} \int_0^T R^2(t)dt$$

$$= k\,4A_R{}^2\cos^2(\Delta/2)\ 1/T\int_0^T \cos^2[2\pi\nu_R(t + x/c) + \Delta/2]dt$$

where

> $I_R(\Delta)$ is the reference interferogram
> k is a constant of proportionality
> T is the detector time constant

Since the detector time constant is very much longer than the period of the light-frequency reference, and

$$\frac{2}{\pi} \int_0^{\pi/2} \cos^2(x)dx = \frac{2}{\pi}\frac{\pi}{4} = \frac{1}{2}$$

then

$$I_R(\Delta) = 2kA_R{}^2\cos^2(\Delta/2)$$

$$= kA_R{}^2[1 + \cos(\Delta)]$$

The phase difference, Δ, is a function of the difference in optical path length, δ, and the wavelength of the light; that is,

$$\Delta = 2\pi\delta/\lambda_R$$

Assuming the optical path lengths are equal at $t = 0$, the difference in path length is twice the distance travelled by the mirror in time, t. Ideally,

$$\delta = 2V_m t$$

(where V_m denotes the [constant] mirror-drive speed) so that

$$\Delta(t) = 2\pi 2V_m t/\lambda_R$$

107<

2-3

Expressing the neon reference frequency in terms of its wave number, σ_R, where

$$\sigma_R = 1/\lambda_R$$

we have that

$$\Delta(t) = 2\pi(2V_m \, \sigma_R)t$$

$$= 2\pi \, f_R \, t$$

That is, the nonconstant part of the reference interferogram varies sinusoidally with frequency f_R, where

$$f_R = 2V_m \, \sigma_R$$

In the IRIS, the interferogram is AC coupled out of the detector so that, ideally,

$$I_R(t) = kA_R^2 \cos(2\pi f_R t)$$

In the simulation the amplitude of the reference interferogram (kA_R^2) is assumed to be 1.0, arbitrarily, for ease in establishing the noise power in the reference channel and the threshold levels employed in zero-crossing detection.

A time-varying departure from the ideally constant mirror speed is simulated by the inclusion of a perturbation term, $p(t)$, added to the instantaneous mirror position. That is, in general

$$\Delta(t) = 2\pi[f_R t + 2\sigma_R \, p(t)]$$

In simulating the IRIS, the perturbation can be specified as:

1. Sinusoidal (with the amplitude and frequency specified by the investigator)

2. Random (normally distributed with the mean value and standard deviation specified by the investigator)

3. The sum of 1 and 2, above.

108<

Note that if A_p denotes the amplitude of sinusoidal perturbation (or, in the case of random perturbation, the standard deviation of the distribution), and β_R denotes the corresponding phase shift of the neon reference, then in radians,

$$\beta_R = 2\pi(2\sigma_R A_p)$$

so that in the same units as wavelength, the perturbation amplitude, respect to a particular value of phase shift (in radians) of the reference interferogram is specified as

$$A_p = \beta_R \lambda_R/(4\pi) ,$$

C.   THE SIGNAL SOURCE AND ITS INTERFEROGRAM

Being an interferometer, the IRIS instrument enjoys the multiplex (Fellg ...) advantage; i.e., all the spectral components of the target are observed simultaneously (in contrast to a conventional spectrometer in which the spectral elements are explored consecutively). In the simulation model, the target spectrum is assumed to be flat over the desired band of infrared light frequencies. Simulating the IRIS subject to specified error conditions, the resulting effects can be observed across the entire band of interest, in any run.

The wave number, σ, is the number of wavelengths per unit distance (at a particular frequency), or

$$\nu = c/\lambda$$
$$= c\sigma .$$

If ν_{max} denotes the maximum wave number in IR targets of interest, then

$$\nu_{max} = c\sigma_{max}$$

and the flat power spectrum of the signal is represented as the rectangular function defined as follows:

$$Q(\nu) = \begin{cases} U, & -\nu_{max} \le \nu \le \nu_{max} \\ 0, & \text{otherwise} \end{cases}$$

If Q is real (implying a flat cophasal spectrum in which all spectral elements have amplitude U and zero phase), then the autocorrelation function, $\phi_s(t)$, being the inverse Fourier transform of the power spectrum (by the Wiener-Khinchine theorem) is

$$\phi_s(t) = 2U\nu_{max}\sin(2\pi\nu_{max}t)/(2\pi\nu_{max}t)$$

Since the convolution of a symmetric function with itself yields (identically) its autocorrelation, and the convolution of functions in the time domain corresponds to multiplication of their spectra, it follows that the time function q(t) corresponding to the rectangular spectrum Q(ν) has the same form as its autocorrelation; i.e., the time-domain representation of the target has the following form:

$$q(t) = K \sin(2\pi\nu_{max}t)/(2\pi\nu_{max}t)$$

(As will be shown, subsequently, the amplitude of the target signal is implicitly determined so that the spectral elements of the signal interferogram have unit height).

Analogous to the case of the monochromatic reference source previously discussed, the signal beams emerging from the Michelson mirror optics can be characterized by their respective electric fields S_F and S_M as follows

$$S_F(t) = A_s \sin[2\pi\nu_{max}(t + x/c)]/[2\pi\nu_{max}(t + x/c)]$$

and

$$S_M(t) = A_s \sin[2\pi\nu_{max}(t + x/c) + \gamma(t)]/[2\pi\nu_{max}(t + x/c) + \gamma(t)]$$

where $\gamma(t)$ denotes the phase difference between paths. Combining the signal beams from each path, the composite signal interference pattern is the sum

$$S(t) = S_F(t) + S_M(t)$$

$$= A_s \sin[\alpha(t)]/[\alpha(t)] + A_s \sin[\alpha(t) + \gamma(t)]/\alpha(t) + \gamma(t)]$$

110<

2-6

where we have attempted to simplify notation by the following definition:

$$\alpha(t) = 2\pi\nu_{max}(t + x/c)$$

The signal interferogram is obtained by detection; that is,

$$I_s(\gamma) = \frac{k}{T} \int_0^T S^2(t) \, dt$$

$$= kA_s^2 \frac{1}{T} \int_0^T \left\{ \frac{\sin^2[\alpha(t)]}{\alpha^2(t)} + \frac{2\sin[\alpha(t)]}{[\alpha(t)]} \cdot \frac{\sin[\alpha(t) + \gamma]}{[\alpha(t) + \gamma]} \right.$$

$$\left. + \frac{\sin^2[\alpha(t) + \gamma]}{[\alpha(t) + \gamma]^2} \right\} dt$$

But, since

$$\int_0^\infty \frac{\sin^2 x}{x^2} \, dx = \pi/2$$

and

$$\lim_{T \to \infty} \frac{1}{T} \int_0^T \frac{\sin^2 x}{x^2} \, dx = 0$$

The first and last terms in the integrand of the expression for the signal interferogram contribute essentially nothing to the average. (The integration time, T -- the detector time constant -- is on the order of a millisecond; a 2.5 µm IR signal has a period of 0.8×10^{-14} seconds).

With the vanishing of the first and last terms, the expression for the signal interferogram reduces to the proportion

$$I_s(\gamma) \propto \frac{1}{T} \int_0^T \frac{\sin[\alpha(t)]}{[\alpha(t)]} \cdot \frac{\sin[\alpha(t) + \gamma]}{[\alpha(t) + \gamma]} \, dt$$

Recalling the definition of the autocorrelation of a function, v(t),

$$\phi(\tau) \equiv \lim_{T \to \infty} \frac{1}{T} \int_0^T v(t) \, v(t + \tau) \, dt$$

it is seen that the interferogram is proportional to the autocorrelation function of the target signal, $q(t)$. Further, since functions of the form $\sin(x)/x$ are their own autocorrelation functions (as implied previously), it follows that

$$I_s(\gamma) \propto \sin(\gamma)/\gamma$$

As observed in Section II.B, the phase difference is a function of the difference in optical path length, δ, and the wave number of the signal (the largest wavenumber in the signal spectrum, in this case); that is,

$$\gamma = 2\pi\delta\sigma_{max}$$

$$= 2\pi(2V_m t)\sigma_{max}$$

$$= 2\pi f_{max} t$$

where

$$f_{max} \equiv 2V_m\sigma_{max}$$

Hence

$$I_s(\gamma) = A_s \sin(2\pi f_{max} t)/(2\pi f_{max} t)$$

In order that the spectral components of the signal interferogram have unit amplitude (for convenience, in the simulation), we let

$$A_s = 2f_{max}$$

and have, in the ideal case, that

$$I_s(\gamma) = 2f_{max} \sin(2\pi f_{max} t)/(2\pi f_{max} t)$$

In an analogous manner to the reference-channel case, perturbation of the Michelson mirror constant-speed condition is simulated by the inclusion of the perturbation term, $p(t)$, added to the instantaneous mirror position, so that

$$\gamma(t) = 2\pi[f_{max}t + 2\sigma_{max}p(t)]$$

and

$$I_s(\gamma) = 2f_{max}\sin(\gamma)/\gamma$$

As the IRIS is simulated on a digital computer, the waveforms (and spectra) are observed only at discrete points. In the time domain, resolution is determined by the specification of a simulation time-increment, Δt, and the length of the time interval is determined by N, the number of time increments. The interferograms are generated from t_{min} to t_{max}, where

$$t_{min} = -N \Delta t/2$$

and

$$t_{max} = -t_{min} - \Delta t$$

At each point in time, the perturbed mirror position is superimposed upon the nominal (constant-speed) position, the phase shifts Δ and γ are computed, and the values of the reference and signal interferograms corresponding to their respective time shifts are determined as previously outlined.

It is pointed out here that in conjunction with the specification of N, the specification of Δt deserves careful consideration, since an important tradeoff is involved. The time increment must be small enough to provide a sufficiently good [sampled] representation of the reference interferogram (say, several points per period) and yet large enough that the interval from t_{min} to t_{max} contains all but a negligible portion of the signal interferogram energy. (Choosing $\Delta t \simeq 0.001$ seconds with N = 2048 results in about eight points per period of the reference interferogram and about 28 lobes on each side of the signal interferogram. This appears to be at least marginally acceptable.)

D. FAST FOURIER TRANSFORM (FFT)

As indicated in Figure 1, the simulated IRIS processing takes place in both time and frequency domains. The link between the alternative signal representations is the Fast Fourier Transform (FFT), an efficient approximation to the Fourier transform which relates the power density spectrum and autocorrelation of a function (or the complex spectral components and a time waveform).

An efficient ALC (IBM-360 assembly language) version of the Cooley-Tukey FFT algorithm* is employed to perform the transformations. The efficiency of FFT algorithms is based on successive divisions by two of the interval from 0 to 2π; hence the length of the FFT "window" -- the number of points employed in the sampled representation of a time- or frequency-domain function -- is a power of two. Letting Nu denote the exponent and N the size of the FFT, the relationship is

$$N = 2^{Nu}$$

For a specified time increment, Δt, the total time, T, frequency-domain resolution, Δf, and frequency limits f_{min} and f_{max} are related as follows:

$$T = (N-1)\Delta t$$

$$\Delta f = 1/T$$

$$f_{min} = -N\Delta f/2$$

and

$$f_{max} = -f_{min} - \Delta f$$

The FFT is a <u>discrete</u> transform relating a sampled waveform and a finite set of spectral components; thus it is implicit that the time- (or frequency-) domain representations are but single periods of infinite, periodic waveforms (or spectra). In the employment of an IRIS instrument, the interferogram of an IR source is produced by the finite travel of the moving mirror; the spectrum of the IR target is inferred from the finite time sample of the [infinite] interferogram as if it were one period of a periodic signal.

In simulating the IRIS, the time interval over which the interferogram is generated is of length T. As previously indicated, T is determined by the

---

* The ALC FFT routine is *ADW3*, which is called from the FORTRAN routine *CLYTKY*. Both routines were coded by Tony Wilbanks of the System Analysis Branch.

specification of Δt and Nu and should be long enough to include all but the tails of the interferogram in which the amplitudes can be considered negligible in relation to the interferogram peak. Aliasing will result in transforming the truncated interferogram, but smearing of the spectrum is reduced by "matching" the interferogram at the ends of the time interval. This is accomplished (within the simulation) by respecifying Δt so that T corresponds to an odd number of quarter wavelengths of f_{max}, ensuring that the interferogram terminates in the middle of a lobe (of the $sin(x)/x$-shaped interferogram) at both ends. As long as perturbations of the Michelson mirror are relatively small in relation to a period of f_{max}, additional measures to reduce aliasing (e.g., apodization) do not appear to be warranted.

Strictly speaking, the inverse Fourier transform should be employed to obtain the time function corresponding to a specific set of [complex] spectral points. For convenience, the direct transform is employed throughout the simulation; however, spectra are maintained symmetric (with antisymmetric phase angles) and time functions are maintained real, in every case. Thus the transformations are legitimate.

E.   DETECTOR/AMPLIFIER NOISE

As indicated in Figure 1, noise in the instrument electronics is simulated by the addition of pseudo-random "noise" to the spectra of the interferograms. The signal-to-noise ratios in signal and reference channels are specified independently. If detector/amplifier noise is to be included in the simulation [as indicated by the investigator's specification of input data (see Section III.A)], then a vector having an amplitude equal to the inverse of the specified signal-to-noise ratio and a [uniformly distributed] random phase angle is added to each positive spectral component. The conjugate of each noise vector is added to the corresponding negative-frequency point.

F.   LOW-PASS FILTERS

In both channels of the IRIS instrument, the detected interferograms are filtered to a specified bandwidth. In the simulation, the filters are completely defined by the [independent] specification of the cut-off frequency and the number of filter sections in each channel. In a highly-idealized representation, each filter is assumed to be perfectly flat out to the specified cut-off frequency, at which point the response is assumed to roll

off at 6 dB/octave (20 dB/decade) for each section specified. In addition, the filter is assumed to introduce zero phase shift at all frequencies.*

The filter is implemented by multiplication (in the frequency domain) of the [complex] interferogram spectrum by the [complex] filter function in each channel. Since the filters are implemented in such a straightforward way, it would be a relatively simple matter to substitute more realistic filter descriptions, if desired, as [complex] functions of frequency (e.g., products of transfer functions, and/or nonlinear filter functions).

The interferograms are AC coupled from the detector, in the IRIS. In the simulation, the zero frequency (DC) value is set to zero in the spectrum of the reference interferogram. The DC is not removed from the signal interferogram, since removal of the zero-frequency component in the case of a truncated interferogram would correspond to the addition of a negative bias, which is undesirable since the "tails" of the interferogram should approach zero, asymptotically.

G. ZERO-CROSSING DETECTION

A particularly important aspect of the IRIS processing concerns the sampling of the signal-channel interferogram at a rate determined by the [ideally sinusoidal] reference interferogram. In this manner, any nonlinear mirror motion will affect both interferograms in the same way, and sampling at times proportional to the observed frequency of the reference will aid in cancelling errors in the mirror motion.

The sampling times are derived from the zero-crossings of the reference interferogram. Each zero-crossing is defined by determining the time at which the positive-going [real] waveform crosses the positive threshold, or the negative-going waveform crosses the negative threshold. (The threshold values are specified independently so that threshold errors, hysteresis, bias, etc., can be simulated). Each threshold-crossing time is determined by cubic interpolation, using the set of four equi-spaced points bracketting the crossing (two points on each side).

---

* The phase shifts introduced by a linear phase filter and the delay
introduced into the reference channel are absorbed (in the simulation)
in the [specified] net delay between the two channels.

H. NET TIME DELAY BETWEEN CHANNELS

The linear phase filter in the signal channel introduces a delay which must be compensated for, if coherence between channels is to be maintained. In the IRIS, a shift register in the reference channel is employed to delay the zero-crossing times and maintain coherence.

The error in time delay (from the exact value necessary to maintain coherence) is simulated by specifying a value for the net time delay to be added to the detected zero-crossing times. Since the delay is discrete, the time determined by interpolation is delayed to the next shift-register clock time and, additionally, by the integral number of shift-register clock periods closest to the specified net delay between channels.

I. INTERFEROGRAM SAMPLING

The reference-channel interferogram zero-crossing times, delayed by the specified net time delay between channels, constitute the set of times at which the signal-channel interferogram is to be sampled. The corresponding interferogram sample values are determined by cubic interpolation, using the two closest points on each side of the sampling time, in each case.

J. QUANTIZATION

In the analog-to-digital conversion (ADC) of the signal interferogram, the sample values are quantized to N_B bits (not including the sign bit). In simulating the quantization, it is assumed that the maximum interferogram amplitude ($2f_{max}$) is some fraction of full scale (N_B bits). If k_F denotes the specified fraction of full scale, the resolution of interferogram amplitude values, ΔI, is determined by the expression for a single quantization level

$$\Delta I = 2f_{max}/(k_F 2^{N_B})$$

Each interferogram sample value determined by interpolation is subsequently quantized in the simulation to the closest integral number of quantization levels.

K. DIGITAL FILTER

Following analog-to-digital conversion, the sampled and quantized signal interferogram is filtered (digitally) to smooth the data and reduce the output data rate. The data filtering and compression technique to be employed in the IRIS utilizes two summation processes: In the first, a rolling sum of N_1 data samples is performed. The interferogram samples are shifted serially through an N_1-stage shift register; at each shift, the contents of all stages are read out and combined in parallel. The second summation process is a straight sum of N_2 outputs from the first [rolling] summation; the second [straight] sum is clocked out every N_2 shifts, reducing the output data rate by the factor N_2:1. For the MJS'77 IRIS, $N_1 = 4$ and $N_2 = 3$.

Describing the digital filtering algorithm in terms of the z-transform, let $g(k)$ denote the kth interferogram sample. Then (in the time domain), the output of the first summation process, $a(k)$, is

$$a(k) = \sum_{i=1}^{N_1} g(k+1-i)$$

and the z-transform of the output is

$$A(Z) = G(Z) \sum_{i=1}^{N_1} Z^{1-i}$$

where Z^{-1} denotes a time delay of one sampling period.

For the second summation, the output $B(Z)$ is expressed

$$B(Z) = A(Z) \sum_{j=1}^{N_2} Z^{1-j}$$

so that the filtering algorithm is expressed as the product

$$B(Z) = G(Z) \left(\sum_{i=1}^{N_1} Z^{1-i} \right) \left(\sum_{j=1}^{N_2} Z^{1-j} \right)$$

In the simulation, it is assumed that $N_1 = 4$ and $N_2 = 3$ (despite the fact that N_1 and N_2 are input-data parameters - the extension to a more general digital filter is straightforward). With the IRIS parameters,

$$B(Z) = G(Z)[1 + 2Z^{-1} + 3Z^{-2} + 3Z^{-3} + 2Z^{-4} + Z^{-5}]$$

and, by inspection, the time domain response of the filter is obtained as

$$b(k) = g(k) + 2g(k-1) + 3g(k-2) + 3g(k-3) + 2g(k-4) + g(k-5)$$

However, the output is only observed every N_2 sample-times. Hence the output data stream is

$$b(3k) = g(3k) + 2g(3k-1) + 3g(3k-2) + 3g(3k-3)$$

$$+ 2g(3k-4) + g(3k-5)$$

$$k = 2, 3, \ldots$$

L. APODIZATION

The number of digitally-filtered interferogram points is approximately equal to the number of reference interferogram zero-crossings in the time interval spanned by the simulation $[T = (N-1)\Delta t]$, divided by N_2(i.e., 3). In general, the number of filtered points is not an exact power of two. Before the output interferogram is transformed (by FFT) to the frequency domain a final time, the filter output is padded with a sufficient number of leading and trailing zeroes to bring the total number of points to an exact power of two.

In the simulated IRIS, as in the instrument, the output of the digital filter has its origin in a finite segment of a [theoretically] infinite interferogram. Hence the truncated interferogram exhibits discontinuities at the points where the zero-level "tails" are "attached." In order to suppress the high-frequency components associated with the discontinuities, the original segment of the augmented filter output is apodized before transformation.

Ideally, apodization should provide a smooth transition of the filter output to zero, removing the discontinuities; the central section of the interferogram (containing most of the information) should be affected as little as possible. An apodization function having these characteristics is suggested by Connes* (in her dissertation) as the following function

$$M(t) = [1 - (t/L)^2]^2 , \quad -L \leq t \leq L$$

This apodization is applied in the simulation. The peak value of the filter output (t = 0) is determined by fitting a quadratic function in the [three point] neighborhood of the maximum sample value. The apodization interval (2L) is defined as two times the shorter of the intervals between the time of the peak and each of the interferogram limits (assuming equally-spaced samples).

M. ERROR ASSESSMENT

The goal in simulating the IRIS is to determine the degradation in performance associated with non-ideal characteristics of the instrument. In IRIS applications, various data processing techniques are applied to the output interferogram samples to obtain the best possible inference of the input [IR target] spectrum.

In the IRIS simulation, the interferogram samples are apodized and transformed (by FFT) to the frequency domain. In order to have a basis of comparison, the "ideal" power spectrum is defined as the transform of the apodized, sampled output interferogram obtained by an "error-free" simulation of the IRIS -- no perturbation of the Michelson mirror, no detector/amplifier noise, sufficient bandwidth to pass essentially all of the signal- and reference-channel interferograms, no error in zero-crossing detection thresholds and no net time delay between channels.

Simulating the IRIS subject to a specified set of error conditions, the difference between the obtained power spectrum and the "ideal" spectrum yields, directly, a measure of spectral error at each discrete frequency associated with a component of the flat, input [IR] spectrum. The "ideal" output power spectrum, theoretically, would have unit values (in the band of data frequencies);

---

* J. Connes, Rev. Opt. 40 (1961); An English translation is available as a Navy publication NAVWEPS report no. 8099, NOTSTP 3157, published by the U. S. Naval Ordnance Test Station, China Lake, California.

the simulated "ideal" differs from the unit rectangle, slightly, due to the applied apodization, the finite extent of the interferogram, the simulation of a delay shift register, the quantization and computer noise. Nevertheless, the spectral difference is considered to be the "percent error" at each frequency, the difference having been [implicitly] normalized to unity.

Conventionally, the spectral error is expressed in terms of noise equivalent radiance (NER). The NER at some frequency would be determined by calculating the ratio of the difference in power spectrum values at that frequency and a second [reference] frequency to the corresponding difference in responsivities (to a blackbody target at T°K). Since the simulated IRIS responsivity is flat, NER is computed simply by multiplying spectral error and blackbody radiance. That is, at wave number σ, NER(σ) is computed according to the relationship

$$NER(\sigma) = \frac{|C(\sigma) - C^*(\sigma)| \cdot R_{BB}(\sigma)}{C^*(\sigma)}$$

where

$C(\sigma)$ is the calculated value of the power spectrum at σ

$C^*(\sigma)$ is the "ideal" value of the power spectrum at σ

R_{BB} is the blackbody radiance (in watts cm^{-2} steradian^{-1} cm)

and R_{BB} is approximated by the relationship

$$R_{BB}(\sigma) = C_1\sigma^3/[\exp(C_2\sigma/T - 1)$$

where

σ is the wave number (in cm^{-1})

$C_1 = 1.1909 \times 10^{-12}$ watt cm^2 steradian^{-1}

$C_2 = 1.4380$ cm°K

T is temperature (in °K).

121<

In order to assess the degradation in output power spectrum due to errors, the simulation provides digital plots of the output spectrum (superimposed upon the "ideal" spectrum), spectral error, NER and (for reference purposes) the blackbody radiance curve. Also, statistics (mean value, variance, standard deviation and the maximum value) are computed for spectral error and for NER, across the specified band of data frequencies.

APPENDIX B

MJS IRIS ELECTRON RADIATION
TEST RESULTS SUMMARY

123<

MJS-IRIS ELECTRON RADIATION TEST RESULTS SUMMARY

Several components considered critical to the IRIS instrument operation were selected for irradiation simulating the Jovian electron radiation environment. Electron bombardment was conducted under the control of JPL personnel. Test specimen parameter measurements were performed by Texas Instruments.

The short time span available for test preparation precluded dynamic testing of component parameters during irradiation and also limited the total number of test specimens to those immediately available. However, the specimens tested respresent a majority of those components expected to be unique to the IRIS instrument.

Two separate radiation tests were performed. The first group of tests involved energy levels up to 3 Mev. The second set of tests was conducted at 20 Mev. No shielding was provided for either test in order to allow a worst case evaluation.

As far as permanent damage is concerned, only one component, the neon filter lens, suffered sufficient degradation to have possibly resulted in an instrument failure, and most of this degradation was sustained at the lower energy levels where shielding is most effective. Only slight degradations were observed after full dosage in the transmission of the visible portion of the beamsplitters and the output intensity of the gallium-arsenide source. Finally, while the clear glass envelopes of the neon bulbs were darkened, no permanent effects were detected within the spectral interval of interest.

The following briefly describes the baseline parameters monitored for each component and summarizes the individual test results.

124<

A.   CsI BEAMSPLITTERS

1.   Visible Transmission

Visible transmission was checked through one spot on each piece of CsI, through an aperture of $\sim$ 0.25 x 0.375 inch. Approximately the same spot was used when testing the samples before irradiation and after subsequent irradiations. The spectral band was limited by a band pass filter centered at 5800Å, with a half width of 100Å. A tungsten filament quartz-iodine lamp was the radiation source, and a United Detector Technology UDT PIN-10 was the detector used (silicon Schottky diode). The following transmission properties were observed:

SAMPLE	SAMPLE CONDITION	% TRANSMISSION
A	BEFORE RADIATION TESTS	39
A	AFTER 3MEV TEST	36
A	AFTER 20MEV TEST	34
B	BEFORE RADIATION TESTS	71
B	AFTER 3MEV TEST	68
B	AFTER 20MEV TEST	65

Sample A was a coated substrate, viewed through the same aperture used for the interferometer reference channel. Sample B was an uncoated but mounted piece of CsI. The aluminum mounting ring showed a noticeable darkening on one surface after the high energy irradiation, similar to a black anodized finish. Some slight coloration appeared in the CsI after irradiation, but the only quantitative measurements were listed in the previous table.

The transmission was down $\sim$ 5% after each handling and irradiation, the losses being somewhat greater for the coated than the uncoated sample. Some of the loss can probably be attributed to the collection of H_2O on the sample surfaces and subsequent clouding by atmospheric water vapor.

125<

If experimental error is added to the uncertainty, it would appear that while some loss of transmission did occur due to irradiation it was certainly less than $\sim$ 5%.

2.   IR Transmission

The IR transmission of the samples was checked on a Perkin-Elmer Model 457 over the wavelength range 2.5-40.0 μm. The only changes that were identifiable in the spectra as the testing progressed were the possible addition of H_2O absorption. This can be attributed to collection of atmospheric H_2O accumulated during handling and testing. The humidity was in excess of 70% in Dallas while some of the testing was done at Texas Instruments.

3.   Summary

The visible and IR transmission tests carried out on two CsI substrates (one coated, one uncoated and mounted) indicate that no static effects occurred in the IR region observed. Some deterioration was seen in the visible tests carried out at 5800Å, but these involved reductions in transmission less than 5% after each irradiation.

B.   NEON BULBS

The output intensity and starting voltage of K-3A neon bulbs were monitored before and after radiation tests. Relative measurements of the output intensity were made using a silicon reference detector. Intensity measurements were obtained for both the broad spectral output and a limited band using a band pass filter centered at 5800Å, with a half width of 100Å. The bulbs were sustained with a constant current of 1.8 ma, simulating the actual application. The following results were obtained.

1.   Bulb #1

126<

        (a)   Pre-Radiation Measurements
             Relative Output Intensity   0.221
             Starting Voltage   112 Volts

        (b)   Post 3Mev Radiation Measurements
             Relative Output Intensity   0.2205
             Starting Voltage   112 Volts

2.   Bulb #2

        (a)   Pre-Radiation Tests
             Relative Output Intensity   0.655
             Starting Voltage   112 Volts

        (b)   Post 20 Mev Radiation Tests
             Relative Output Intensity   0.681
             Starting Voltage   113 Volts

3.   Summary

      Both clean glass bulbs were observed to be a light shade of brown following irradiation, with the bulb exposed to 3 Mev being slightly darker. However, no changes in the output intensity or starting voltage beyond the measurement uncertainties of 1-2%, could be detected or ascribed to static radiation effects.

C.   NEON FILTER LENS

   1.   Lens #1

      The relative transmission of a 6929$\overset{o}{A}$ bandpass filter lens was measured using a K3A neon bulb reference source and a silicon reference detector. Following electron irradiation at 3 Mev, the lens appeared much darker in color. The relative transmission was found to be 33% less than its initial value. The spectral response of the test specimen was subsequently measured and compared to that of a second 6929$\overset{o}{A}$ filter lens with the following results:

RELATIVE TRANSMISSION

$\lambda(\overset{o}{A})$	SECOND FILTER	IRRADIATED FILTER
6880	-0-	-0-
6890	0.02	-0-
6900	0.05	-0-
6910	0.20	-0-
6920	0.45	0.04
6930	0.56	0.12
6940	0.58	0.22
6950	0.56	0.22
6960	0.55	0.14
6970	0.44	0.01
6980	0.15	-0-
6990	0.04	-0-
7000	0.01	-0-

2. Lens #2

The second lens was later exposed to 20 Mev radiation. It also appeared darker after irradiation, but less than the first lens. The relative transmission of the second lens was measured to be 14% less than its initial value.

3. Summary

The transmission of both filter lenses was significantly degraded by electron radiation, with the 3 Mev environment being the more severe. The center frequency of the filters remained constant and the transmission losses were fairly uniformly distributed across the bandpass.

D. GALLIUM ARSENIDE LED

A PN gallium arsenide source, type TIXL10, such as used in the PLL position loop, was subjected to both radiation environments. The parameters monitored were the forward

voltage drop and the relative output intensity. The forward
voltage drop was measured with the PN junction forward biased
with 140 ma d.c. The relative output intensity was measured
with the same forward current using a silicon reference de-
tector. The following results were obtained:

1. Pre-Radiation Test Values
   Forward Voltage   +1.192 Volts
   Relative Output Intensity   0.1275

2. Post - 3 Mev Test Values
   Forward Voltage   +1.25 Volts
   Relative Output Intensity   0.1199

3. Post - 20 Mev Test Values
   Forward Voltage   +1.18 Volts
   Relative Output Intensity   0.1166

The variation observed in the forward voltage drop was
well within the uncertainty of the measurement. Small de-
gradations in output intensity of approximately 6% and 3%
were observed after 3 Mev and 20 Mev irradiations respectively.

E. SILICON DETECTOR

Relative output sensitivity measurements were obtained
for a ENL-626B silicon detector. This detector would be
used in the IRIS neon channel. A GaAs LED was used as a
reference source for all measurements. The values measured
for the relative output sensitivity were:

RELATIVE OUTPUT SENSITIVITY
1. Pre-Radiation Value   0.2698
2. Post - 3 Mev Radiation Value   0.2660
3. Post - 20 Mev Radiation Value   0.2710

No ill effects of static radiation were observed in the
output sensitivity of the ENL-626B silicon detector.

MJS-IRIS RADIATION TEST SUMMARY

TEST SPECIMEN	TEST PARAMETER	BASELINE VALUE	POST-3MEV VALUE	POST-20MEV VALUE	COMMENTS
CsI Beamsplitters A. Coated B. Uncoated	 Visible Transmission Visible Transmission	 39% 71%	 36% 68%	 34% 65%	1. IR Transmission of both specimens remained unchanged except for H_2O 2. Scintillation observed during test.
K3A Neon Bulb #1 #2	 Output Intensity Starting Voltage Output Intensity Starting Voltage	 0.221 112V 0.655 112V	 0.2205 112V 	 0.681 113V	Both bulbs turned brown- no degradation detected
Neon Filter Lens #1 #2	 Transmission Transmission	 0.0775 0.0741	 0.0521 (-33%)	 0.0634 (-14%)	1. Both lenses darkened. 2. Significant degradation.
GaAs LED	Forward Voltage Output Intensity	1.192V 0.1275	1.25V 0.1199 (-6%)	1.18V 0.1166 (-9%)	Slight degradation
Silicon Detector	Output Sensitivity	0.2698	0.2660	0.2710	No effects detected.